Dry Sliding and Rolling Tribotests of Carbon Black Filled EPDM Elastomers and Their FE Simulations

Dem Fachbereich Maschinenbau und Verfahrenstechnik
der Technischen Universität Kaiserslautern
zur Erlangung des akademischen Grades

Doktor-Ingenieur (Dr.-Ing.)
vorgelegte
Dissertation

von
Herr
MSc. Dávid Felhős
aus Vásárosnamény, Ungarn

2008

Acknowledgements

The present work was completed at the Institut für Verbundwerkstoffe GmbH (IVW) at the Technical University of Kaiserslautern.

First and foremost I would like to express my special gratitude to my supervisor Prof. Dr.-Ing habil. Dr.h.c. József Karger Kocsis for his fundamental scientific and parental support. Our exciting discussions on polymer science and technology let me broaden my knowledge and fulfill this research work.

I am especially thankful to Prof. Dr. Károly Váradi who inspirited me to start PhD studies. Thanks to his stimulating teaching I became familiar with the FE method during my stay as PhD student in Budapest before going to the IVW.

I am thankful to Prof. Dr.-Ing. Bernd Sauer for accepting the presidency of the examination committee.

I would like to thank the EU for the financial support in frames of the KRISTAL-project (Contract no.: NMP3-CT-2005-515837; www.kristal-project.org), as well as the IVW GmbH for providing me all the appropriate means to realize this PhD work. The support of the colleagues at the IVW is grateful acknowledged during my stay. Thanks for the help to B. Fodor, H. Plocharzik, S. Schmidt, H. Giertzsch, R. Schimmele, J. Stephan, M. Hentzel, Dr. M. Schehl, and especially to N. Marinova.

Thanks to T. Goda, L. Martínez, E. Román and J.L. de Segovia for their help in the publications related to chapters 8 and 9.

Last but not least, I would like to convey my special thanks to my mother and father, my sister Enikő and my brother Koppány.

1 Content

Abstract

Unlubricated sliding systems being economic and environmentally benign are already realized in bearings, where dry metal-plastic sliding pairs successfully replace lubricated metal-metal ones. Nowadays, a considerable part of the tribological research concentrates to realize unlubricated elastomer-metal sliding systems, and to extend the application field of lubrication-free slider elements. In this Thesis, characteristics of the dry sliding and friction are investigated for elastomer-metal sliding pairs.

In this study ethylene-propylene-diene rubbers (EPDM) with and without carbon black (CB) filler were used. The filler content of the EPDMs was varied: EPDMs with 0-, 30-, 45- and 60 part per hundred rubber (phr) CB amount were investigated. Quasistatic tension and compression tests and dynamic mechanical thermal analysis (DMTA) were carried out to analyze the static a viscoelastic behavior of the EPDMs. The tribological properties of the EPDMs were investigated using dry roller (metal) – on – plate (rubber) type tests (ROP). During the ROP tests the normal load was varied. The coefficient of friction (COF) and the temperature were registered online during the tests, the loss volumes were determined after certain test durations.

The worn surfaces of the rubbers and of the steel counterparts were analyzed using scanning electron microscope (SEM) to determine the wear mechanisms. Because possible chemical changes may take place during dry sliding due to the elevated contact temperature the chemical composition of the surfaces was also analyzed before and after the tribotests. For the latter investigations X-ray photoelectron spectroscopy (XPS), sessil drop tests and Raman spectroscopy were used.

In addition, the dry sliding tribotests were simulated using finite element (FE) codes for the better understanding of the related wear mechanisms. Finally, as the internal damping effect of the elastomers plays a great role in the sliding wear process, their viscoelasticity has been taken into account. The effect of viscoelasticity was shown on example of rolling friction. To study the rolling COF for the EPDM with 30 phr CB (EPDM 30) an FE model was created which considered the viscoelastic behavior of the rubber during rolling.

The results showed that the incorporated CB enhanced the mechanical and tribological properties (both COF and wear rate have been reduced) of the EPDMs. Further on, the CB content of the EPDM influences fundamentally the observed wear

mechanisms. The wear characteristics changed also with the applied normal load. In case of the EPDM 30 a rubber tribofilm was found on the steel counterpart when tests were performed at high normal loads. Analysis of the chemical composition of the surfaces before and after the wear tests does not result in notable changes. It was demonstrated, that the FE method is powerful tool to model both, the dry sliding and rolling performances of elastomers.

Kurzfassung

Trockenlaufende Gleit- Reibpaare sind wirtschaftlich und umweltfreundlich. Aus diesem Grunde werden in zunehmendem Maße geschmierte Stahl/Stahl (Metal/Metal) Reibsysteme durch ungeschmierte Stahl/Polymer Kombinationen im ersetzt. Diese Entwicklung gilt auch für Gleit- Reibsysteme, die aus Metall- und Elastomerteilen bestehen. Diese Doktorarbeit beschäftigt sich mit der Trockenreibung und dem Verschleißverhalten von Stahl/Elastomer Kombinationen

Schwefelvulkanisierte Ethylen-Propylen-Dien Verschnitte mit und ohne Russfüllung wurden bezüglich derer Reib- und Verschleißeigenschaften untersucht. Der Russgehalt der EPDM-Elastomere wurde variiert. Es wurden EPDM Werkstoffe mit 0, 30, 45 und 60 Gewichtsprozent Ruß hergestellt.

Die mechanischen und viskoelastischen Eigenschaften der EPDM Gummiwerkstoffe wurden bei quasistatischer Zug und Druckbelastung, sowie durch dynamisch-mechanische Thermoanalyse (DMTA) ermittelt. Die tribologischen Eigenschaften der EPDM Mischungen wurden in einer Testvorrichtung des Typs rotierender Zylinder (Stahl) auf Platte (Elastomer) (ROP) bestimmt. In den Versuchsreihen wurde die Normalkraft variiert. Der Reibungskoeffizient und die Temperatur der Kontaktoberfläche wurden während der Versuche kontinuierlich registriert. Der Volumenabtrag wurde in verschiedenen Zeitintervallen ermittelt. Die Verschleißoberflächen der EPDM Proben und der Stahlzylinder wurden im Rasterelektronenmikroskop (REM) inspiziert um charakteristische Verschleißmechanismen abzuleiten. Weiterhin erfolgte mittels Röntgenphotoelektronspektroskopie, Raman-Spektroskopie und Kontaktwinkelmessungen eine Analyse der Reiboberfläche, um (aufgrund der hohen Temperaturen) mögliche chemische Änderungen zu beurteilen.

Des Weiteren wurde der Verschleißvorgang mit der Methode der finiten Elementen (FE) modellhaft untersucht. Der Einfluss der Viskoelastizität wurde am Beispiel der Rollreibung von EPDM mit 30 Gewichtsprozent Ruß studiert. Durch ein erstelltes FE-Modell konnte der Verlauf des Reibungskoeffizienten während reversierender Rollbewegung im Einklang mit den Testergebnissen interpretiert werden.

Die Ergebnisse haben gezeigt, dass die mechanischen und tribologischen Eigenschaften der EPDM Gummiwerkstoffe mit zunehmendem Russgehalt deutlich

verbessert wurden. Der Russgehalt hat die vorliegenden Verschleißmechanismen maßgeblich beeinflusst. Die Variation der Normalkraft führte ebenfalls zu veränderten Verschleißmechanismen. Beim ROP-Test des EPDM mit 30 Gewichtsprozent Ruß konnte die Entstehung eines Gummi-Tribofilms an der Stahlzylinderoberfläche nachgewiesen werden. Die angewendeten analytischen Methoden konnten keinen eindeutigen Beweis für eine chemische Veränderung der EPDM Verschleißoberflächen erbringen.

Die erstellten FE-Modelle erwiesen sich als sehr nützliche „Werkzeuge“ für ein besseres Verständnis des Gleitverschleißes und der Rollreibung von Elastomeren.

List of Abbreviations- and Symbols

Abbreviations

Ar^+	ionised Argon
ASTM	American Society for Testing and Materials
C	carbon
CA	contact angle
CB	carbon black
CBS	N-cyclohexyl-2-benzothiazole sulfonamide
COF	coefficient of friction
DBP	di(n-dibutyl)
DBPA	di(n-dibutyl) absorption
DMTA	dynamic mechanical thermal analysis
DIN	Deutsches Institut für Normung
EPDM	ethylene-propylene-diene rubber
EPDM 0	unfilled ethylene-propylene-diene rubber
EPDM 30	ethylene-propylene-diene rubber with 30 phr CB content
EPDM 45	ethylene-propylene-diene rubber with 45 phr CB content
EPDM 60	ethylene-propylene-diene rubber with 60 phr CB content
ESCA	electron spectroscopy for chemical analysis
EV	effective vulcanizing
FE	Finite Elements
KE	kinetic energy
MBT	2-mercapto benzothiazole
N	nitrogen
O	oxygen
phr	per hundred rubber
POP	pin-on-plate
ROP	roller-on-plate
S	sulphur
SEM	scanning electron microscope
Si	silicon
tc1	first time curve

tc2	second time curve
TEM	tunneling electron microscope
UHV	ultra high vacuum
WLF	William – Landel – Ferry
WLP	white light profilometry
XPS	X-ray photoelectron spectroscopy
ZBEC	zinc dibenzyl dithiocarbamate
ZnO	Zinc oxide

Symbols

a_T	[-]	shift factor (WLF equation)
A	[mm]	amplitude
A_{def}	[m^2]	cross-sectional area in deformed state
A_0	[m^2]	original cross-sectional area
A_E^U	[$J \cdot kmol^{-1}$]	constant over upper limit (WLF-Arrhenius equation)
A_E^L	[$J \cdot kmol^{-1}$]	constant under lover limit (WLF-Arrhenius equation)
b	[1/m]	shape parameter of the polymer chain
b_w	[mm]	length of the wear track
$\underline{\underline{B}}$	[-]	left Cauchy-Green tensor
c	[J/K^1]	constant, characterizing the volume in which the end of the molecule bewares
C_1	[MPa]	first constant of the Mooney model ≡ C_{10}
C_2	[MPa]	second constant of the Mooney model ≡ C_{01}
C_{10}	[MPa]	first constant of the Mooney-Rivlin model ≡ C_1
C_{01}	[MPa]	second constant of the Mooney-Rivlin model ≡ C_2
d	[mm]	diameter
d_{w1}	[mm]	minor axes of the ellipse
d_{w2}	[mm]	major axes of the ellipse
D_w	[mm]	depth of the wear track
D_w^d	[nm]	mean value of aggregate diameter distribution
e_i	[-]	i-th spring-dashpot constant
E	[MPa]	tensile modulus

E_∞	[MPa]	plateau modulus of the elastomer over T_g
E_0	[MPa]	glassy modulus of the elastomer
E_i	[MPa]	modulus of rigidity for the i-th spring in the Maxwell model
E'	[MPa]	storage modulus
E''	[MPa]	loss modulus
E^*	[MPa]	complex modulus
f	[Hz]	frequency
F	[N]	force
$\underline{\underline{F}}$	[-]	deformation gradient
F_I	[MPa]	first invariant of the stress tensor
F_{II}	[MPa^2]	second invariant of the stress tensor
F_{III}	[MPa^3]	third invariant of the stress tensor
F_N	[N]	normal force
F_T	[N]	tangential force
g	[mm]	width of the guiding groove
G	[MPa]	shear modulus
h	[mm]	vertical distance
I_1	[-]	first scalar invariant of the left Cauchy-Green tensor
I_2	[-]	second scalar invariant of the left Cauchy-Green tensor
I_3	[-]	third scalar invariant of the left Cauchy-Green tensor
J_C	[1/MPa]	creep plasticity compliance
k	[J/K^1]	Boltzmann-constant ($1.3806503 \cdot 10^{-23}$)
K	[N/m]	spring constant
K'	[N/m]	storage spring constant
K''	[N/m]	loss spring constant
K_1	[-]	first WLF constant
K_2	[°C]	second WLF constant
l	[-]	bond length in the polymer chain
L	[m]	length in strained state
L_0	[m]	original length
ΔL	[m]	cumulative length
M	[-]	constant (lg(e)=0,434294)

M_c	[g/mol^1]	degree of crosslinking
n	[-]	number of bonds in the polymer chain
N	[1/m^3]	number of polymer chains per unit volume
p(t)	[N/m]	pressure load
P_{loss}	[J]	frictional loss power
r	[mm]	radius
r_s	[m]	end to end distance of polymer chains (strained state)
r_0	[m]	end to end distance of polymer chains (unstrained state)
$\bar{r}_0^2$	[m^2]	mean-square chain end distance (unstrained state)
$\left(\bar{r}_0^2\right)^{\frac{1}{2}}$	[m]	root-mean-square chain end distance (unstrained state)
R	[J·mol^{-1}·K^{-1}]	universal gas constant
$\underline{\underline{R}}$	[-]	rotation tensor
R_a	[µm]	arithmetic roughness
s	[J/K^1]	entropy of a polymer chain in strained state
s_0	[J/K^1]	entropy of a polymer chain in unstrained state
s(t)	[mm]	position of the steel ball
s_D(t)	[mm]	position of the driving part
Δs	[J/K^1]	entropy change of a polymer chain
ΔS	[J/K^1]	total entropy change
t	[s]	time
tan δ	[-]	loss factor
Δt	[s]	change in time
T	[°C]	temperature
T_C^U	[°C]	upper validity limit of WLF-Arrhenius equation
T_C^L	[°C]	lover validity limit of WLF-Arrhenius equation
T_g	[°C]	glass transition temperature
T_p	[s]	period
T_{ref}	[°C]	reference temperature
u(t)	[rad/s]	rotation speed
$\underline{\underline{U}}$	[-]	stretch tensor
v	[m/s]	velocity

$v(t)$	[m/s]	velocity of the steel ball
$v_D(t)$	[m/s]	velocity of the driving part
V_{loss}	[$mm^3 \cdot N^{-1} \cdot m^{-1}$]	loss volume
W_w	[mm]	width of the wear track
W	[MPa]	strain-energy

Greek Symbols

α	[°]	angle
γ	[-]	angular torsion
δ	[°]	phase angle
Δ	[mm]	distance
η	[m^2/s]	kinetic viscosity
γ	[°]	angle
κ	[m]	distance
λ	[-]	strain ratio
μ	[-]	coefficient of friction
ν	[-]	Poisson's ratio
ν_c	[$1/m^3$]	crosslink density
ω	[rad/s]	frequency, angular velocity
ω_0	[rad/s]	initial frequency
ρ	[g/cm^3]	density
σ	[MPa]	stress
σ_0	[MPa]	initial stress
σ'	[MPa]	elastic stress
σ''	[MPa]	viscous stress
σ^*	[MPa]	complex stress
σ_1	[MPa]	first principal stress
σ_2	[MPa]	second principal stress
σ_3	[MPa]	third principal stress
τ	[MPa]	shear stress
τ_i	[s]	time constant (i-th spring-dashpot pair for Maxwell model)

θ	[°]	angle
ε	[-]	strain
ε_0	[-]	initial strain
ε_{equiv}	[-]	equivalent or von Mises strain
ε_1	[-]	first principal strain
ε_2	[-]	second principal strain
ε_3	[-]	third principal strain

2 Introduction

The practical importance of rubbers as constructional materials does not need detailed elaboration. The most spectacular properties of rubbers are their high strain-to-break (several hundred percent), exceptional resilience and low modulus. Based on them the dimensional tolerance of rubber is relatively uncritical which is in favour of the mass production of different seals [1]. The high dry sliding friction of rubbers is a clear disadvantage for seals but one of the major benefits for tyre tread compounds. As detailed, general accepted scientific understanding of the friction and wear has not been achieved, the material development occurred mostly an empirical basis. Fuelled by tyre applications, a large body of work was devoted to assess the abrasion behaviour of rubbers (e.g. [2, 3, 4, 5, 6, 7] and references therein). These studies resulted in suitable predictions for the abrasion, however, only for certain arrangements and conditions. The “by-product” of the related research was a special terminology which is not easy to understand and follow (e.g. distinction between “mild” and “severe” wear, grouping according to various wear mechanisms). The wear of polymers, including rubbers, is differently classified (e.g. [8, 9]) whereby emphasising various aspects. This already hints for the complexity of rubber tribology. The friction and wear of rubbers differ from most of the other materials as apart of cohesive and wear components considerable energy dissipation may occur by hysteresis. Hysteretic heating is characteristic for all viscoelastic materials (such as rubbers). This comes from the viscoelastic deformation (“damping”) of the rubber over the surface topography (asperities) of the “hard” counterpart. Fundamental works on the friction and wear of rubbers have been performed until end of the 1980´s (e.g. [2, 5, 7, 10]). The interest renewal for this topic is likely due to the following aspects: a) appearance of novel modifiers and formulation methods for rubbers, b) industrial need to model (i.e. “to predict”) the behaviour of the rubber parts under the foreseen loading collectives, and c) novel possibilities for the surface texturing of the rubber and the counterparts (e.g. laser patterning).

Nowadays, there is a clear shift in the R&D activities with rubbers from abrasion toward sliding wear. Sliding friction and wear are key issues for technical rubber goods such as seals, bearings and crankshafts. They are often low-cost products but the consequence of their failure can be very high see for example the break systems of automobiles and mass vehicles or the hydro-pneumatic sealing

systems of aircraft landing gears. However, these sealing systems are usually lubricated, during long rest of the system or under extremely high pressures the lubricant can be removed from the seal-shaft or seal-housing contact area. This phenomenon occurs dry sliding conditions within the first few cycles and wear and damage of the seals are starting.

There is also an increasing demand from industrial side to achieve cost reductions. Elastomers are used in numerous applications as sliding parts whereby exploiting their excellent sealing, vibration damping and noise isolating properties. To avoid undesirable wear and to decrease friction forces in these applications usually some kind of oily or greasy lubrication is used. Beside the negative environmental impact of lubrication, the regularly needed service to refill the lost lubricant means an economical handicap. Therefore the avoiding of lubricants, keeping the products at the same quality will imply significant cost reduction and less environmental risk.

Accordingly, recent targets of the material development are improved reliability, prolonged lifetime, and maintenance-free service. Needless to say that this demand can only be met when the material development is accompanied by further measures, such as proper construction, design, and suitable manufacturing processes. To be able to fulfil the industrial expectations the processes during dry sliding need to be studied in detail. It is not clear yet what is the effect of temperature (changing during the tribotest) and how the actual testing parameters affect the material behavior in respect to sliding and wear properties. It is also unknown whether chemical changes take place in the elastomers due to the probably high flash temperatures in the contact area.

3 Background

3.1 Elastomeric materials

Elastomers are built up from long hydrocarbon polymer chains, which are connected with each other by chemical bonds. However, due to the steady developments within the class of elastomers is more proper to say that a material can be classified as elastomer which can suffer several hundred percent of strain without significant irreversible (plastic) deformation (cf. Figure 1). This “framing” allow us to consider as elastomers also those thermoplastic or hybrid polymeric materials which fulfill the upper requirement.

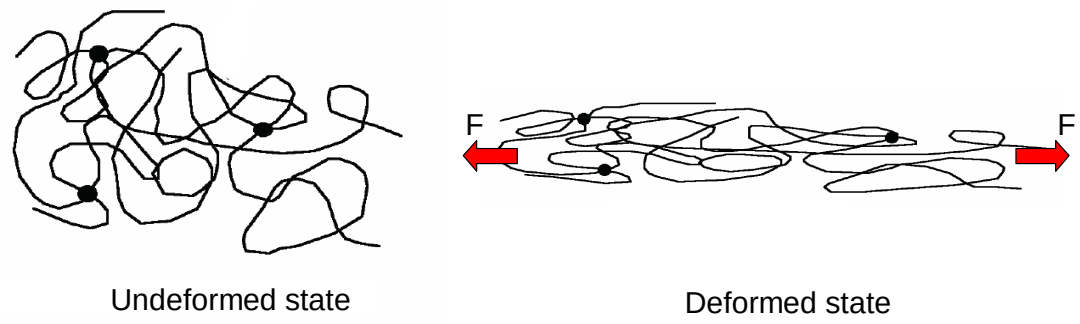

Figure 1: Reversible extension of crosslinked polymer chains

Among others the huge deformability and unusual thermal behaviors of the elastomers amaze the scientists and explorers since more than hundred years. However, the large scale technical usage of rubber becomes possible only after the discovery of the vulcanization technique (credited to Goodyear, 1839) [11]. The uncured rubber was also used for example as eraser (since the name “rubber” from Priestly) or insulator material in different medical applications. The first trials with rubber products were short timed because of the fast degradation of the uncured material that became fast sticky and smelly [12].

3.1.1 The EPDM rubber

The ethylene-propylene-diene rubber (EPDM) was chosen for investigation, because of its advantageous chemical and mechanical properties. The EPDM rubber is a synthetic elastomer whereby the M- character means that the backbone of the polymer chain is built up only from C-atoms (ISO 1692 or ASTM 1418). The EPDMs are terpolymers of ethylene, propylene and a small amount of a nonconjugated

diene, which provides unsaturation in side chains, pendent from the fully saturated backbone (cf. Figure 2) [13].

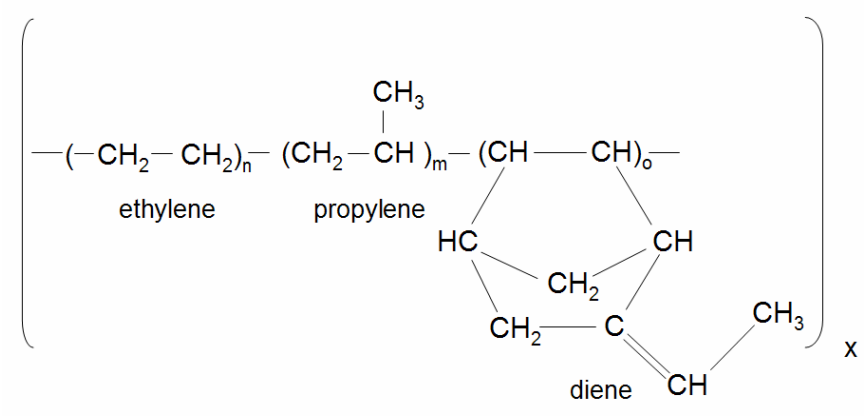

Figure 2: The molecular structure of the EPDM. Diene in that case is ethylidene norbornene

The EPDMs are produced by solution polymerization using Ziegler-Natta type catalysts. That way, a moderate wide molecular mass distribution and a fairly regular molecular structure can be created [14]. Recently EPDM rubbers of improved properties are produced by metallocen catalysis as well. The EPDMs have a fair tensile strength over a wide hardness range and excellent resistance to ozone, weathering and chemical attack. Furthermore EPDM rubbers exhibit very good electrical insulation properties. Sulphure cured EPDM compounds have high compression set and are less resistant to high temperatures than peroxide cured ones.

The EPDM vulcanizates are resistant to:

- Non-mineral oil based brake fluids
- Hot water and steam
- Silicon oils and greases
- Aqueous solutions of inorganic acids, alkalis and salts
- Alkalis, glycols, ketones…

The EPDM vulcanizates are not resistant to:

- Mineral oil-based fluids and greases
- Synthetic hydrocarbon lubricants
- Organic ester-based lubricants
- Hydrocarbon fuels.

EPDM rubbers are used for a wide range of products, including sealings, o-rings, gaskets, window and door seals, wire and cable insulations, roller covers, conveyor belts, hoses and water proofing sheets [13].

3.1.2 Carbon Black (CB) as Filler Material

The term „carbon black“ (CB) refers to a group of industrial products, which will be produced by controlled burning of hydrocarbons. CBs can be grouped based on their production methods, that way thermal, furnace, channel and acetylene blacks can be differentiated. The porous CB consists of essentially spherical particles composing aggregates and agglomerates. These spherical particles are built up from elemental carbon which will be extracted of hydrocarbons during their incomplete combustion. [15]

The CBs were used since ancient times as pigment in black ink. The modern industry uses the CB as filler in elastomers, in plastics and in paints. The incorporated CB can modify the mechanical, thermal, electrical and optical properties of the corresponding materials. The importance of the CB as “active” filler is especially large by elastomers, where the incorporation of the CB improves significantly the fracture/failure behavior, the stiffness, the tearing strength and the resistance to abrasion of the elastomeric matrix. About 90% of the worldwide production of CB is used by the tire industry where the CB enhances the strength and improves the stiffness and wear characteristics of the tires. [15]

During the long history of the usage of CB different manufacturing techniques were developed. The most widely used of them is the so called Furnace-Method. During this manufacture process the feedstock/air mixture is introduced into the burning chamber and with further addition of natural gas and air incompletely burned. The residual carbon is crystallizing; the stack gas is cooled by the “quench”-water whereby the reaction is stopped. [16]

By changing and controlling process-related parameters, such as hydrocarbon/air mixture ratio, additional air supply, temperature, burning speed, addition of catalysts or change in the design of the burning chamber, the properties and quality of the CB can be tailored. That way the primary CB particle size can be varied between 10 and 80 nm. The most important parameter in view of the primary CB particle size is the retention time of the reaction gases in the burning chamber,

since with increasing retention time larger particles are forming. [16] Although it is necessary to note, that the exact process of the particle formation is unknown [17].

The carbon black is usually present as aggregate particles. Based on Transmission Electron Microscopy (TEM) and Scanning Electron Microscopy (SEM) investigations four easily discernible aggregate shape categories were classified (cf. Figure 3) [17]. The appearance of the aggregates depends on both the production method and production parameters.

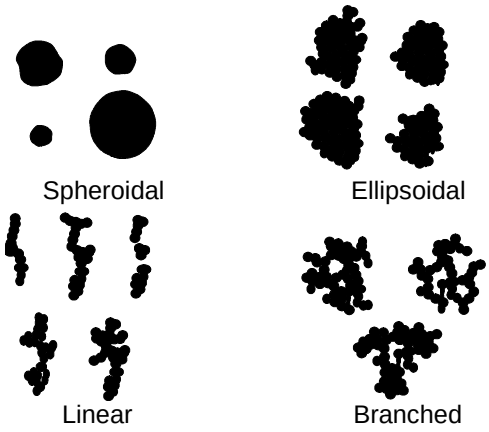

Figure 3: Different carbon black aggregate types [18]

The CB aggregates are built up from spherical carbon crystallites, which are composed of graphite like layers (cf. Figure 4). These crystallites arrange themselves into spherical particles, by keeping a more or less concentric ordering as shown in Figure 4 schematically. During the growth of these spherical particles, caused by collisions, several particles will grow together. They are connected with covalent bonds (cf. Figure 4). These aggregates can well be recognized by suitable techniques (cf. Figure 3).

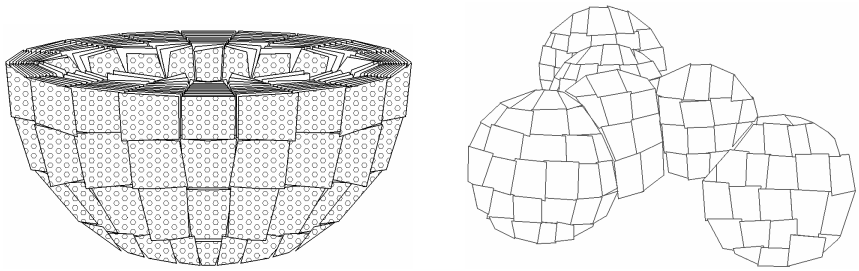

Figure 4: The structure of spherical CB particles and formation of agglomerates [18, 19, 20, 21, 22]

3.2 Material Models for Elastomers

It is of paramount importance to study the mechanical behavior of the investigated materials to be able understand the wear process. Further on the FE simulations need as input adequate material laws, which have to be determined accordingly.

3.2.1 Elasticity of Elastomers (Kuhn's Theory)

Since the rubbers are built up of long-chain polymer molecules, investigating their elasticity is unavoidable. The following description of the elastomers theory is based on reference [23]. At this point it is important to note how fascinating the results of the science are. Based only on molecular considerations it is possible to describe, however not perfectly, the behavior of a bulk rubber material which is built up from long polymer chains. The history of the molecular theorem started at the beginning of the 19th century, when Gough described his observations related to the thermo-mechanical effects of the rubber. Since then the rubber as an interesting model material has been attaining scientific interest, and many researchers (Joule, Faraday etc…) have developed theories to describe the nature of the rubber. All of these theorems are based on the description of the entropy change of polymer chains [23].

The most successful models are based on the Gaussian network theory which describes the chain length distribution within the bulk elastomer. The below introduced Kuhn model uses also the Gaussian network theory. The long chain hydrocarbon molecules by their nature are of irregular shape, if no constrain is acting on them. This "irregularity" arises from the angular freedom of the carbon-carbon bonds within the polymer chain.

Based on some further assumptions the Kuhn's theory can describe the elastic behaviors of a molecular network. Kuhn made the following simplifications and specifications when deriving the model [23]:

1. The network contains N chains per unit volume, a chain being defined as the segment of molecule between successive points of crosslinks.

2. The root-mean-square end-to-end distance for the whole assembly chains in the unstrained state is the same as for a corresponding set of free chains, and is given by the formula- $\left(\bar{r}_0^{-2}\right)^{\frac{1}{2}} = l \cdot (2n)^{\frac{1}{2}}$, (2.2.1.1)

   where l- is bond length in the polymer chain and n- is the number of bonds.
3. There is no change of volume on deformation.
4. The junction points between chains move on deformation as if they were embedded in an elastic continuum. As a result the components of length of each chain change in the same ratio as the corresponding dimension of the bulk rubber. (assumption of affine deformation)
5. The entropy of the network is the sum of the entropies of the individual chains, the latter being given by the formula- $s = c - k \cdot b^2 \cdot r_s^2$. (2.2.1.2)

   In Equation 2.2.1.2 c- is an arbitrary constant which contains the size of that small volume element where the end of the chain possibly bewares, $b^2 = \frac{3}{2 \cdot n \cdot l^2}$, r_s- is the distance between the chain ends and k-is the Boltzmann-constant.

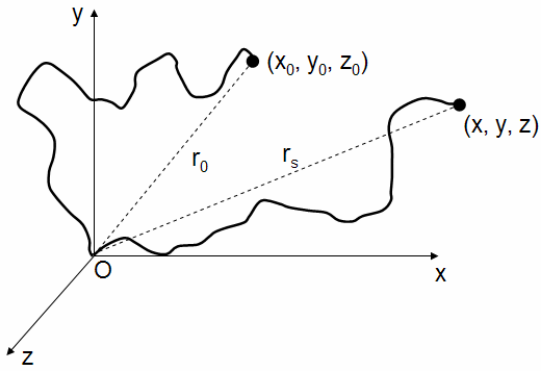

Figure 5: A polymer chain in its unstrained (indexed by 0) and strained state

Let us consider an individual chain (Figure 5). The entropy of the chain in the original state (s_0) and in the strained state (s) can be described as follows:

$$s_0 = c - k \cdot b^2 \cdot r_0^2 = c - k \cdot b^2 \cdot \left(x_0^2 + y_0^2 + z_0^2\right), \quad (2.2.1.3)$$

$$s = c - k \cdot b^2 \cdot \left(\lambda_1^2 \cdot x_0^2 + \lambda_2^2 \cdot y_0^2 + \lambda_3^2 \cdot z_0^2\right). \quad (2.2.1.4)$$

In Equation 2.2.1.4 λ_1, λ_2 and λ_3 are the strain ratios in x, y and z directions respectively. In this interpretation λ_1 can be determined as follows: $\lambda_1 = \frac{x_0 + \Delta x}{x_0}$. In the same way can be determined λ_2 and λ_3 for the y and z directions.

Continuing the train of thought, the total entropy change of the upper strained chain due to the deformation will therefore be:

$$\Delta s = s - s_0 = -k \cdot b^2 \cdot \left\{ \left(\lambda_1^2 - 1\right) \cdot x_0^2 + \left(\lambda_2^2 - 1\right) \cdot y_0^2 + \left(\lambda_3^2 - 1\right) \cdot z_0^2 \right\}. \quad (2.2.1.5)$$

By the summation of the expression 2.2.1.5 we can get he total entropy change of the unit network volume which contains N chains. Assuming the same molecular weight for all the chains, the parameter b is constant, and we may write for the total entropy deformation:

$$\Delta S = \sum \Delta s = -k \cdot b^2 \cdot \left\{ \left(\lambda_1^2 - 1\right) \cdot \sum x_0^2 + \left(\lambda_2^2 - 1\right) \cdot \sum y_0^2 + \left(\lambda_3^2 - 1\right) \cdot \sum z_0^2 \right\}. \quad (2.2.1.6)$$

The directions of the chain vectors r_0 are entirely random in the unstrained state. Because of it there will be no preference for the x, y or z directions and hence,

$$\sum x_0^2 = \sum y_0^2 = \sum z_0^2 = \frac{1}{3} \sum r_0^2 = \frac{1}{3} N \cdot \bar{r}_0^2, \quad (2.2.1.7)$$

where $\bar{r}_0^2$ is the mean square distance of the chain ends in the unstrained state. Using Eqns. 2.1.1.6 and 2.2.1.7 we can write:

$$\Delta S = -\frac{1}{3} \cdot N \cdot k \cdot b^2 \cdot \bar{r}_0^2 \cdot \left(\lambda_1^2 + \lambda_2^2 + \lambda_3^2 - 3\right). \quad (2.2.1.8)$$

Because the mean-square chain vector length in the unstrained state is $\bar{r}_0^2 = \frac{3}{2 \cdot b^2}$ Eqn. 2.2.1.8 gives

$$\Delta S = -\frac{1}{2} \cdot N \cdot k \cdot \left(\lambda_1^2 + \lambda_2^2 + \lambda_3^2 - 3\right). \quad (2.2.1.9)$$

As the work needed to be done during stretching of a molecule chain is proportional to the entropy change ($W = -T \cdot \Delta S$), considering Eqn. 2.2.1.9 yields:

$$W = \frac{1}{2} \cdot N \cdot k \cdot T \cdot \left(\lambda_1^2 + \lambda_2^2 + \lambda_3^2 - 3\right). \quad (2.2.1.10)$$

Using the expression 2.2.1.10 it is possible to derive the stresses proper to the strain- or stress-states for different deformation modes, such as simple shear, uniaxial tension, compression etc... Expression 2.2.1.9 can be written as:

$$W = \frac{1}{2} \cdot G \cdot \left(\lambda_1^2 + \lambda_2^2 + \lambda_3^2 - 3\right) \quad (2.2.1.11)$$

where $G = N \cdot k \cdot T$ is the elastic constant of the material and it is equivalent to the shear modulus. G depends on the N number of chains per unit volume, which itself is determined as the degree of crosslinking M_c. The appropriate relationship is

$$G = N \cdot k \cdot T = \frac{\rho \cdot R \cdot T}{M_c} \qquad (2.2.1.12)$$

where ρ –is the density of the rubber and R –is the universal gas constant per mol. The expression 2.2.1.11 shows that based on the molecular rubber elasticity theory, the degree of crosslinking M_c together with the density of the rubber determines the elastic properties of the cured system. A further frequently used measure to characterize the elastomer network is the crosslink density ν_C:

$$\nu_C = \frac{\rho}{M_C} \qquad (2.2.1.13)$$

As it was shown, the elastic behavior of an elastomer can be directly derived from the M_c or from the ν_C. Because of it these parameters are often represented in the literature as very important material characteristics. Therefore it is worthwhile to show and explain shortly the correlations which are usually used to determine the M_c and ν_C. These values are often expressed from the tensile modulus (E), which was determined at a proper small tensile strain (< 1%) at a given temperature above the glassy temperature (T_g). As it is known, the relationship between the shear (G) and the tensile modulus (E) is

$$G = \frac{E}{2 \cdot (1 + \nu)}, \qquad (2.2.1.14)$$

where ν-is the Poisson ratio of the elastomer. But as the elastomers are assumed to be incompressible, ν will be equal to 0.5 and 2.2.1.14 gives

$$3 \cdot G = E. \qquad (2.2.1.15)$$

The substitution of 2.2.1.15 into 2.2.1.12 yields

$$M_C = \frac{3 \cdot \rho \cdot R \cdot T}{E}. \qquad (2.2.1.16)$$

Using Equations 2.2.1.16 and 2.2.1.13 the determined crosslink density for elastomers is usually in the range of several thousands in mol/cm^3. As mentioned above this early molecular theory can not perfectly describe the real behavior of the rubbers (cf. Figure 6) but e pretty good correlation is found in small strain ranges.

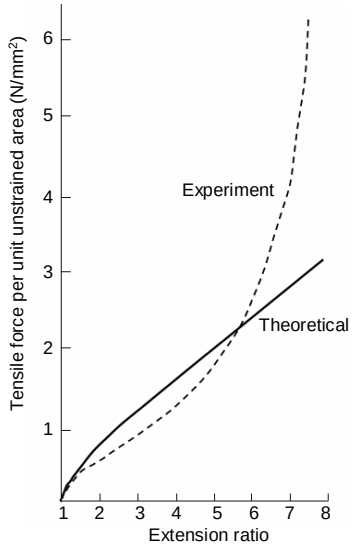

Figure 6: Simple extension. Comparison of experimental curve with theoretical form (Equation: 2.2.1.11) (G=0.39 Nmm^{-2}) [23]

3.2.2 The Mooney-Rivlin constitutive model

The following summary is based on reference [23]. Mooney's theory (1940) is the earliest significant phenomenological description of large elastic deformations, which has played a dominant part in all later works in the related research field. It has to be noted that this theory appeared some years before Kuhn's (Gaussian statistical) theory. Mooney's description is based not on molecular or structural considerations but purely on mathematical reasoning. The special form of Mooney's theory (see Equation 2.2.2.1) is based on the following assumptions:

- the rubber is incompressible and isotropic in the unstrained state.
- Hooke's law is obeyed in simple shear, or in simple shear superimposed in a plane transverse to a prior uniaxial extension or compression.

On the basis of the upper assumptions Mooney derived, by purely mathematical arguments, the following strain-energy function

$$W = C_1 \cdot \left(\lambda_1^2 + \lambda_2^2 + \lambda_3^2 - 3\right) + C_2 \cdot \left(\frac{1}{\lambda_1^2} + \frac{1}{\lambda_2^2} + \frac{1}{\lambda_3^2} - 3\right) \qquad (2.2.2.1)$$

which contains two elastic constants C_1 and C_2. The first term in this expression corresponds identically to Kuhn's theory; see Equation 2.2.1.11 (derived from the Gaussian network theory) with

$$2 \cdot C_1 \equiv G = N \cdot k \cdot T = \frac{\rho \cdot R \cdot T}{M_c}. \qquad (2.2.2.2)$$

The Gaussian theory is thus the particular case of the Mooney theory corresponding to C_2=0.

Mooney's special mathematical model was refined by Rivlin, whose formulation is more general. When defining constitutive relations for isotropic solids it is useful to use deformation measures which are independent of the basis coordinates. The principal stretches provide one such choice. In finite elasticity theories the most commonly used deformation measure is the left Cauchy-Green strain tensor

$$\underline{\underline{B}} = \underline{\underline{F}}^{T} \cdot \underline{\underline{F}}, \qquad (2.2.2.3)$$

where F is the deformation gradient [24]. The F deformation gradient can be decomposited in two second-order tensors based on the polar decomposition theorem. That way F can be expressed as the multiplication of an orthogonal and a positive definite symmetric tensor, i.e.

$$\underline{\underline{F}} = \underline{\underline{R}}\,\underline{\underline{U}}. \qquad (2.2.2.4)$$

In 2.2.2.4 $\underline{\underline{R}}$ is an orthogonal tensor, i.e representing a rotation; the other $\underline{\underline{U}}$ tensor is the right stretch tensor which is a positive definite and symmetric tensor. Because pure rotation should not induce any stresses in a deformable body, some rotation-independent deformation tensors are used in mechanics, such as the above mentioned left Cauchy-Green deformation tensor. As a rotation followed by its inverse rotation leads to no change due to its orthogonality $\left(\underline{\underline{R}}\underline{\underline{R}}^{T} = \underline{\underline{R}}^{T}\underline{\underline{R}} = 1\right)$ we can eliminate the rotation by multiplying $\underline{\underline{F}}$ by its transpose [25]. So Equation 2.2.2.3 can be expressed as:

$$\underline{\underline{B}} = \underline{\underline{F}}^{T} \cdot \underline{\underline{F}} = \underline{\underline{U}}^{2}. \qquad (2.2.2.5)$$

Since $\underline{\underline{U}}$- being a stretch tensor, described in the basis of principal stresses, it contains only the hydrostatic strain components and is determined as follows:

$$\underline{\underline{U}} = \begin{bmatrix} \lambda_1 & 0 & 0 \\ 0 & \lambda_2 & 0 \\ 0 & 0 & \lambda_3 \end{bmatrix}. \qquad (2.2.2.6)$$

Constituting Equation 2.2.2.6 into Equation 2.2.2.5, one can get for $\underline{\underline{B}}$ the following:

$$\underline{\underline{B}} = \begin{bmatrix} \lambda_1^2 & 0 & 0 \\ 0 & \lambda_2^2 & 0 \\ 0 & 0 & \lambda_3^2 \end{bmatrix}. \qquad (2.2.2.7)$$

Thus the deformation state can be described with the strain invariants, Rivlin has chosen the invariants of the left Cauchy-Green strain tensor for the creation of a general formulation of the Mooney model. The three (I_1, I_2 and I_3) scalar invariants of the strain tensor are determined as it is shown in Equations 2.2.2.8, 2.2.2.9 and 2.2.2.10 respectively.

$$I_1 = \mathrm{tr}(\underline{\underline{B}}) = \lambda_1^2 + \lambda_2^2 + \lambda_3^2 \qquad (2.2.2.8)$$

$$I_2 = \frac{1}{2}\left(\mathrm{tr}\left(\underline{\underline{B}}^2\right) - \mathrm{tr}\left(\underline{\underline{B}}\right)^2\right) = \lambda_1^2 \cdot \lambda_2^2 + \lambda_2^2 \cdot \lambda_3^2 + \lambda_3^2 \cdot \lambda_1^2 \qquad (2.2.2.9)$$

$$I_3 = \det(\underline{\underline{B}}) = \lambda_1^2 \cdot \lambda_2^2 \cdot \lambda_3^2 \qquad (2.2.2.10)$$

These expressions are independent from the choice of coordinate axes and any more complex function of λ_i can be always expressed in terms of these three basic forms. Assuming the incompressibility of the rubber material further equation can be introduced:

$$I_3 = \lambda_1^2 \cdot \lambda_2^2 \cdot \lambda_3^2 = 1. \qquad (2.2.2.11)$$

This enables to simplify the 2nd invariant (Equation 2.2.2.9) as follows:

$$I_2 = \frac{1}{\lambda_1^2} + \frac{1}{\lambda_2^2} + \frac{1}{\lambda_3^2}. \qquad (2.2.2.12)$$

The most general formulation of Mooney's model, the well known Mooney-Rivlin material model is given by Equation 2.2.2.13. This formulation allows us to create a material model using optional number of material constants. The applied indexes and exponents result that for zero strain the strain-energy function becomes automatically zero (i=0, j=0, I_1=I_2=3, → C_{00}=0).

$$W = \sum_{i=0,j=0}^{\infty} C_{ij}\left(I_1 - 3\right)^i \cdot \left(I_2 - 3\right)^j \qquad (2.2.2.13)$$

The first one parameter Mooney-Rivlin model, where i=1 and j=0 provides the 2.2.2.14 expression which is identical with Kuhn's formulation, see Equations 2.2.1.10 and 2.2.1.11.

$$W = C_{10}\left(I_1 - 3\right) = C_{10}\left(\lambda_1^2 + \lambda_2^2 + \lambda_3^2 - 3\right) \qquad (2.2.2.14)$$

The second one parameter form of 2.2.2.13, where i=0 and j=1 results the expression 2.2.2.15.

$$W = C_{01}\left(I_2 - 3\right) = C_{01}\left(\frac{1}{\lambda_1^2} + \frac{1}{\lambda_2^2} + \frac{1}{\lambda_3^2} - 3\right) \qquad (2.2.2.15)$$

However this equation has no obvious application for elastomers, the combination of Equations 2.2.2.14 and 2.2.2.15 (where i=1 and j=1) results the already known form of the Mooney material model (see Equation 2.2.2.16).

$$W = C_{10}(I_1 - 3) + C_{01}(I_2 - 3) \qquad (2.2.2.16)$$

In the elasticity theories of rubbers the usually applied expression to describe the strain state is shown in Equation 2.2.2.17.

$$\lambda_i = \frac{L_0 + \Delta L_i}{L_0} = 1 + \frac{\Delta L_i}{L_0} = 1 + \varepsilon_i, \qquad (2.2.2.17)$$

where $\varepsilon = \Delta L / L_0$. Expression 2.2.2.17 provides positive values for the strain, even when tension or compression takes places. The only difference between the compression and tension strain values is that in the case of tensile strains the value of λ is higher than one and in compression its value is between zero and one. The higher the tension the larger the value of λ is and the higher the compression strain the closer the λ value to zero will be. Equation 2.2.2.17 can be written in another form, which describes simpler the correlation between the strain ratios and dimensional changes (see Equation 2.2.2.18).

$$\lambda_i \cdot L_0 = L_0 + \Delta L_i = L_i \qquad (2.2.2.18)$$

Thus within this work the Mooney-Rivlin model will be fitted to uniaxial-tension and uniaxial-compression test results, next it will be shown which further considerations are needed to determine the Mooney-Rivlin parameters based on test results.

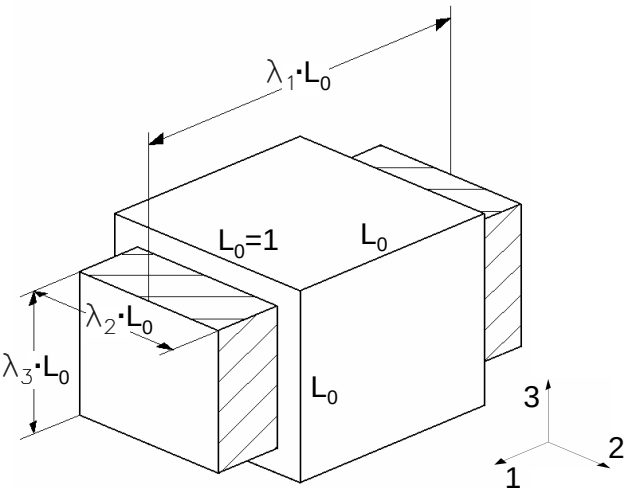

Figure 7: Unit cube in unstrained state and under uniaxial tensile strain (shaded)

Considering uniaxial tension of an incompressible unit cube (cf. Figure 7), due to the constancy of volume, one can write the equation 2.2.2.19:

$$L_1 \cdot L_2 \cdot L_3 = L_0^3 . \qquad (2.2.2.19)$$

The symmetry of the deformations in the directions “2” and “3” allows us to simplify the problem because of the equality of the deformed edge length L_2 and L_3, ($L_2 = L_3 \equiv L_{2,3}$ and similar $\lambda_2 = \lambda_3 = \lambda_{2,3}$) and we can rewrite 2.2.2.19 as follows:

$$L_1 \cdot L_{2,3}^2 = L_0^3 . \qquad (2.2.2.20)$$

To eliminate $L_{2,3}$ we can express it as the function of λ_1 and L_0^2. This replacement is to see in Equation 2.2.2.21:

$$L_{2,3} = L_0 + \Delta L_{2,3} = \sqrt{\frac{L_0^3}{L_1}} = \sqrt{\frac{L_0^3}{L_0 + \Delta L_1}} = \sqrt{\frac{L_0^2}{\lambda_1}} . \qquad (2.2.2.21)$$

Continuing the train of thought similar to $L_{2,3}$, $\lambda_{2,3}$ can be replaced by λ_1 (see Equation 2.2.2.22):

$$\frac{L_0 + \Delta L_{2,3}}{L_0} = \lambda_{2,3} = \sqrt{\frac{L_0^2}{\lambda_1 \cdot L_0^2}} = \frac{1}{\sqrt{\lambda_1}} . \qquad (2.2.2.22)$$

That way only one strain component remains (λ_1) which needs to be substituted into Equation 2.2.2.16, the other two components (λ_2 and λ_3) can be expressed by λ_1. As further simplification of the formulation we can write that:

$$\lambda_1 = \lambda \qquad (2.2.2.23)$$

and:

$$\lambda_2 = \lambda_3 = \frac{1}{\sqrt{\lambda}} . \qquad (2.2.2.24)$$

To clarify the notations it needs to be note that due to the equality of 2.2.2.1 and 2.2.2.16 we can write that $C_1 \equiv C_{10}$ and $C_2 \equiv C_{01}$. With the substitution of 2.2.2.23 and 2.2.2.24 into 2.2.2.1 or into 2.2.2.16 we can gat the special form of the Mooney-Rivlin constitutive material for uniaxial tension (or compression):

$$W = C_1\left(\lambda^2 + \frac{2}{\lambda} - 3\right) + C_2\left(\frac{1}{\lambda^2} + 2\lambda - 3\right). \qquad (2.2.2.25)$$

As the strain energy density (W) function can be expressed in integral form (see Equation 2.2.2.26), a simple differential equation will provide the expression of the needed stress function (see Equation 2.2.2.27).

$$W = \int \sigma d\varepsilon \qquad (2.2.2.26)$$

$$\sigma = \frac{dW}{d\varepsilon} = \frac{dW}{d\lambda} , \qquad (2.2.2.27)$$

where σ is the stress, a measure of the acting force per unit area, σ=F/A. Solving the derivation of 2.2.2.27, one can get an easily soluble stress function (see Equation 2.2.2.28). For the constitutive material model fitting process the two parameters of 2.2.2.28 (C_1 and C_2) need to be varied to find the optimal Mooney-Rivlin model which is able to describe the investigated material.

$$\sigma = 2\left(\lambda - \frac{1}{\lambda^2}\right)\left(C_1 + \frac{C_2}{\lambda}\right) \qquad (2.2.2.28)$$

As it to see from the upper derivation process the Mooney-Rivlin constitutive model strongly depends on the strain state. Therefore one should be careful with the use of this material model. At least two kinds of tests are needed (uniaxial and biaxial tension, or uniaxial tension and compression, etc…) to have acceptable constitutive model for analytical or for FE calculations. In this thesis uniaxial tension and uniaxial compression tests were carried out for fitting the two parameter Mooney-Rivlin model for the elastomers used.

3.3 Viscoelasticity

In the former chapter the characteristic nonlinear mechanical behavior of the elastomeric materials was discussed. Viscoelasticity is a further important characteristic for elastomers more exactly for all polymeric materials. One can differentiate basically between three phenomena which are related to the viscoelasticity. These are the hysteresis, the stress relaxation and the creep. Though all of the mentioned viscoelastic phenomena are linked with the molecular structure they are discussed always separately because of the related difficult mathematical formulations. Not only the mathematical descriptions but also the test methods which are usually used to access the viscoelastic behavior of polymers, are different.

For the determination of the hysteretic losses usually dynamic-mechanical-thermal-analysis (DMTA) is used, where a sinusoidal stress or strain is applied onto the specimen and the mechanical response of the material is registered. During the DMTA test the frequency and the amplitude of the load, as well as the test temperature can be varied. Choosing an excitation frequency and varying the temperature the DMTA tests deliver information on the temperature dependence of the complex modulus (E^*) of the material. The (E^*) can be deconvoluted as the sum of the storage (E´) and loss moduli (E´´). The mechanical loss factor ($\tan\delta$) is the quotient of E´´ and E´. The DMTA data are often used to characterize the molecular

or phase structure of the investigated polymer and to detect the glass transition temperature (T_g) of the material. T_g represents the transition temperature between the glassy and rubbery state of the material, where the loss factor reaches its maximum value. The simultaneous variation of the temperature and the frequency during DMTA tests (frequency and temperature sweep) is scarcely followed. As a result of the frequency and temperature sweeps one can get for example the storage modulus (E´) vs. frequency curves which were measured at different temperatures. Aftermath these curves, may be used to create the storage modulus vs. frequency master curve of the material by adopting the WLF-theory [28, 29, 30, 31]. The mathematical description of this master curve can serve as material model, considering the viscoelastic behavior of the material. In this chapter the related process will be detailed.

During stress relaxation tests a prescribed strain is applied on the specimen and the decrease of the evolved reaction force is detected as a function of time. This measurement can be repeated at different temperatures. From the relaxation modulus vs. relaxation time curves, which were measured at different temperatures, one can create a relaxation modulus master curve, using the WLF theory.

The creep tests are similar to the stress relaxation test. The difference between the creep and the stress relaxation measurements is that not a constant strain but a constant stress is applied onto the specimen during creep. That way a slowly increasing strain (creep) can be detected with the testing time. To characterise the creep behavior of a polymer, the measure of creep or plasticity compliance (J_C) is introduced. The J_C is determined as quotient of the total strain at a particular time and the applied constant stress; $J_C = \frac{\varepsilon(t)}{\sigma_0}$ [26]. The J_C vs. time curves can be measured at different temperatures and the creation of a J_C vs. time master curve is also possible.

Suitable mechanical models can be found for DMTA, stress relaxation and creep tests however different models (usually of phenomenological nature) are used for them. It is important to note, that these mechanical models are not compatible with each other. The material model which describes the creep behavior of a given polymer can not describe the stress relaxation or hysteretic behavior of the same material and vice versa. On the other hand, the storage modulus and the relaxation modulus master curves of a material can be described using the same models.

3.3.1 DMTA Basics

The following description of the DMTA testing process is based on the testing method of the used QDMA (TA Instruments-Waters LLC, New Castle, USA) machine [27]. During the dynamic mechanical thermal analysis, an oscillatory load (strain or stress) is applied to the material and the resulting stress (or strain) is measured. Ideal elastic materials follow Hooke's law which means that the arising stress and the magnitude of the applied strain are proportional. Further on, one can not detect any phase shift between the applied load and the response of the material, *i.e*., the strain will be in phase with the stress (the phase angle δ will be 0°, see Figure 8-a). For ideal fluids (viscous materials) Newton's law is obtained; *i.e.*, the stress is proportional to the strain rate. It means that the load signal will lead the response signal of the material shifted by 90° (see b in Fig ure 8-b).

Generally every (real) materials exhibit a mechanical response being a mixture of elastic and viscous contributions. This phenomenon is especially significant by polymeric materials thus, they are termed viscoelastic. For a polymeric material, the measurable phase angle (δ), during DMTA test, lies somewhere between 0° and 90° (as depicted in Figure 9).

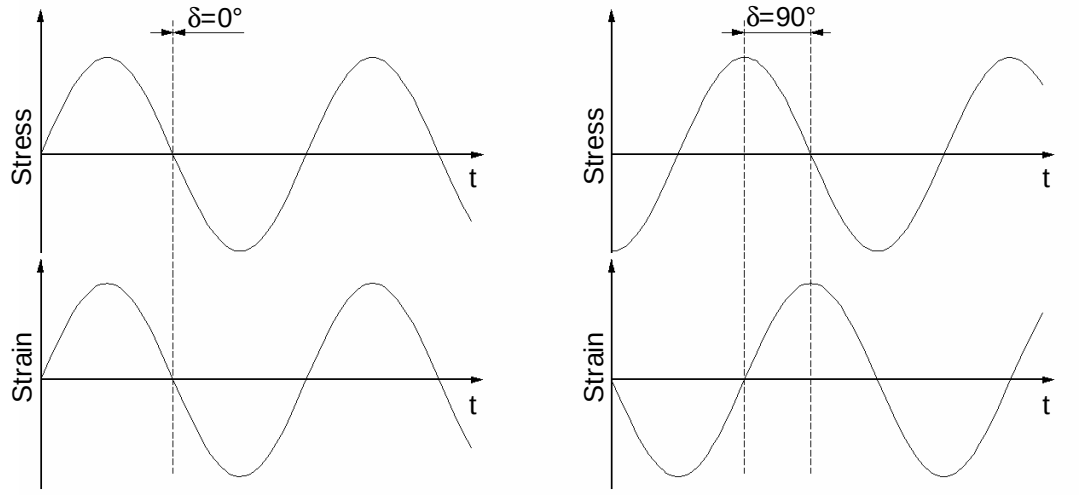

100% Elastic
a;

100% Viscous
b;

Figure 8: Response of an ideal solid (a) and an ideal fluid material (b) for dynamic excitation [27]

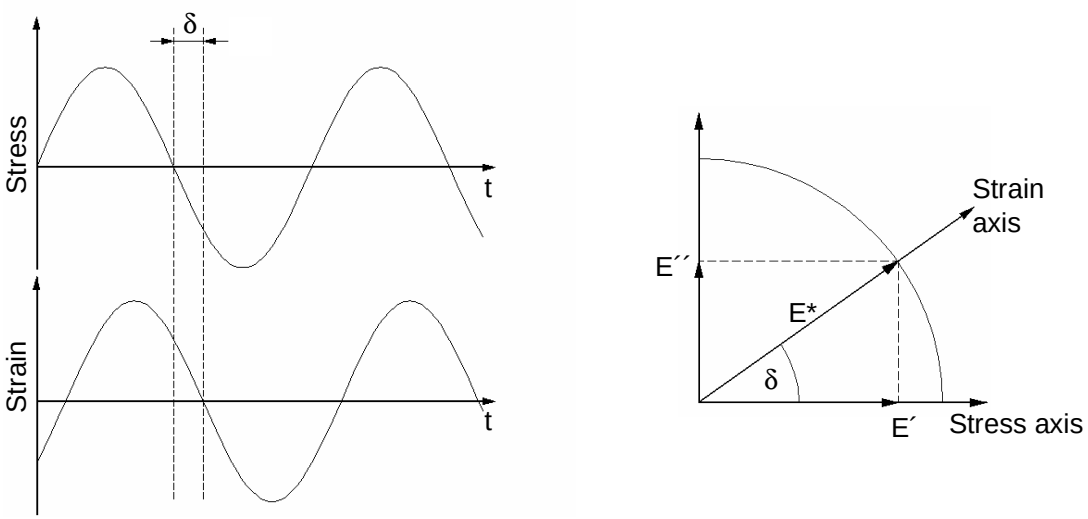

Figure 9: Response of a polymeric material for dynamic excitation and the vector depiction of the E´ and E´´. Note: E´ is the storage modulus and E´´ is the loss modulus, these are the real (elastic) and imaginary (viscous) parts of the measured complex modulus [27].

The modulus is defined as the ratio of stress over strain in a strain state in which Hooke's law is obeyed for the material. Thus the resultant stress in a viscoelastic material due to dynamic excitation is the complex stress (σ*), the complex modulus (E*) can be determined applying Hooke's law (see Equation 2.3.1.1).

$$E^* = \frac{\sigma^*}{\varepsilon}. \qquad (2.3.1.1)$$

The complex modulus contains both elastic and viscous responses of the material. The great advantage of this type of dynamic testing is, that with the help of the measured phase angle, the calculated complex modulus (or by the same way the complex stress) can be deconvoluted into two parts:

$$E^* = E' + i \cdot E'' \text{ or } \sigma^* = \sigma' + i \cdot \sigma''. \qquad (2.3.1.2)$$

In Equation 2.3.1.2 σ´- is the elastic stress which is in phase with the strain, σ´´ is the viscous stress which is in phase with the strain rate (90° out of phase with the strain). The storage (E´) and the loss modulus (E´´) can be calculated directly from the elastic and viscous stresses respectively as it is shown in 2.3.1.4 and in 2.3.1.6. The complex modulus can be deconvoluted into elastic and loss modulus parts, also by the determination of its real and imaginary components (see Equations 2.3.1.5 and in 2.3.1.7). For this one needs the phase angle (δ) which is determined as follows:

$$\delta = 2\pi \cdot f \cdot \Delta t, \qquad (2.3.1.3)$$

where f – is the frequency of the dynamic excitation and Δt – is the time delay between stress and strain (cf. Figure 9).

A summary of the calculations are as follows:

for the storage modulus;

$$E' = \frac{\sigma'}{\varepsilon} \qquad (2.3.1.4)$$

or

$$E' = E^* \cdot \cos\delta \qquad (2.3.1.5)$$

for the loss modulus;

$$E'' = \frac{\sigma''}{\varepsilon} \qquad (2.3.1.6)$$

or

$$E'' = E^* \cdot \sin\delta\,. \qquad (2.3.1.7)$$

and for the loss factor:

$$\tan\delta = \frac{E''}{E'}\,. \qquad (2.3.1.8)$$

The stiffness of a specimen, measured in the tension clamp (i.e. this configuration was applied), is calculated by:

$$K = \frac{A_{def} \cdot E}{L}, \qquad (2.3.1.9)$$

where K – is the stiffness or spring constant, E – is the elastic modulus, A_{def} - is the actual (deformed) cross-sectional area of the sample and L - is the length of the specimen. Or otherwise the modulus can be written by:

$$E = K \cdot \frac{L}{A_{def}}\,. \qquad (2.3.1.10)$$

Similar to Hooke's law, the calculation of the engineering stress (σ_0) and strain (ε_0) delivers only for those measurements good results, where the incremental displacement of the specimen is a very small percentage of its initial length (see Equations 2.3.1.11 and 2.3.1.12). It is the right place to note that in our case the applied tension strain was 0.01 % which fulfils this prerequisite. The nominal or engineering stress and strain are described by:

$$\sigma_0 = \frac{F}{A_0} \qquad (2.3.1.11)$$

and

$$\varepsilon_0 = \frac{\Delta L}{L_0}, \qquad (2.3.1.12)$$

where σ_0 - is the nominal stress and ε_0 - is the nominal strain, F – is the applied force, ΔL - is the cumulative change in specimen length, L_0 - is the initial specimen length and A_0 - is the initial cross-sectional area of the specimen.

During DMTA tests the specimen stiffness (K) will be determined. For dynamic, oscillation experiments K is defined as the ratio of the applied force (in Newtons) over the amplitude (in meters). Using the phase angle the storage and loss stiffness (K' and K") can be determined. The tan δ is calculated as the ratio of K" over K'. Storage and loss moduli are then calculated by multiplying the "raw stiffness" measurements by the appropriate geometry factors [27].

In multifrequency controlled strain mode, the frequency and the temperature are changing, while the amplitude of oscillation is constant. Frequency and temperature sweeps are performed to observe changes in the storage and loss moduli against the excitation frequency and against the temperature. Based on the frequency and temperature sweeps the related DMTA curves are suitable to generate proper master curves exploiting the WLF time-temperature superposition principle as it will be shown in Chapter 3.3.2.

3.3.2 WLF

As it was mentioned before the most valuable results are DMTA data, because these contain the temperature as well as the frequency dependences of the material properties. In the following section the generation of the storage modulus vs. frequency master curve will be detailed. The outcome will serve later for a viscoelastic material model after proper fitting procedure. To be able to apply the time-temperature equivalence (WLF- equation) we need the temperature and frequency dependence of the storage modulus for a given material as it is shown in Figure 10.

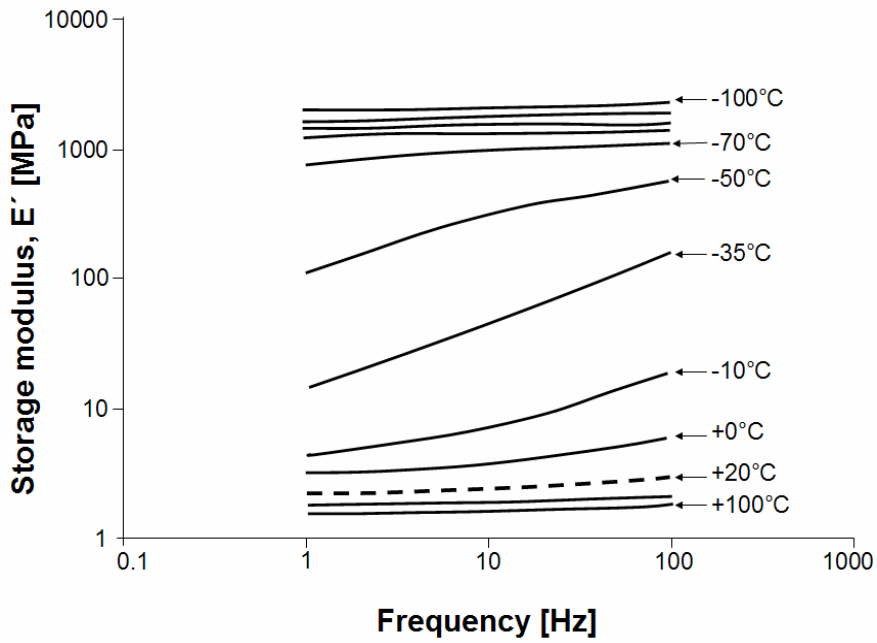

Figure 10: Example for the temperature and frequency dependence of the storage modulus for a given material

In Figure 10 one can see Storage modulus (E´) vs. Frequency curves which were measured at different temperatures. As it is clearly to see the highest E´ values were determined at the lowest, while the lowest modulus values at the highest temperatures. The largest change in the E´ vs. frequency curves is to observe at the vicinity of the T_g. For the creation the master curve one need to chose a reference curve from these E´ vs. Frequency curves. This reference curve will be fixed and all other E´ vs. Frequency traces shifted compared to it in the frequency domain by an adequate temperature dependent shift factor (a_T) (see Figure 11). The shift factors are chosen so that finally the shifted curves give a continuous master curve. After this shifting procedure one can get a continuous master curve in the frequency domain which covers a much wider frequency range than the measured one (cf. Figure 10).

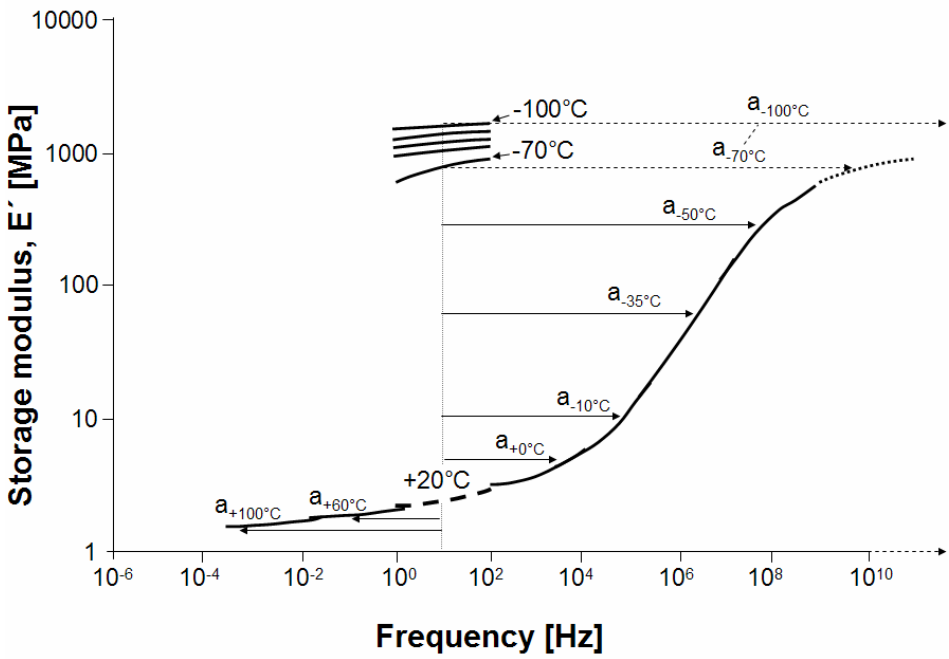

Figure 11: Shifting procedure with a temperature dependent shift factors (a_T), reference curve is the E´ vs. frequency curve measured at 20℃.

However during the creation of the master curve the shift factors are defined arbitrarily though their should fulfil the requirements of the WLF theory. If the shifting procedure is not within the framework of the time-temperature equivalence theory, then the master curve was generated falsely [28, 29, 30, 31]. The shift factors (a_T) can be depicted versus the temperature as it is displayed in Figure 12. The series of the experimentally defined shift factors need to fit to the WLF theory (see Equation 2.3.2.1). However the simple WLF description works mostly only in a relatively narrow temperature range around the T_g (see Figure 12), using the Arrhenius supplement the modified WLF equation one can describe the whole log a_T – temperature curve (Equations 2.3.2.2 and 2.3.2.3) [32].

$$\log a_T = \frac{-K_1 \cdot (T - T_{ref})}{K_2 + (T - T_{ref})} \qquad T_C^L \le T \le T_C^O \quad (2.3.2.1)$$

$$\log a_T = \frac{-K_1 \cdot (T_C^L - T_{ref})}{K_2 + (T_C^L - T_{ref})} - \frac{M \cdot A_E^L}{R \cdot T_C^L} \cdot \frac{(T - T_{ref}) + (T_{ref} - T_C^L)}{T_{ref} + (T - T_{ref})} \qquad -\infty \le T \ge T_C^L \quad (2.3.2.2)$$

$$\log a_T = \frac{-K_1 \cdot (T_C^U - T_{ref})}{K_2 + (T_C^U - T_{ref})} - \frac{M \cdot A_E^U}{R \cdot T_C^U} \cdot \frac{(T - T_{ref}) + (T_{ref} - T_C^U)}{T_{ref} + (T - T_{ref})} \qquad T_C^U \le T \le +\infty \quad (2.3.2.3)$$

where: K_1, K_2 - are constants depending on the material and the temperature, T – is the temperature of the measured curve, T_{ref} – is the reference temperature, T_C^U - is

the upper validity limit of WLF equation, T_C^L – is the lover validity limit of WLF equation, A_E^U – is a constant depending on material and reference temperature (over upper limit), A_E^L – is a constant depending on material and reference temperature (under lover limit), M – is constant (lg(e)=0,434294) and R- is the universal gas constant (8314.41 J/kmol·K).

Another important aspect of the WLF-Arrhenius description is that via the related Log a_T-temperature function the master curve can be transformed to other reference temperatures. This helps us to use temperature- and frequency-dependent material models.

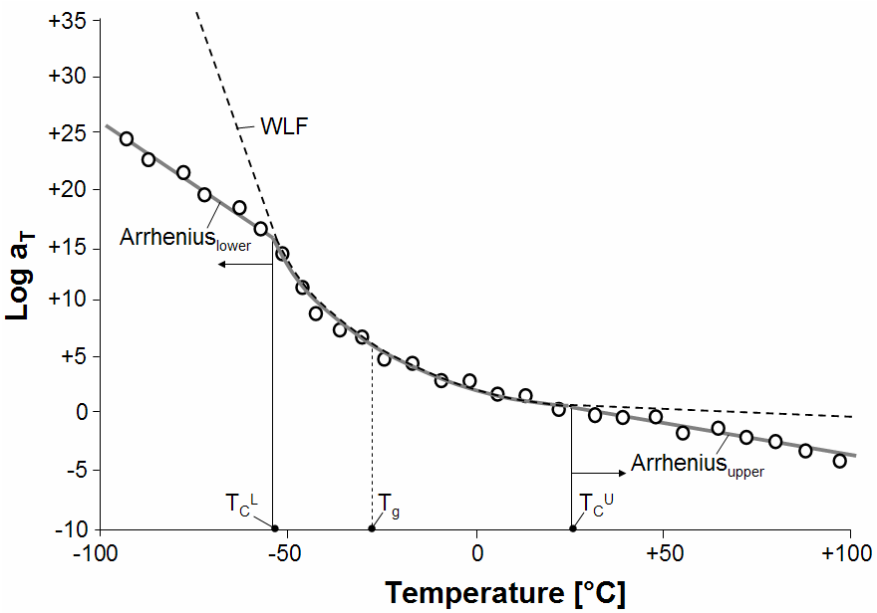

Figure 12: Fitting a WLF and a WLF-Arrhenius curve to the experimentally defined shift factors (showed by points).

3.3.3 Generalized Maxwell-model

The above described theory is the scientific background of the production of the master curve reflecting the storage modulus vs. frequency trace at a proper reference temperature. Next a 15-term (N=1..15) viscoelastic model (see Figure 13) will be introduced the behavior of which describes that of the created master curve. It is the right place to mention that in different literatures the depicted viscoelastic model in Figure 13 is termed as Maxwell, Zener, or Standard Solid model. Further it will be referred to as generalized Maxwell model. This generalized Maxwell model is built up from parallel connected spring-dashpot pairs which are additionally parallel connected with a single spring. E_i represents the elastic modulus of rigidity for the i-th

spring, η_i is the kinematic viscosity and E_∞ is the plateau modulus of the modelled elastomer E´ at Figure 11 (the smallest frequencies or at the highest temperatures).

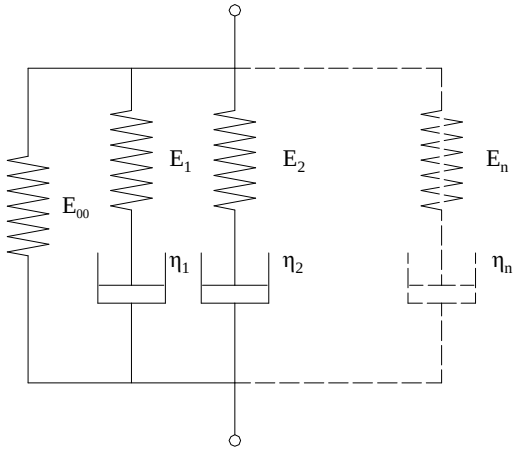

Figure 13: The generalised Maxwell model

As it was mentioned before, the relaxation modulus and the DMTA test results (DMTA) are to describe by the same viscoelastic models. Without derivation, the relaxation modulus of the generalised Maxwell model can be described as follows [32,33,34]:

$$E(t,T_{ref}) = E_\infty + \sum_{i=1}^{N}(E_i)\cdot e^{-\frac{t}{\tau_i}}, \qquad (2.3.3.1)$$

and the expression of the complex modulus (E*) as function of the applied frequency can be written:

$$E^* = E_\infty + \sum_{i=1}^{N} E_i \frac{\omega^2\tau_i^2 + i\omega\tau_i}{1+\omega^2\tau_i^2}, \qquad (2.3.3.2)$$

where ω is the applied frequency and $\tau_i = \frac{\eta_i}{E_i}$ is the relaxation time constant of the i-th spring-dashpot pair.

The Equation 2.3.3.2 can be deconvoluted into two parts, namely into a real (storage modulus, Equation 2.3.3.3) and imaginary parts (loss modulus, Equation 2.3.3.4):

$$E' = E_\infty + \sum_{i=1}^{N} E_i \frac{\omega^2\tau_i^2}{1+\omega^2\tau_i^2} \qquad (2.3.3.3)$$

$$E'' = \sum_{i=1}^{N} E_i \frac{\omega\,\tau_i}{1+\omega^2\tau_i^2}. \qquad (2.3.3.4)$$

During the fitting process next the equation 2.3.3.3 will be used to describe the storage modulus vs. frequency master curve. For this purpose, one needs to define the right series of the fifteen τ_i-E_i pairs, the so called Prony series. For this

optimisation, fitting process, the ViscoData software was used [35]. However the ViscoData software uses the following alternative formulations for the description of the storage and of the loss modulus:

$$E'(\omega, T_{ref}) = E_0\left[1 - \sum_{i=1}^{N} e_i \frac{1}{1+\omega^2\tau_i^2}\right] \qquad (2.3.3.5)$$

$$E''(\omega, T_{ref}) = E_0 \cdot \sum_{i=1}^{N} e_i \frac{\omega\tau_i}{1+\omega^2\tau_i^2} \qquad (2.3.3.6)$$

The values of constants e_1-e_{15} are derived from the following equation as interpreted by the curve adjustment software:

$$e_i = \frac{E_{i-1} - E_i}{E_0} \qquad (2.3.3.7)$$

where

$$E_0 = E_\infty + \sum_{i=1}^{n} (E_{i-1} - E_i). \qquad (2.3.3.8)$$

The described alternative formulation of the storage and loss moduli, as described in 2.3.3.5 – 2.3.3.8, is specific for the applied Msc.Marc FE software. In this thesis a 15-term Maxwell model was fitted to the storage modulus (E´) vs. frequency master curve of the EPDM rubber containing 30 phr CB. The master curve and the parameters of the fitted Maxwell model will be introduced when treating the rolling friction (see chapter 7.3).

3.4 Chemical characterization of the elastomer surface

Surface characteristics of the EPDM elastomers were determined in their original state and after dry sliding tribotests with the goal to detect possible chemical changes in the elastomer structure. For this purpose three advanced characterization methods, viz. X-ray photoelectron spectroscopy (XPS), Raman spectroscopy and sessile drop test, were used.

3.4.1 XPS

The X-ray photoelectron spectroscopy (XPS) is a quantitative spectroscopic technique that measures the elemental composition within a material. This method is also called electron spectroscopy for chemical analysis (ESCA). This technique is based on the photoelectronic effect in which a material emits electrons under

electromagnetic irradiation, such as x-rays or visible light. In the XPS usually aluminum or magnesium X-rays are used to irradiate the investigated material and parallel the kinetic energy (KE) and number of emitted electrons will be measured. The emitted electrons can escape typically from the top layer (<10-12 nm) of the material, providing that way information related to the composition of the materials surface. XPS requires ultra-high vacuum (UHV) conditions [36]. The schematic sketch of the XPS test method is depicted in Figure 14.

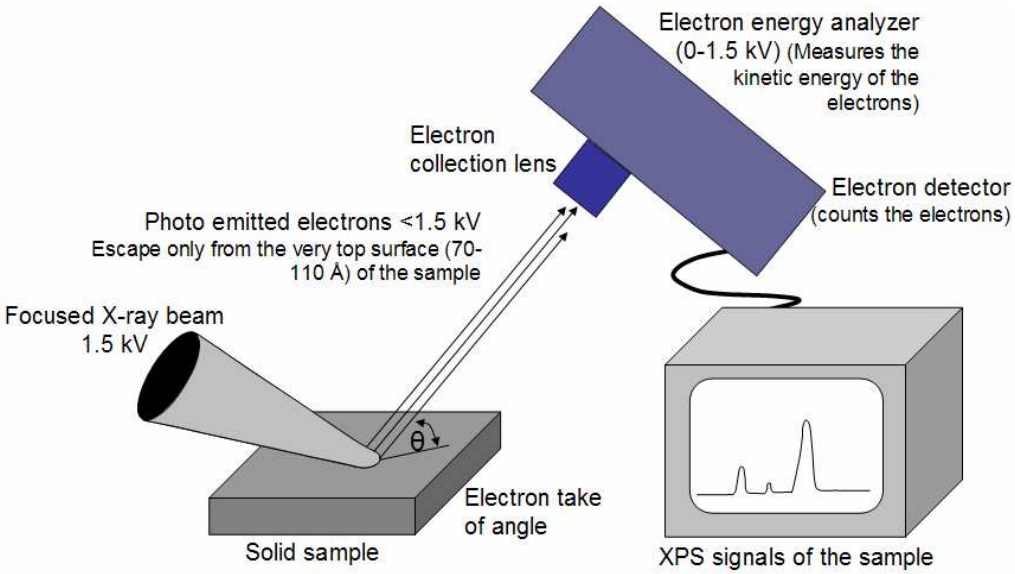

Figure 14: Schematic sketch of the XPS test method [36]

The kinetic or binding energy set of the emitted electrons is characteristic for each element. Because of it with the evaluation of the XPS signals (peaks) one can directly identify the elements on the surface of the investigated material. Note that the binding energy of the electron is that amount of energy which is needed to release the electron from its atomic orbital [37]. The number of detected electrons in each of the characteristic peaks correlates to the amount of element within the area irradiated.

A typical XPS spectrum is a plot of the number of electrons detected (Y-axis, ordinate) versus the kinetic energy of these electrons (X-axis, abscissa) [38]. Instead of the kinetic or binding energy, the wavelength of the electrons can be also used as measure of the X-axis.

The surface of the samples needs to be cleaned carefully; the contaminants and absorbed gases need to be removed from it applying special techniques.

3.4.2 Raman spectroscopy

The Raman spectroscopy is used in condensed matter physics and chemistry to study vibrational, rotational, and other low-frequency modes in a molecular system [39]. This test method is based on the phenomenon that a colliding molecule and photon pair interacts with each other. The result of such a collision can be the reflection, the absorption or the inelastic scattering of the photon. Raman spectroscopes use monochromatic light, usually laser in the visible, near infrared, or near ultraviolet range. The photons of the incident light (their common frequency is ω_0) are mainly absorbed or reflected by the molecules of the investigated material nevertheless the reflected light can be detected and analysed. It was found that the largest part of the reflected photons have the same wavelength (or frequency (ω_0)) as the incident light. This is the called Rayleigh scattering. On the other hand photons in small amount are detectable at other wavelengths. Due to the interaction with the vibrating molecule the energy (or frequency) of the laser photons can be shifted up or down ($\omega_0+\omega$, $\omega_0-\omega$, see Figure 15). This phenomenon is the so called Raman scattering.

As it is shown in Figure 15 the light from the illuminated spot is collected and sent through an analyzer to a detector [39]. The detected Raman shift will be analyzed using mathematical tools just like the Fourier method.

Because the Raman scattering behavior of chemical bonds and its different stretched or bended states is already known, the Raman spectroscopy can be used for the chemical structure and composition analysis of polymeric materials or for the determination of the polymer chain conformation in them [40].

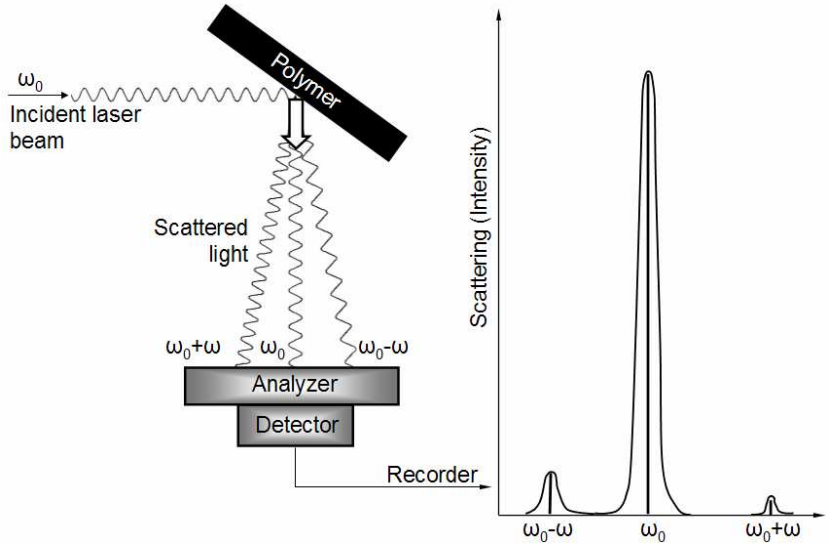

Figure 15 Schematic sketch of the Raman spectroscopy in front reflection mode [40]

3.4.3 Contact angle measurements

The contact angle is the angle at which a liquid interface meets the solid surface (see Figure 16). This angle is specific for any solid-liquid-ambient medium system. Most often this measurement will be realized suing a small liquid droplet resting on a flat horizontal solid surface. The arising shape of the droplet can be described with the help of the Young-Laplace equation [41]. The test rig to determine contact angle is called contact angle goniometer. Let us consider a drop of water on a solid surface (see Figure 16). In the case of strongly hydrophilic solid the water will be strongly attracted to the surface of the solid and the droplet will spread out having a contact angle close to 0°. In case of less strongly hydroph ilic solids the droplet will have a contact angle up to 90°. On highly hydrophobic surf aces the surfaces have water contact angles as high as 150° or even nearly 180° [42].

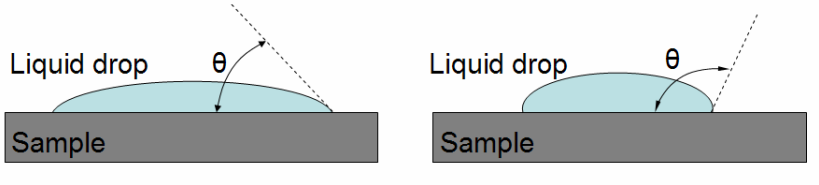

Figure 16: Schematic sketch of a water drop on a solid surface in case of hydrophilic (left) and hydrophobic material (right) [41]

The contact angle thus directly provides information on the interaction energy between the surface and the liquid. Using contact angle measurements one can detect structural or chemical changes on the tested samples [42].

3.5 Friction and wear of elastomeric materials

3.5.1 Theories related to the friction of elastomers

In the followings, the dry friction as well as rolling contact of elastomers is the subjects of discussion. There are many theories trying to describe the friction between different sliding pairs. The main difficulty is due to the complexity of interactions, being of chemical, mechanical and thermal nature between the surfaces of the contacting counterparts. Further problems are caused by the multiscale effects of the surface roughnesses. Note that the surface roughness varies from nano- to micro-scale in a very broad range.

Tribologists are creating theories to predict the friction and wear behaviors of different sliding pairs. For the simpler mathematical interpretation of a given problem some of the former mentioned phenomena are always neglected. The related assumptions depend on the actual topic of study. Due to this, the developed theories are valid only for special cases. Other retarding factor is, (however not from viewpoint of the tribology), the lack of universal material models, with which the elastic, viscoelastic, plastic, temperature-, stress- (or strain-) and velocity-dependent properties of the related materials could be considered.

The friction phenomenon is related with different mechanisms just like the adhesion, deformation on sliding asperities, viscoelastic losses, plastic yield, fracture and third-body mechanism. Next these phenomena will be detailed.

In Figure 17 the adhesion phenomena of a sliding (or rolling) cylinder on elastomeric plane under dry conditions is depicted. The κ distance between the rigid body and the elastomeric plane represents the molecular roughness of the elastomer. One can assume, that the polymer chains are fixed in the bulk at their one end (cross-linking) and free at the other. During sliding the free molecule ends touch the surface of the rigid body and adhere to it. The detaching process needs more energy then the adhering process and the molecules at the detaching (peeling) site of the contact region will be extended causing additional friction forces [43].

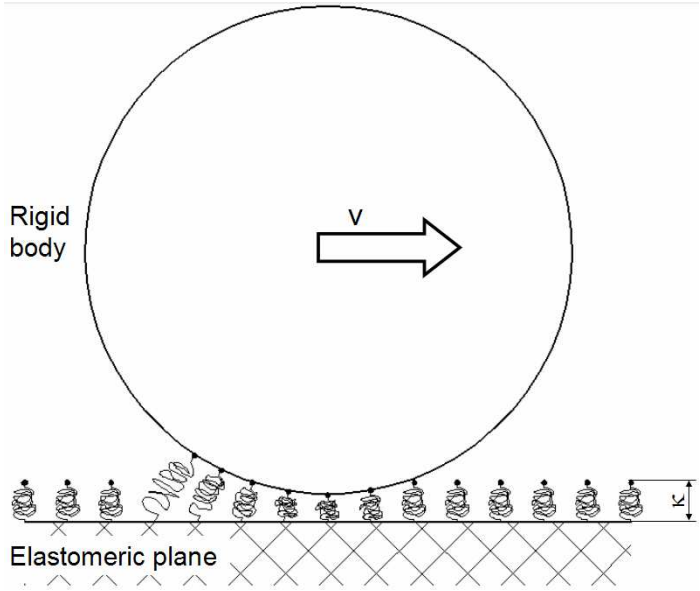

Figure 17: The adhesion effect in case of a rolling cylinder on elastomeric plane [44]

Based on the adhesion phenomena the same process causes friction even if the rigid body in Figure 17 is a large rolling cylinder, or if it is a sliding surface asperity in micron- or in nano-range [44]. Numerous workers showed that the dry sliding friction

depends on the normal force, on the sliding velocity and on the temperature (see [43, 44, 45, 46, 47] and references therein). General observation is that the friction coefficient increases with increasing normal load. This can be explained in a simple way. The friction force is caused by single adhering molecule chains. When more chains adhere to the rigid surface, larger friction force arises. Assuming a uniform free molecule end density on the rubber surface, the size of the real contact area is proportional with the magnitude of the arising friction force. So, with increasing normal load the real contact area increases (see Figure 18) which results in an increased friction force.

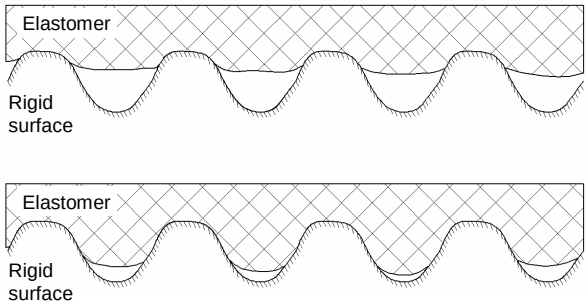

Figure 18: Increase of the contact surface due to increasing normal load.

More complicated task is to elucidate effects of the sliding speed and temperature. The dependence of the coefficient of friction as a function of the sliding speed is qualitatively depicted in Figure 19. The tendency of the curve in Figure 19 is similar to the loss modulus vs. temperature or loss modulus vs. frequency master curves [47]. This fact suggests that a very similar tendency should hold for the coefficient of friction (COF) vs. temperature curve keeping in mind the WLF time-temperature equivalence principle.

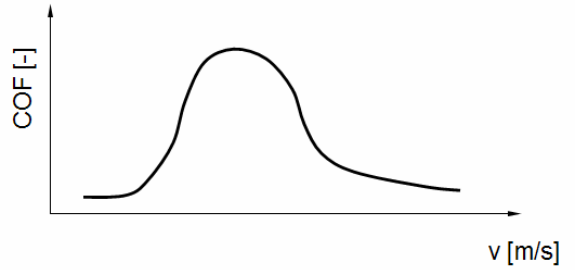

Figure 19: Qualitative depiction of the COF vs. velocity curve for dry sliding [47]

The reason of the similarity of the loss factor vs. frequency master curve and the COF vs. velocity curves can be explained as follows. During dry sliding the free molecule ends of the elastomer undergoe a steadily repeating touching-streching-detouching-touching cycle as it is shown in Figure 20 [45]. This repeating cycle can be considered as a harmonic excitation, so a similar behavior of the elastomer

molecules can be expected as that of the bulk material during DMTA tests. The quantitative description and the derivation of this approach can be found detailed in [46].

Figure 20: Classical description of a polymer chain in contact with a lateral counter surface. The chain stretches, detaches, relaxes, and reattaches to the surface in a cycle.

Another description of the rubber friction is based on the viscoelasticity of the elastomers, whereby the rubber friction is related to different phenomena. First, the sliding friction of elastomers in micro range is influenced by mechanical losses caused by interactions between the rubber and roughness peaks of the rigid surface. Second, the rolling friction of elastomeric rollers, as well as the rolling friction on an elastomeric plane can be quantitatively determined by the same principle in macro range. The common feature of these two approaches is that the friction can be deduced from the absorbed mechanical energy caused by the local deformations of the elastomeric material. The difference between them is in the determination of the accommodating deformations (stresses) caused by the roughness asperities (in the case of dry sliding) and by the rolling contact respectively. That is the reason why one need the viscoelastic characterization of the elastomeric material. In Figure 21 one can see the deformed zones of the elastomeric body during dry sliding caused by the asperities of the hard substrate [47, 48]. The deformations are calculated usually using the Hertzian contact theory assuming spherical shaped roughness peeks [47, 48, 49, 50, 51].

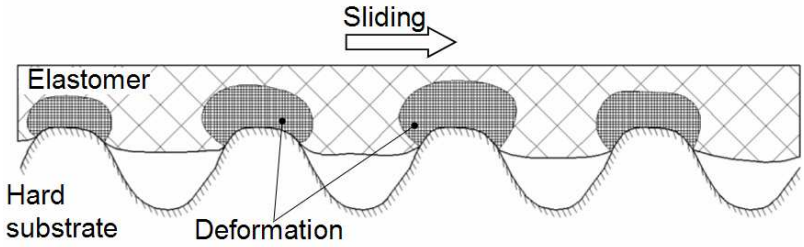

Figure 21: Deformations during dry sliding caused by the roughness peaks of the hard substrate

An interesting question is; how can be described the multiscale waviness of the rough surfaces. For this the so called power spectrum density is used, which

qualifies the surface roughness by describing the average values of the amplitude and wavelengths from mm range to the nanometer scale [49]. This kind of depiction of the surface roughness is shown in Figure 22.

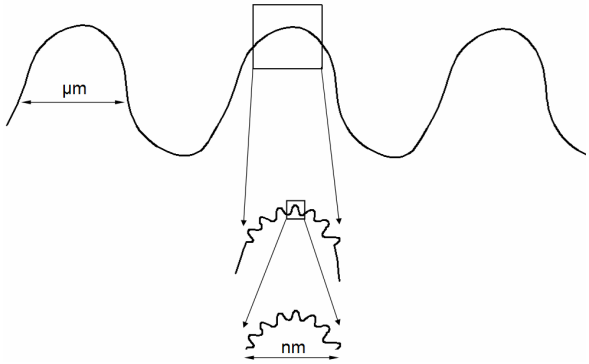

Figure 22: Surface roughness from micro- to nanometer range

The superposition of deformations in different scales, and that way, the arising mechanical losses due to the viscoelastic damping result in a friction force, which can be assessed experimentally in dry sliding measurements. However for correct results the effect of the adhesion should be also considered [50, 51].

As mentioned before, the rolling friction induced viscoelastic effects in elastomeric materials can be determined similarly as for sliding. On the other hand, the deformations in the related works [52 , 53, 54 , 55, 56, 57, 58, 59] were determined using the Hertzian contact theory in case of simple geometries. This is a simpler way as for dry sliding, but other phenomena such as, microslip [60], change in the contact area [61] or temperature increase [62, 63, 64, 65] due to the internal damping during rolling represent an additional challenge. Albeit not all the cited publications deals with elastomeric materials (but with other polymers), the used models and methods are applicable also for rubbers. Nowadays the FE method offers itself as a powerful tool to consider viscoelastic effects. Thus its use allows us to perform realistic calculations [66, 67].

Most of the approaches adopted for elastomers target to describe the friction during dry sliding or rolling. On the other hand, a further effect can play a key role in the friction and wear phenomena during dry sliding or rolling, namely the crack propagation [68] (see Figure 23). The friction increasing effect of the crack propagation during sliding is traceable by different rubbers [68].

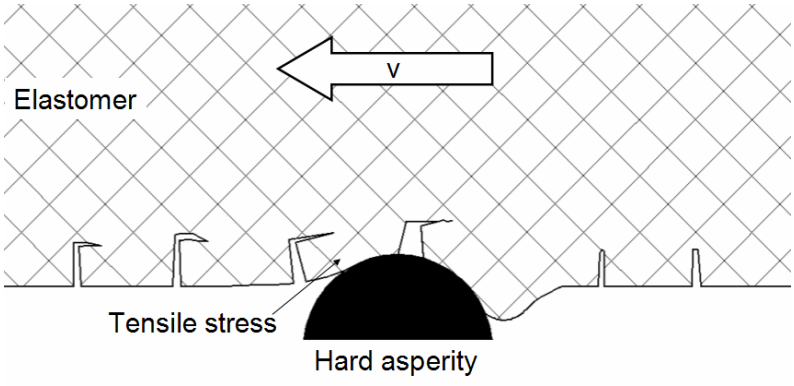

Figure 23: Rubber sliding over a substrate asperity. The tensile stress on the exit side leads to the formation of cracks in a thin layer at the rubber surface [68]

Elastomers are classified as nearly perfect elastic materials without irreversible deformations. Plastic deformations of the rubber (caused by the asperities) are usually not involved in the related theories. In contrast to this general opinion, our observations show, that the CB filled EPDM is able to undergo irreversible deformations (see Chapter 7.1). Moreover the test results pointed out that plastic deformation can play a dominant role during dry sliding. The effect of the plastic deformations may be so dominant that the whole sliding scenario (COF, wear mechanism …) will be changed (see Chapters 7.5, 7.6 and 7.7).

3.5.2 Wear of elastomers

3.5.2.1 Test methods

The wear behavior of rubbers is investigated since more than hundred years. First the rubbing behavior (roll formation, see Figure 24) of the unvulcanized rubber was observed and since then it was applied as eraser. Later, as the rubber becomes inevitable component in tires for different vehicles, the abrasive wear performance of different vulcanizates was under spot of interest. With further development of the rubber technology elastomers acquired in more and more technical applications, where the friction and wear are of great practical relevance. In résumé studies of rubbers tribology the following wear types are distinguished; abrasive, erosive, adhesive and fatigue wear [69, 70]. However, as the wear types are not always easy to separate from each other, basically the following statements are widely accepted.
If two sliding pairs are not separated by a lubricant, (the surfaces have direct contact with each other) and the counterpart is harder and rougher than the basic material,

abrasion or abrasive wear take place. Also hard particles which can get in between the interacting surfaces, for example even with the lubricant, lead to abrasive wear [71, 72].

Erosive wear or erosion is defined as the wear resulting from the interaction between a solid surface and a fluid stream containing abrasive particles with a certain speed. This definition includes also the impact of free-moving liquid (or solid) particles on a solid surface [69].

When an elastomer slides on smooth counterfaces along with a relatively large COF, adhesive wear occurs [69].

Fatigue wear occurs when the rubber surface endures repetitive stresses for a long time. Such exposures take place during rolling, or repeated bending (e.g. in case of conveyor belts).

Car tire is that rubber good which is produced in the largest quantities. As abrasive wear controls the performance of car tires, this is the most widely studied wear phenomenon. To compare the abrasion resistance of different rubber mixtures, without field trials, several standard laboratory abrasive test methods were developed just like the Taber Test [73] (see Figure 24 -1). The simplified laboratory test methods provide only comparative test results on the investigated rubber goods (see pictures 1, 2, 5 and 6 in Figure 24). To observe and analyze the wear mechanisms under abrasive conditions specific methods were developed. In the corresponding tests a razor blade or a needle is abrading the rubber surface, simulating a single roughness asperity of the abrasive surface (see pictures 4 and 5 in Figure 24). Detailed description of the latter test methods is to find in references [74, 75, 76 and 77] (blade on rubber plate test or blade abrader), and in references [69, 78 and 79] (scratch or needle on rubber plate test).

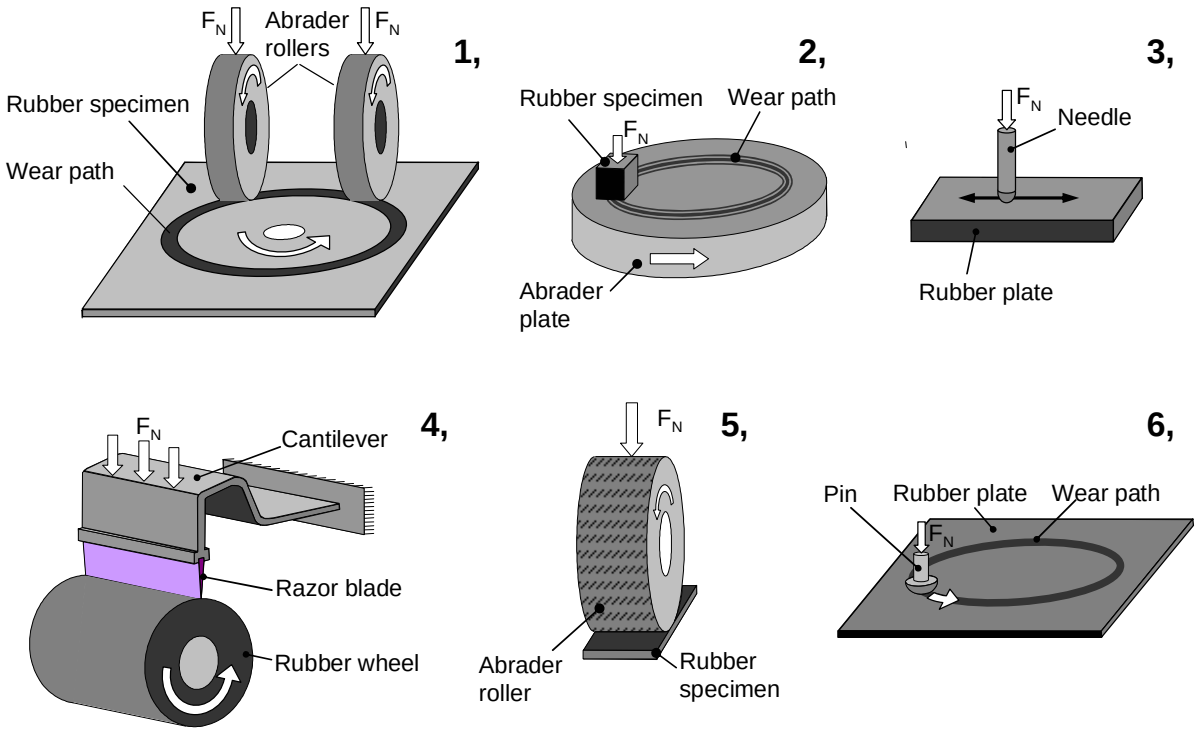

Figure 24: Schematic sketches of abrasive tribotest

Fatigue wear arise under repeated load cycles. This type of wear (or failure) takes place in vibration insulator elements, in seals working at high frequencies, in sliding elements suffering stick slip phenomena, or in elastomer parts exposed to rolling movement. This type of wear is usually tested in fretting conditions using a suitable machine (see picture 1 in Figure 25). There the tested material and the counter body are compressed together with a constant load and the counterpart is moving with relative small amplitude however at a high frequency on the specimen surface. The counterpart may be cylinder, sphere, etc… To test fatigue type failure under rolling, machines (two-disk configuration) are built in which the disks are pressed und rolled against each other (see picture 3 in Figure 25). Other possibility to test rolling-induced fatigue behavior is the rolling ball on plate setup, where a steel ball is pressed against a rubber plate and rolled in circular path or reciprocating along a line (see picture 2 and 4 in Figure 25). Attention should be paid to the fact that during dry rolling significant microslip (sliding of the non-adhering counter surfaces) can take place due to differences in the elastic moduli of the rolling pairs. Dry rolling is always accompanied with sliding wear. When the surfaces are lubricated, this microslip phenomenon can be neglected.

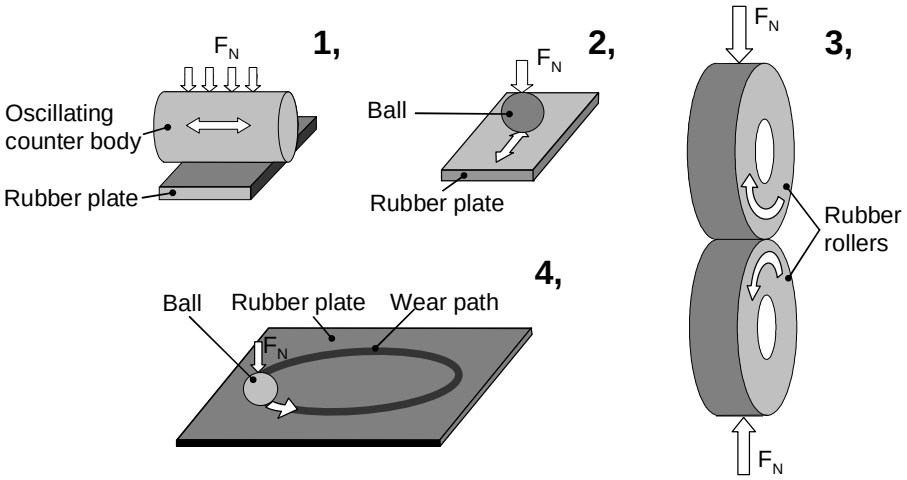

Figure 25: Schematic sketches of fatigue-type tribotest. 1- Fretting tribometer 2- reciprocating rolling ball on plate, 3- two disk machine 4- orbital rolling ball on plate [84]

In hydraulic or pneumatic systems, where the medium contains abrasive particles, erosion takes place. This type of wear mechanism was also intensively investigated to make durable life pipes, ventils, seals and hydraulic (pneumatic) systems. Mostly home made devices were built and as abrasive particles and their transporting media different systems were tried to model special industrial problems [80, 81]. A schematic picture of an erosive wear testing device is given in picture 1 in Figure 26. It is noteworthy, that the incidence angle (γ), the type and velocity of the particles and the type of the medium all have great importance related to the test results.

Sliding wear gained importance nowadays, because the lubrication between sliding rubber and other elements is dismissed based on economical and environmental reasons. On the other hand, new rubber formulations, coatings and elastomer-polymer sliding pairs have to satisfy the industrial needs. Very popular sliding wear test is the ball on prism test, as in the related device more specimens can be tested simultaneously. Disadvantage of this technique is that no friction force can be detected. In the ball on prism test a steel ball is pressed against two rubber plates forming a prism, and the ball is revolving around its axes (see picture 2 in Figure 26). Other possibility is the roller on plate (ROP), or shaft on plate test, where a rotating shaft is pressed against a rubber plate, while the normal and friction forces are detected (see picture 3 in Figure 26). Generally it is not always easy to distinguish between the different test methods which are differently classified. The

simplified laboratory abrasive tests (see pictures 2, 5 and 6 in Figure 24) can be labeled also as adhesive type sliding tests if the surface of the abrader counter body is smooth enough. There is no conventional definition on how to differentiate between abrasive-like and “smooth” surfaces.

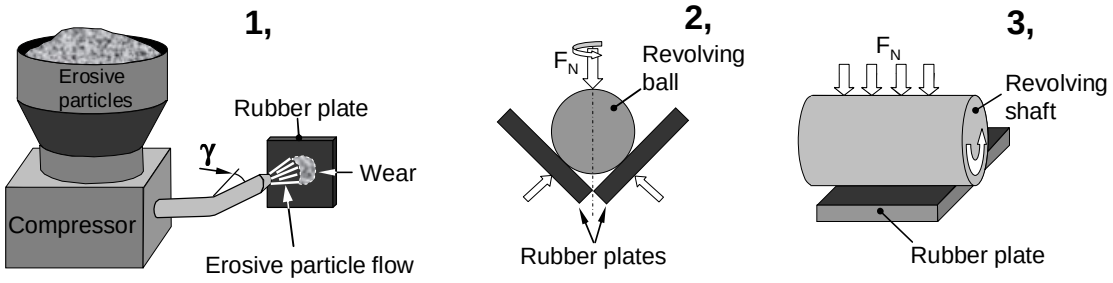

Figure 26: Schematic sketches of erosive-type and sliding tribotest 1- erosive sand blowing, 2- ball on prism [82, 83], 3- roller on plate ROP (or shaft on plate) [84]

3.5.2.2 Wear mechanisms

Other aspect for the classification of the wear of elastomers is based on the observation and description of their worn surfaces. This classification provides not always univocal results because usually more effects, acting parallel, influencing the wear process.

Generally the abrasion is a very harsh action which produces a rough surface. The heavy surface destruction caused is so difficult that its schematic interpretation is not possible. A typical unidirectionally abraded surface structure is depicted in Figure 27–a where abrasive grooves parcel the surface and wear particles are present. This kind of wear can be “produced” using the laboratory abrasion test rigs shown in pictures 2 and 5 in Figure 24. Because in Taber abrader the sliding is not unidirectional, the worn surface is not structured like in Figure 27–a. More clear is the abrasion wear track (see. Figure 27–b) when specific abrasion tests are used (razor blade or needle on plate in pictures 3 and 4 in Figure 24) [77, 85, 86, 87, 88]. With these tests one can mimic and investigate the effect of one single abrader roughness peak or of a sharp edge. The dimensions of the rubber tongues, angles of the crack propagation, crack density, etc… have to be determined and different mechanical models can be created to explain the abrasion properties of the investigated rubbers.

During fatigue-like tests, if the surfaces are lubricated, peculiar subsurface crack initiation and propagation may take place. It is known, in Hertzian like contacts the maximum stresses and strains appear in the bulk near to the surface. So the probability of crack initiation is the highest there, where the arising strains reach their

maximum. Thus cracks arise below the surface and the cracks propagate during the fatigue process. This crack propagation advances as long the cracks grow together and wear particles break out of the surface (and material removal happens) (see Figure 28-a). This phenomenon is called pitting or gouging. In Figure 28-a one can see the schematic picture of the gouging effect, the onset of which can be observed in fretting or in rolling tests. Under dry rolling conditions additional sliding wear occurs via microslip. This will be discussed later.

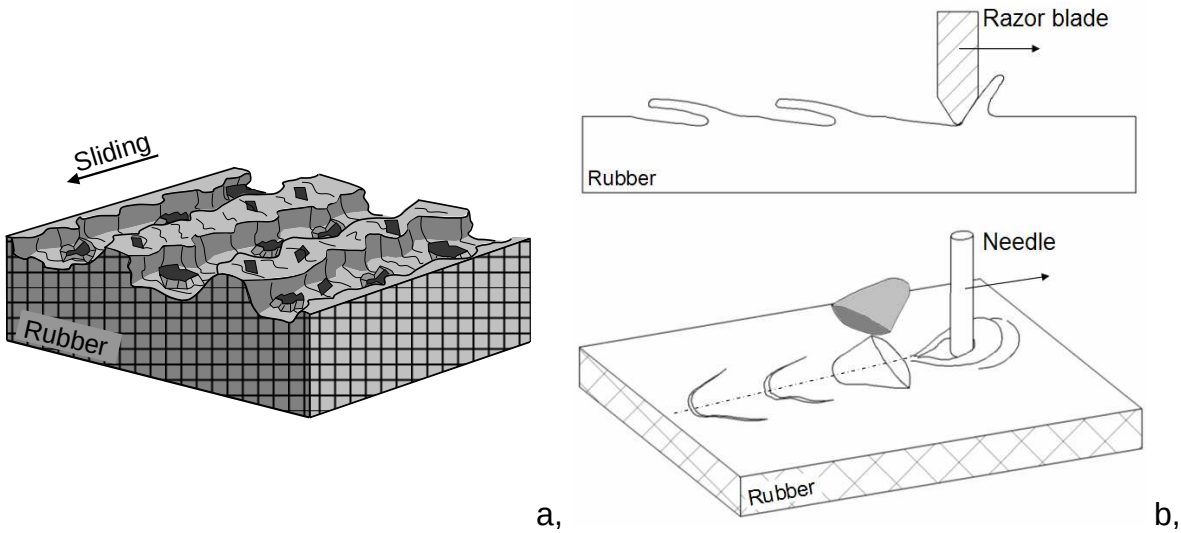

Figure 27: Surface damages after abrasive tribotests. a- general abrasion test, b- Razor blade and needle on plate test results.

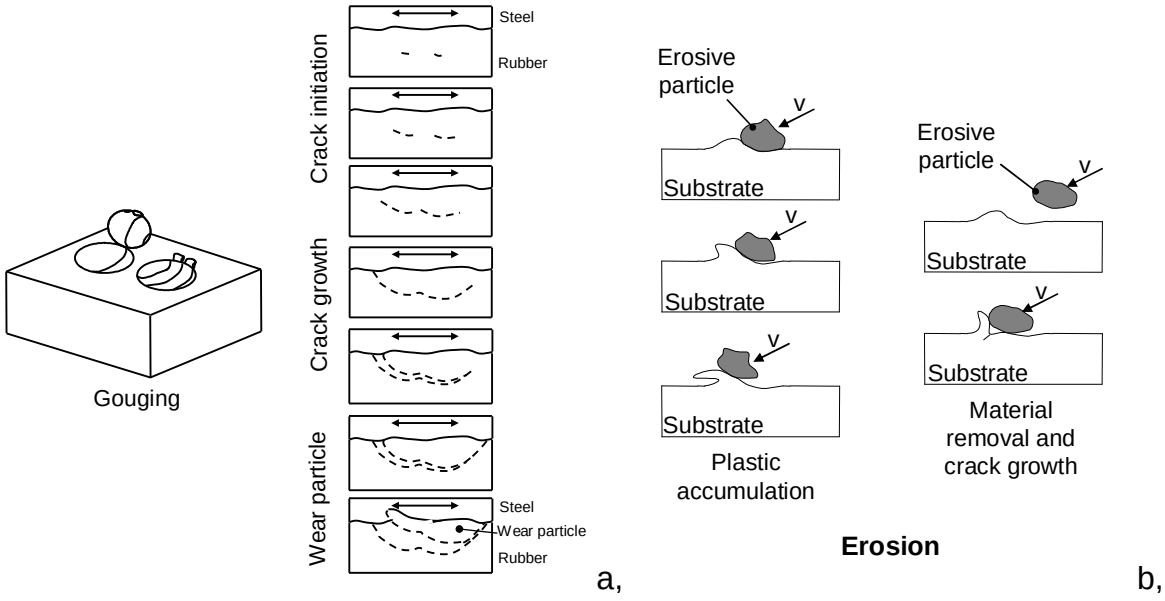

Figure 28: Wear mechanisms in case of fatigue [89] (a) and erosive [69] (b) tribotests

Erosion is occurred by steady collisions between the erosive particles and the substrate. According to the properties of the related substrate, these collisions may

have different consequences. If the material is tough, a permanently growing plastic deformation occurs which leads to wear. When the substrate is rigid (brittle) cracks appear due to the collisions at the surface. They grow into the bulk whereby small particles can be removed from the substrate as it is shown in Figure 28-b. An example for the tribotest rig involved is to see in picture 1 in Figure 26.

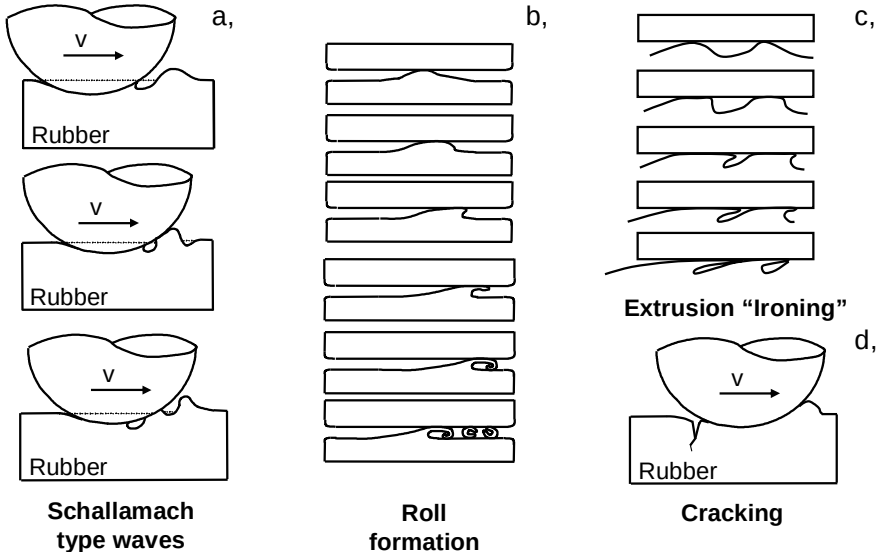

Figure 29: Wear mechanisms caused by dry sliding (adhesive wear)

The adhesion type wear mechanism can be very different depending on the movement type. The most known and investigated phenomenon is the so called Schallamach type waviness [90]. This arises when a macroscaled counterbody slides on a flat elastomer plate while the COF is large. The Schallamach waves reflect instabilities in the contact area. Stick and slip zones appear and the rigid counter body leaves a wavy pattern behind (see Figure 29-a). A smooth and flat counterbody during sliding can cause large tensile strains on the rubber surface due to the large adhesion forces. It can lead to roll formation (see Figure 29-b) or to extrusion (“ironing”) (see Figure 29-c). Though here the roll formation process is related to adhesion-type wear, other authors trace it to abrasion phenomena, see reference [91]. Because large tensile stress appears during dry sliding, this often causes cracking path behind the counterbody in the tensile zone (see Figure 29-d). Of course the consequence of these phenomena is material loss, i.e. wear in every case.

The most typical wear picture of rubbery materials during dry sliding is a characteristic waviness, wavy pattern. This is initiated by Schallamach-type waves (see Figure 29-a). In Figure 30-a one can see an assumed process caused by

repeated sliding of a rigid body over an already cracked highly filled EPDM rubber in pin on plate (POP) test configuration. During sliding large deformation takes place, partly plastically, and the cracks become deeper. In Figure 30-b it is depicted how extreme plastic deformation can be accumulated at these cracks. Finally, the rubber tongues take their final shape and the overview of the wear track shows a wavy surface, the so called “combing waviness” (see Figure 30-c).

The overall mechanical properties of the unfilled elastomers are usually weaker than those of filled ones. A consequence of the weak mechanical properties is well reflected also during dry sliding wear. In Figure 31 one can see the wear mechanism during dry POP test of an unfilled EPDM elastomer. Although Schallamach waviness appears first, but later, instead of plastic deformation of the rubber at the cracks, fast crack propagation takes place (see Figure 31-a). As a consequence, no wavy wear track can be resolved after the tribotest. Instead of that a crater–like surface structure develops (see Figure 31-b).

These differences between the filled and unfilled elastomers are observable already in other sliding tribotests, as it will be shown later. Moreover, the fast cracking of the unfilled and the large deformability of the filled elastomers remain characteristic for all other sliding tests.

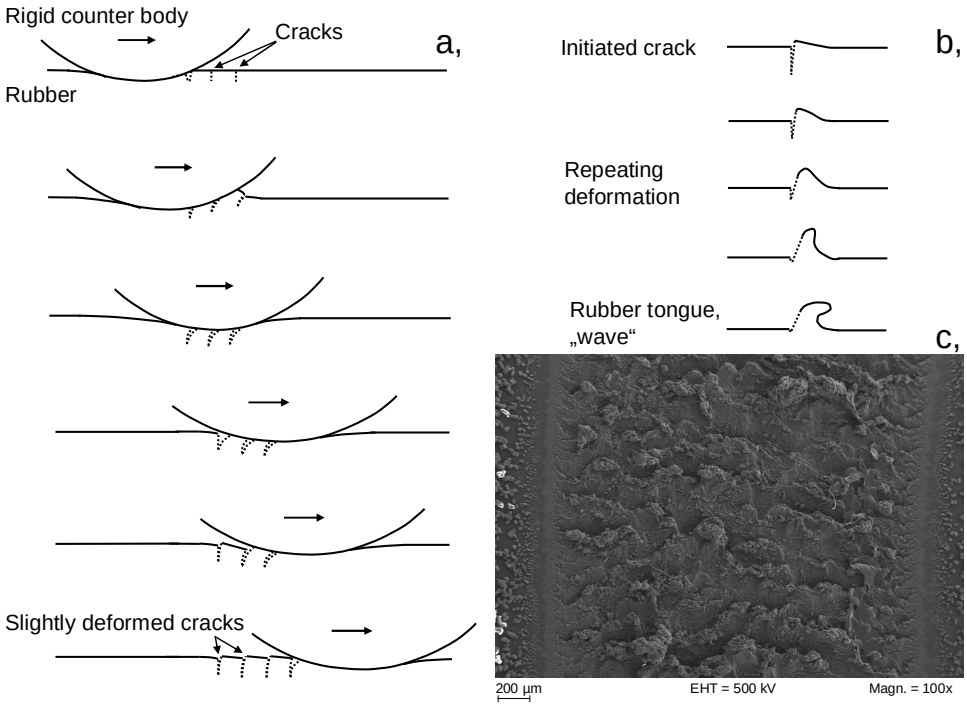

Figure 30: Typical wear mechanisms by dry sliding related to the Schallamach waviness. a -small residual deformations during over sliding, b -arising rubber tongues due to plastic deformation, c -combing waviness of an EPDM rubber containing 60 phr CB after POP test.

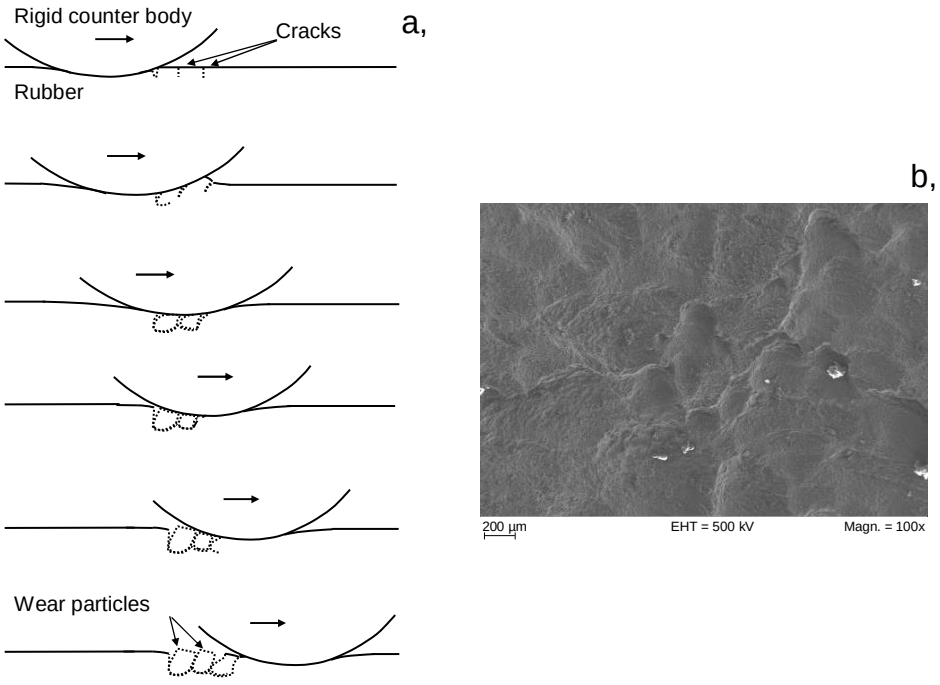

Figure 31: Typical wear mechanisms by dry sliding in case of weak, unfilled elastomers related to the Schallamach waviness. a –fast crack propagation and wear particle formation, b – crater-like surface of an unfilled EPDM rubber after POP test.

4 Objectives

The demand of the industry for high performance materials of improved wear resistance is steadily increasing. To meet the requirements, such as wear resistance, it is necessary to clarify what kinds of mechanisms are controlling the friction and wear during dry sliding. Other need from industry side is to predict the friction behavior and the wear performance of a given tribological system.

The aim of this work was to find correlation between the material and tribological properties of elastomeric materials in case of dry sliding. A further target was to investigate the effect of changing temperature and normal pressure onto the micromechanical processes during dry sliding. Our last objective was to explore the importance of viscoelasticity in the tribological processes of elastomers.

For this study a simple, easily modelable tribological test set up, the roller-on-plate (ROP) test rig was chosen (cf. Figure 26-3). With the ROP test rig dry sliding tests were carried out on a series of elastomeric materials. Subjects of the investigation were EPDM rubbers with different amounts of carbon black (CB) contents (0, 30, 45 and 60 phr).

The effect of the changing contact stress during the ROP tests will be detected by measuring the change in the COF and in the loss volume. The loss volume will be determined based on the contour of the evolved wear groove. The geometry of the wear groove will be assessed by white light profilometer. The change in the wear mechanisms will be followed by SEM investigations. We assume that due to the elevated contact temperature during dry sliding chemical changes may take place on the surface. To detect the chemical composition of the specimens X-ray photoelectron and Raman spectra of the surface will be recorded before and after the tribotests. Sessil drop tests are foreseen to show the change in the surface free energies after dry sliding.

A further tribotest, namely dry rolling, will be also carried out to study the viscoelastic effects of the EPDM 30 material. During the rolling tribotest the coefficient of friction will be detected.

The quasi static tensile and compressive, as well as the time (frequency) and temperature dependent mechanical properties of the EPDM materials will be determined. Based on the quasi static mechanical test results nonlinear two parameter Mooney-Rivlin material model will be created for the investigated

elastomers. From the results of the DMTA tests (frequency and temperature dependent properties) a master curve will be created using the WLF theory. This master curve will be fitted with a 15-term generalized Maxwell model. These material models, i.e. Mooney-Rivlin and generalized Maxwell, will be used by the FE simulation of the sliding and rolling tribotests.

The FE simulations will help us to understand the mechanical processes during the tribotests.

5 Materials

5.1 EPDM/CB mixes

The properties of rubbery materials can be tailored upon request using different additives, usually nano-sized filler materials [92, 93, 94]. The recipe of the rubber mixture is of great importance. It influences the mixing and the curing properties of the mixes, as well as the mechanical, chemical and thermal properties of the end products. The basic additives of the rubbers can be classified as plasticizers, activators, accelerators, curatives and fillers.

The investigated EPDM stocks were prepared in a laboratory internal mixer and the curatives were introduced on a laboratory open mill. The recipe used was as follows: EPDM (Keltan® 512 of DSM Elastomers, Sittard, The Netherlands): 100 parts; carbon black (N550): 0, 30, 45 and 60 parts; ZnO: 5 parts; N-cyclohexyl-2-benzothiazole sulfenamide (CBS, Vulkacit CZ of Bayer, Leverkusen, Germany): 0.6 part; 2-mercapto benzothiazole (MBT, Vulkacit Mercapto by Bayer): 0.6 part; zinc dibenzyl dithiocarbamate (Rhenogran ZBEC-70 of Rhein Chemie): 1.5 parts and zinc dicyanatodiamine (Rhenogran Geniplex 80 of Rhein Chemie, Mannheim, Germany): 0.6 part, sulphure, 1.5 part, stearic acid, 1 part.

ZnO (Zinc oxide) is a generally used activator in manufacturing of rubber mixes. A proper value of this additive allows a quicker and more controllable rubber cure. Zinc oxide may also serve as filler in some rubber mixtures [95].

Zinc dicyanatodiamine is a special accelerator material which together with the other accelerators and sulphur-donors (cf. Figure 32) creates a special accelerator system. This accelerator system allows an optimized and controlled rubber curing process [96, 97]. When sulphur donors are used to realize the crosslinking, typically monosulphide crosslinks will be created between the polymer molecules. This system is called effective vulcanizing (EV) system. In contrast to EV systems, in conventional vulcanization systems, where elemental sulphur is used for vulcanization, di- and polysulphide crosslinks will be produced. Conventionally cured vulcanizates are less stable at elevated temperatures, because sulphur may be released from the polysulphide crosslinks. This creates additional crosslinks, changing that way the material properties.

CB influences generally the material properties of the vulcanizate. The CB content was varied in order to study the effect of this filler on the mechanical, thermal

and wear properties of the EPDM rubbers. The CB content of the EPDM rubbers was varied between 0 and 60 parts per hundred parts rubber (phr). Based on the above recipe, 30, 45 and 60 phr CB corresponds to 21.3, 28.8 and 35.1 wt.-%, respectively.

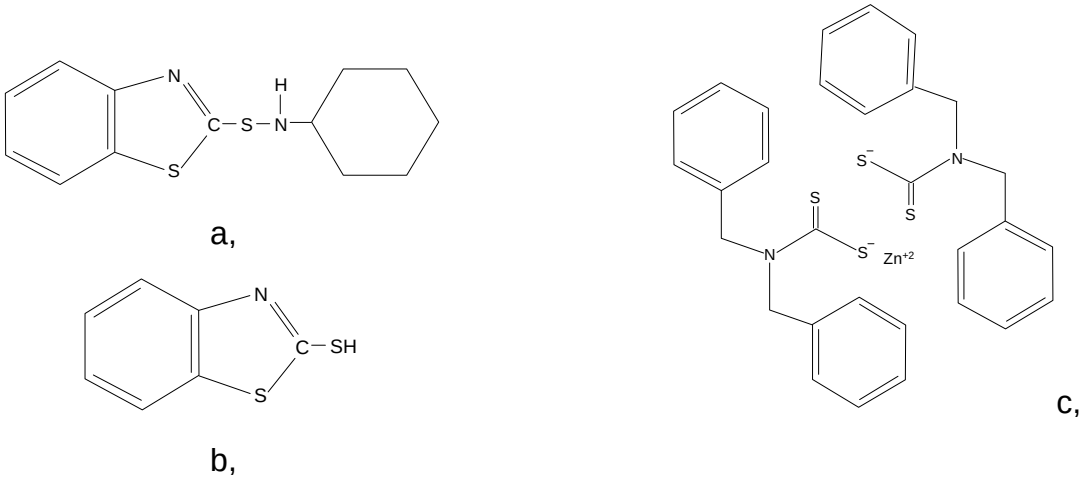

Figure 32: The accelerators and sulphur donors a; N-cyclohexyl-2-benzothiazole sulfonamide (CBS), b; 2-mercapto benzothiazole (MBT), c; zinc dibenzyl dithiocarbamate (ZBEC)

5.2 Carbon Black

Within this study N550 –type carbon black filled EPDM was investigated. The most important parameters of this N550 –type carbon black are listed in Table 1.

Table 1 Physical properties of the used carbon black [18]

ASTM number	D_w^d, nm	Mean Particle diameter, nm	DBPA $cm^3/100g$	Compressed DBPA $cm^3/100g$
N550	240	56	122	81

In Table 1 D_w^d is the mean value of the aggregate diameter distribution, determined using Stoke's law for a centrifugal sedimentation process. DBPA means the di(n-dibutyl) phthalate (DBP) absorption ability of the carbon black in normal circumstances (ASTM D 2414-90) and under compression (ASTM D 3493-90). This data informs us about the activity (surface area, porosity etc…) of the carbon black. The (surface) activity of the CB is an extremely important parameter, as it determines the reinforcing ability of the filler particles. The DBPA tests under compression give information about the stability of the CB aggregates. The applied carbon black particles create linear type aggregates with moderate complex junctions (cf. Figure 3).

5.3 Curing

Rubber sheets (ca. 2 and 4 mm thick) were produced by compression molding at 160 ℃ and 7 MPa pressure using a Satim press (R ion des Landes, France). The vulcanization time was adjusted by considering the time needed for the 90% crosslinking at T=160℃. The related time 7.3- 9.6 min (depending on the CB content) was read from the torque-time curves registered by a Monsanto moving die rheometer (MDR 2000 EA-1).

6 Experimental

6.1 Mechanical Characterization

6.1.1 Tensile Tests

Tensile tests were carried out on 2 mm thick dumbbells (type: S1 according to DIN 53504) on a Zwick 1489 (Ulm, Germany) universal testing machine applying a deformation rate of 500 mm/min at room temperature. The related material properties represent the mean values obtained from five or more parallel measurements. The stress-strain behavior is discussed in chapter 7.1.

6.1.2 Compression Tests

Compression tests were carried out on ~3x3x3 mm^3 cubic shaped specimens on a Zwick 1445 (Ulm, Germany) universal testing machine applying a deformation rate of 1 mm/min at room temperature. During compression tests the compressive steel plates were lubricated using adequate grease (E-COLL Helles Mehrzweckfett I., Wuppertal, Germany) to minimize the friction between the specimen and the steel plates. The tests were repeated for every material five times and the averaged stress-strain curve was considered and discussed.

6.2 Thermo-Mechanical Characterization

Dynamic-mechanical thermal analysis (DMTA) spectra were recorded on rectangular specimens (length x width x thickness = 20 x 10 x ca. 2 mm^3) in tensile mode as a function of temperature (from -100 °C to +100 °C) and frequency at 1, 10 and 100 Hz using a Q800 device of TA Instruments (New Castle, DE, USA). The conditions set were: strain 0.01%, temperature step: 5°C, time for temperature equilibration at each step: 3 s.

The used tension clamping of the DMTA tests is to see in Figure 33. The aim of the DMTA tests was to get information about the time (frequency) and temperature dependent material behavior and generate DMTA vs. frequency master curves. The latter are needed for the generalized Maxwell models. The results of the DMTA tests are detailed in chapter 7.2.

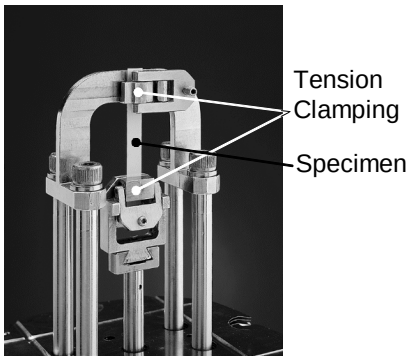

Figure 33: The tension clamping of the DMTA device

6.3 Micro-Structural Characterization

6.3.1 Scanning Electron Microscopy (SEM)

The worn surfaces of the specimens were inspected in a scanning electron microscope (SEM; JSM5400 of Jeol, Tokyo, Japan). Prior to SEM investigation the specimens were sputtered with an Au/Pd alloy using a device of Balzers (Lichtenstein).

6.3.2 White Light Profilometry (WLP)

The wear tracks of the tribotested specimens were scanned using a WLP machine (FRT Fries Research Technology, Bergisch Gladbach, Germany). The dimensions (width and depth) of the wear tracks were determined based of the WLP surface scans. The white light profilometry device (Figure 34) scanned the wear tracks resulting 3D coordinates of the surface points. That way a three dimensional picture was received and the average width (d_{w2}), depth ($d_{w1}/2$) and length (b_w) of the wear tracks could be determined (cf. Figure 34). Using these measured values, and assuming an elliptical cross section of the worn groove, the loss volume (V_{loss}) can be easily calculated, as it is shown in Figure 34.

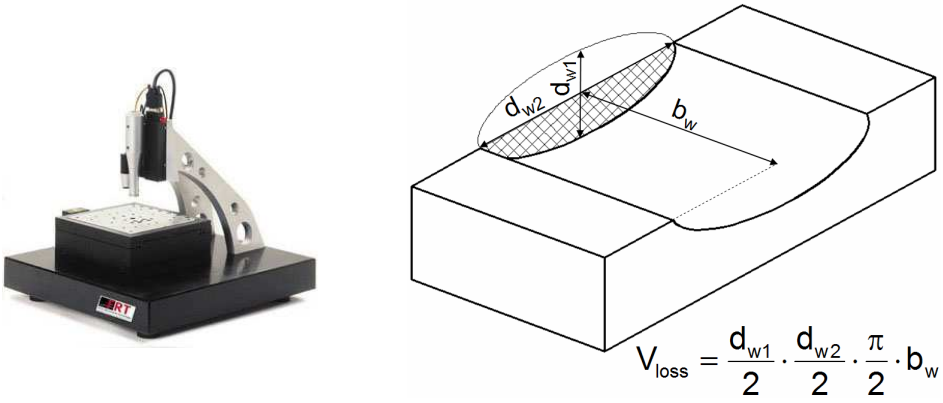

Figure 34: The white light profilometry device and calculation method of the V_{loss}

6.4 Chemical Surface Analysis

6.4.1 XPS

The XPS measurements were performed in an ultra high-vacuum (UHV) chamber with a base pressure of 1x10-10 mbar. The angle between the hemispherical analyzer (Specs-PHOIBOS100, SPECS Nanotechnology, Delft, Netherlands) and the plane of the surface was kept at 60° and the x-ray radiation was the Mg Ka line (1253.6 eV). The survey spectra were recorded with a photon energy step of 0.25 eV and pass energy of 40 eV and the C 1s core levels with a photon energy step of 0.1 eV and pass energy of 15 eV. Prior to the data analysis, the contributions of the MgKa satellite lines were subtracted and the spectra were subjected to linear background subtraction formalism. The binding energy (BE) scale was calibrated with respect to the C 1s peak at 285 eV. For the analysis of the C 1s peak, the full width at half maximum (FWHM) of the C–C/C–H component was left to vary freely and the other components were forced to adopt this value. In addition, a sputtering of the samples was also performed by etching with a beam of energetic Ar+ ions in order to remove the contamination of the surface.

6.4.2 Contact Angle measurements (CA)

Static CA measurements were carried out by the sessile drop method using water drops of 4 µl at room temperature. The surface energy evaluation system [98] was used for the acquisition of the drop images and its further analysis with a specific software.

6.4.3 Raman Spectroscopy

Raman spectroscopy was used for detecting the variation of the non-polar species like double bonds (C=C) present in the system after tribological tests. Raman spectra were collected using Raman scattering by 514.5 nm excitation of a diode laser and the spectra were recorded using a Renishaw Ramascope 2000 microspectrometer (Renishaw plc, Gloucestershire, UK) with a laser power of 10 mW.

6.5 Tribotests

6.5.1 Dry Sliding Tests

To study the sliding wear a roller-on-plate testing machine was used (SOP 3000 tribotester, Dr Tillwich GmbH, Horb-Ahldorf, Germany), referred further on ROP. During the tests a rotating steel roller is pressed against a rubber strip of ~8.3 mm width and rotated around its axes. The roller was made of 9SMnPb28k type steel according to the DIN 7 norm, (diameter: 10 mm, width: 20 mm and $R_a \approx 0.9$ µm). The normal load and the frictional force induced by the torque were measured online and thus the COF was registered during the test. The schematic sketch and the photograph of the tribotesting device is to see on Figure 35.

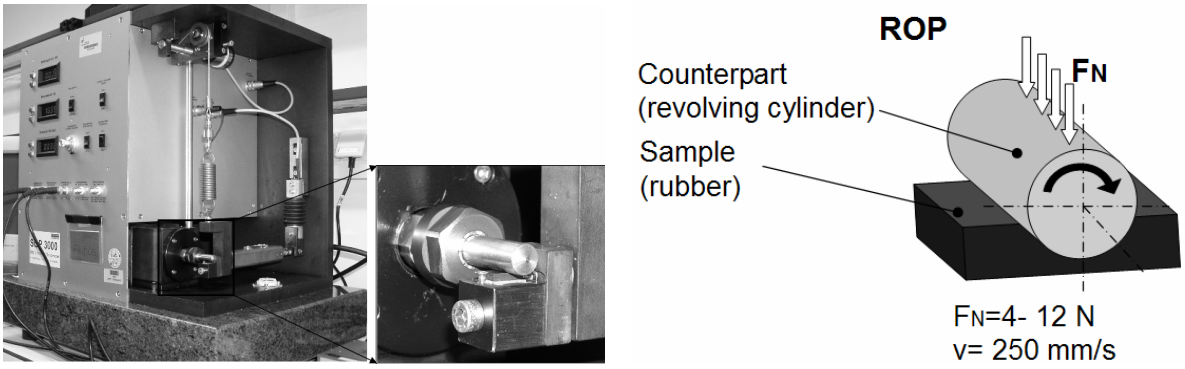

Figure 35 Picture and the schematic sketch of the Roller on Plate (ROP) tribotesting device

Table 2: Summary of the tribotesting parameters used

Materials / Test parameters	Sliding speed 250 [mm/sec]							
	F_N [N]	Sliding time [min]						
EPDM with 0-, 30-, 45- and 60 phr CB content	4	1	2	5	10	20	45	90
	6							
	8							
	10							
	12							

The test parameters are summarized in Table 2. ROP tests were carried out at different normal loads (4 – 12 N) and the sliding time (or sliding way) was varied between 1 and 90 min. This relatively broad normal load range was chosen with respect to the sensitivity of the test rig as well as to produce mild and severe wear in the specimens. Every measurement was repeated five times, and the average values were determined. As a result of this test series a detailed review become available

on the wear and friction behavior of the EPDM material as a function of the carbon black (CB) content, normal load and sliding distance (time).

The mass of the specimens was measured before and after testing using a microbalance (Mettler AT261, Giessen, Germany). By this way the mass loss owing to wear was detected gravimetrically. Because of the uncertainty of the gravimetrically determined mass losses, the loss volume was calculated based on the WLP scan data. The loss volumes were determined at every tested parameter (Table 2) based on WLP measurements (see chapter 6.3.2). Large scatter in the related wear data was caused by sliding instabilities (vibrations). Nevertheless clear tendencies were to observe in respect to the wear results (V_{loss}).

6.5.2 Rolling friction tests

Rolling friction tests were carried out on a home built test rig with oscillating rolling ball (100Cr6, d=2r=14 mm, R_a=1 µm) and stationary rubber plate (cf. Figure 36). The steel ball is driven by the driver part to conduct oscillating rolling motion on the rubber plate. The load is applied by a lever system. The reciprocating linear rolling of the ball occurred with an amplitude of A=25.06 mm, a cyclic frequency of f=1/30 Hz under a normal load of 140 N. This normal load was chosen to produce well detectable friction force. The normal and friction load are measured by load cells. The load cell which measures the normal load (Load cell 1, cf. Figure 36) is placed under the base plate, while the other load cell which measures the friction force (Load cell 2) is placed at the driver element. The ball is rolling in the guiding edges of the driver part (cf. Figure 36-c).

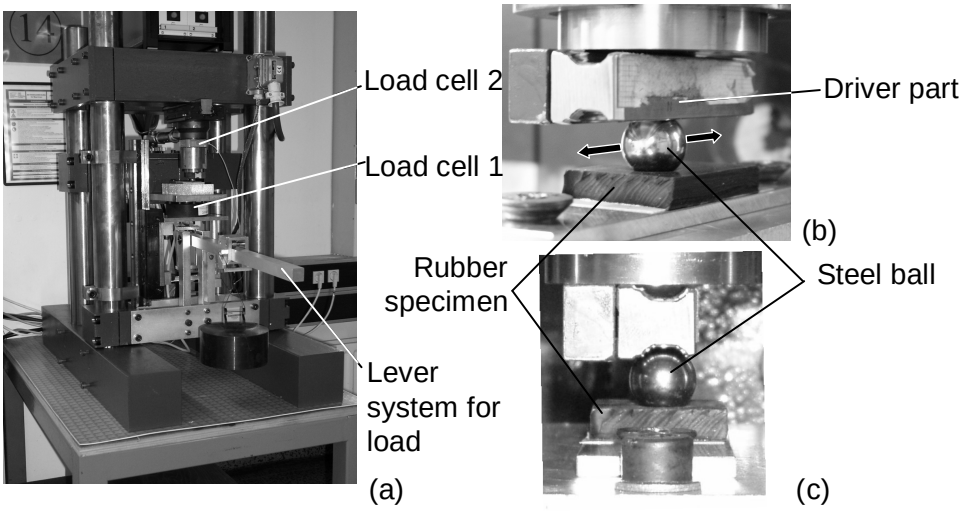

Figure 36: Overview of the Oscillating-RBOP machine (a), detailed view of steel ball rolling on a flat rubber specimen (b), front view of the set-up (c)

6.6 Test conditions of the rolling friction test

The linear reciprocating movement of the driver part and the reciprocating rolling of the ball have different amplitudes and speeds due to the set-up. As starting point of our calculations we used the known movement of the driver part, which reciprocated with a given amplitude and frequency. The kinematical and contact geometry of the ball is shown in Figure 37. One could see the initial and the end position of the ball and the direction of the oscillation shown by arrows. Figure 37 also shows the change of the ball's displacement and the change of the curve of rolling velocity versus the time, where "T_p" is the period (30 sec). On the right side of Figure 36 one can see the contact geometry, where "r" is the radius of the rolling steel ball (7 mm), "g" is the width of the guiding groove on the driver part (8.6 mm), "h" is the vertical distance from the centre point to the upper contact point of the ball, calculated by equations (5.5.1) and (5.5.2).

$$h = r \cdot \cos\alpha\,, \tag{5.5.1}$$

wheret

$$\alpha = \arcsin\frac{g}{2 \cdot r}\,. \tag{5.5.2}$$

We assumed the pure rolling of the ball without any slip at the contact both with the driver part and with the rubber specimen. With this assumption the position and the velocity of the driver part could be calculated using the equations (5.5.3) and (5.5.4).

$$s_D(t) = -A \cdot \cos\left(\frac{2\pi}{T_p} \cdot t\right), \tag{5.5.3}$$

$$v_D(t) = \frac{2\pi}{T} \cdot A \cdot \sin\left(\frac{2\pi}{T_p} \cdot t\right). \tag{5.5.4}$$

The ratio of the driver part's displacement and the velocity to the rolling ball's is constant. The displacement (s(t)) and the velocity (v(t)) of the rolling ball is smaller than that of the driver part. This ratio is given by the equation (5.5.5)

$$\frac{s(t)}{s_D(t)} = \frac{v(t)}{v_D(t)} = \frac{r}{r+h}\,. \tag{5.5.5}$$

Using equations (5.5.3), (5.5.4) and (5.5.5), the displacement and the speed of the rolling ball can be described as follows:

$$s(t) = -A \cdot \left(\frac{r}{r+h} \right) \cdot \cos\left(\frac{2\pi}{T_p} \cdot t \right), \qquad (5.5.6)$$

$$v(t) = \frac{2\pi}{T} \cdot A \cdot \left(\frac{r}{r+h} \right) \cdot \sin\left(\frac{2\pi}{T_p} \cdot t \right). \qquad (5.5.7)$$

The maximum of the displacement ($s(t)_{max}$) of the rolling ball means the amplitude of the reciprocating motion (A=25.06 mm). This will be reached at t=0, $t=T_p/2$ and $t=T_p$. The maximum of the rolling velocity is reached at $t=T_p/4$ and $t=3T_p/4$ (cf. Figure 37). Substituting the data into equations (5.5.6) and (5.5.7), the displacement and the velocity of the rolling ball can be described as follows:

$$s(t) = -0.007019 \cdot \cos\left(\frac{2\pi}{T_p} \cdot t \right) [m] \qquad (5.5.8)$$

$$v(t) = 0.00147 \cdot \sin\left(\frac{2\pi}{T_p} \cdot t \right) \left[\frac{m}{s} \right]. \qquad (5.5.9)$$

If we fixed the centre point of the coordinate system at the middle point of the ball, the apparent angular velocity of the ball ($\omega(t)$) could be calculated as follows:

$$\omega(t) = \frac{v(t)}{r}. \qquad (5.5.10)$$

This value will be needed later by the description of the boundary conditions of the FE simulation.

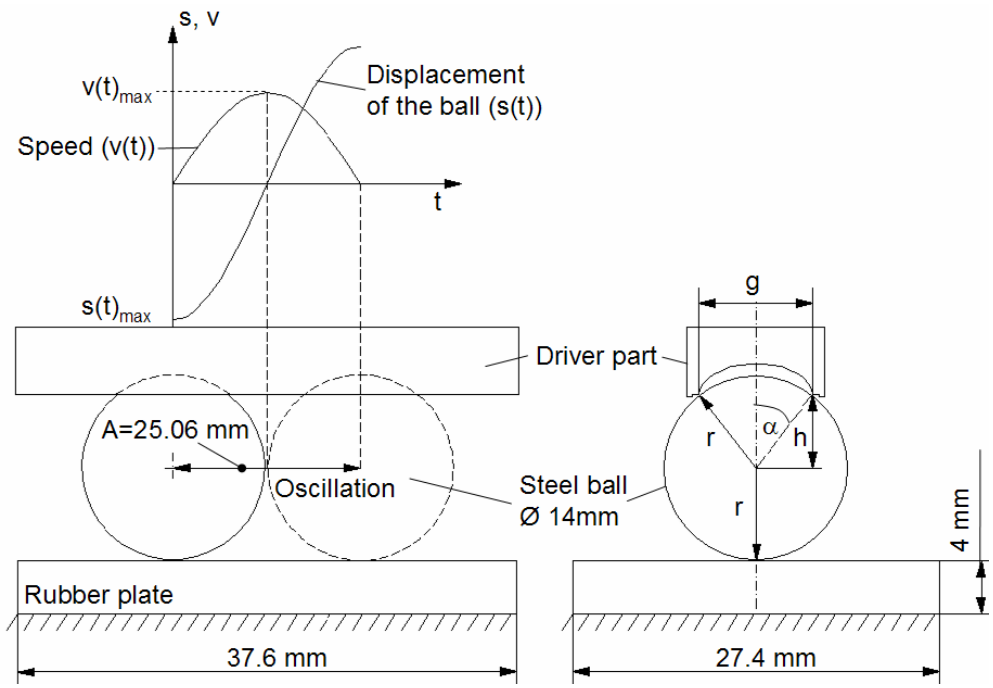

Figure 37: Schematic sketches of the contact geometry and of the ball's kinematics in a half cycle

6.7 Temperature measurements during dry sliding tests

During the measurements, the heat development was detected using an infrared thermo camera (VarioCAM, Jenoptik, Jena, Germany). Thermo cameras are able to detect the electromagnetic radiation in the infrared spectrum and display it in a color coded heat map. All objects emit infrared radiation based on their temperature. According to the ideal black body radiation law, the temperature of the observed objects can be determined. The camera was placed at the side of the specimen, and micro lens was adopted to focus the camera on the small sized specimen (cf. Figure 38). The measured temperature values were registered in a time interval of 15 s. The highest temperatures were detected at the end of the rotating steel roller near to the contact surface; these values were considered as contact temperatures. However, the real temperature in the contact area is likely much higher, which can hardly be measured. Accordingly, this temperature is the lower threshold value of the arisen contact temperature.

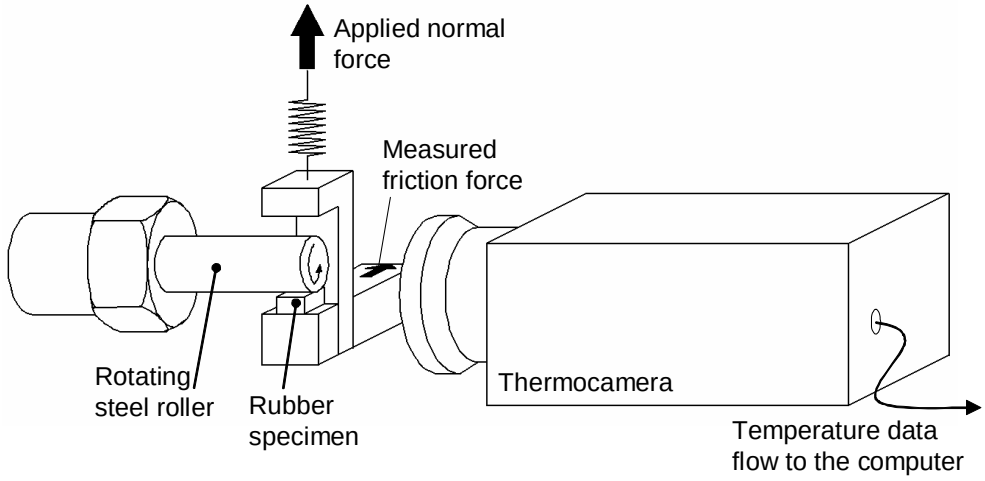

Figure 38: The set up of the ROP device with the thermo camera

6.8 FE Simulations of the Applied Tribotests

6.8.1 FE Model of the ROP test

The FE mesh of the ROP tests simulation is to see in Figure 39. In the tribotests the rubber specimens are fixed to an adequate sized steel plate. This steel plate is also involved in the FE model. The rubber specimen is 12 mm wide and 4 mm high. The modelled rubber specimen and steel plate are glued together. As it is well resolved at the enlarged picture in Figure 39, the mesh of the rubber specimen is

refined in the vicinity of the contact area. In the upper element layer the element size is 62.5 µm. The steel roller of the ROP test configuration is modelled as a perfectly rigid body.

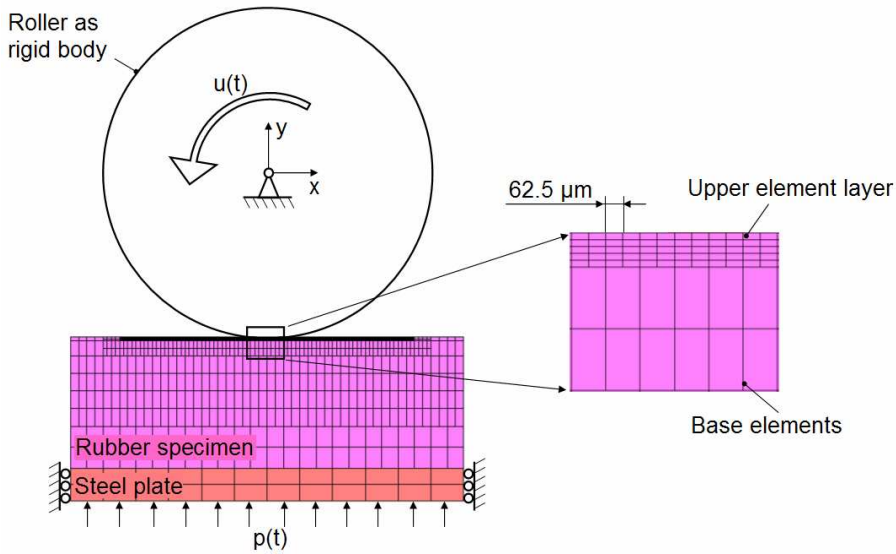

Figure 39: FE mesh of the ROP tribotest in the beginning phase of the tests and the applied constrains

The test configuration was simplified to a plain strain problem. Two types of material model were used. For the rubber a two-parameter Mooney-Rivlin material model was used. The material parameters for the different EPDMs are summarized in chapter 7.1.1. The material model of the steel plate follows the Hook's law (E=210000 MPa, ν=0.3). The model is built up from plane strain solid, quadratic, Hermann-type elements. Between the perfectly rigid roller and the rubber specimen an adequate coefficient of friction was applied. The COF values were derived from the related tribotests.

During FE analysis we have simulated different stages of the tribotests. Only the most interesting test stages were modelled. The chosen time intervals and applied normal loads for modelling are collected in chapters 7.4.4, 7.5.4, 0 and 7.7.4. In the different measurement stages the adequate wear track geometries (width (W_w) and depth (D_w), see Figure 40), normal loads and coefficients of frictions were applied. All of these data are known from the tribotests (see chapters 0, 7.5, 7.6 and 7.7). In Figure 39 and in Figure 40 three different models are shown for the EPDM 0 material modelling the ROP tribotest under 12 N normal load. In Figure 39 the model simulates the beginning stage of the wear test, without wear path. In Figure 40 the two models are showing the FE meshes simulating the test in the 2nd and in the 90th minutes. The deformation of the FE mesh as the wear track grows is obvious. By this

way the stress and strain states could be calculated for different measurement stages by the FE simulation.

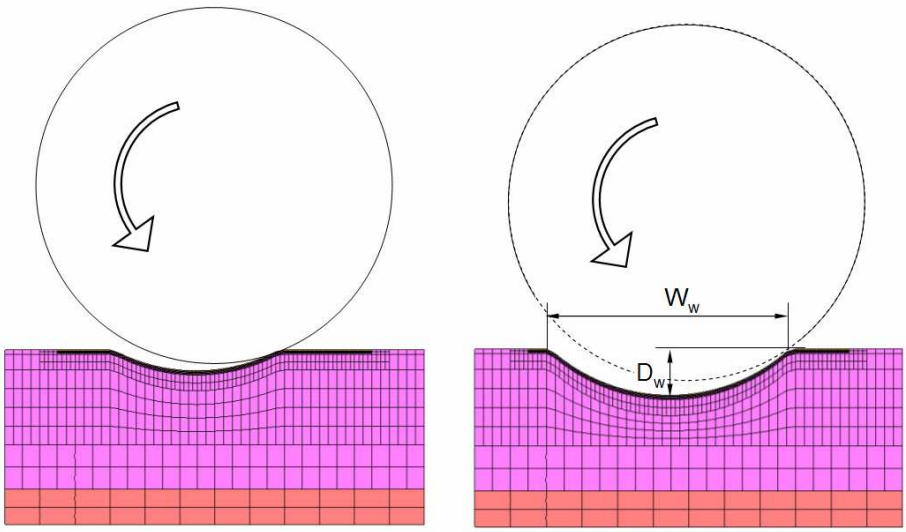

Figure 40: Change of the FE mesh, simulating different stages of the tribotests

The following constraints were applied during the simulations. A prescribed zero displacement in the “x” direction was applied for the nodes of the steel plate. The normal load was introduced at the bottom of the steel plate as a distributed pressure p(t) (see Figure 39). The value of the pressure was always adapted to the actual simulation. The middle point of the rigid steel roller was fixed in the “x” as well as in the “y” directions. A prescribed rotation was applied for the rigid roller u(t) (see Figure 39). The value of the introduced pressure p(t) and of the prescribed rotation of the rigid roller u(t) are controlled by time curves tc1 and tc2 (see Figure 41). The tc1 curve in Figure 41 controls the actual pressure value versus the time. In the model the applied pressure value is calculated by the multiplication of tc1 and p(t), (tc1·p(t)). The tc2 curve in Figure 41 controls the rotation speed, (radian / time) of the rigid roller. In the model the applied rotation limit is calculated by the multiplication of tc2 and u(t), (tc1·u(t)). The value of u(t) is chosen for 1. In this case the speed of the rotation is irrelevant, because we have no speed, or time dependent material or mechanical parameters in the model. The simulation goes on until the full sliding of the rigid roller on the rubber surface. The results of the simulations (nodal stresses) are collected from the second node array under the contact area, to avoid numerical instabilities of the FE calculation in the sliding contact zone. The temperature effect was not considered during the simulations, because over 20 ℃ the change of the EPDMs elasticity modulus is very small (see chapter 7.2). The additional work to

consider the effect of the temperature distribution would not justify the marginal benefit of it.

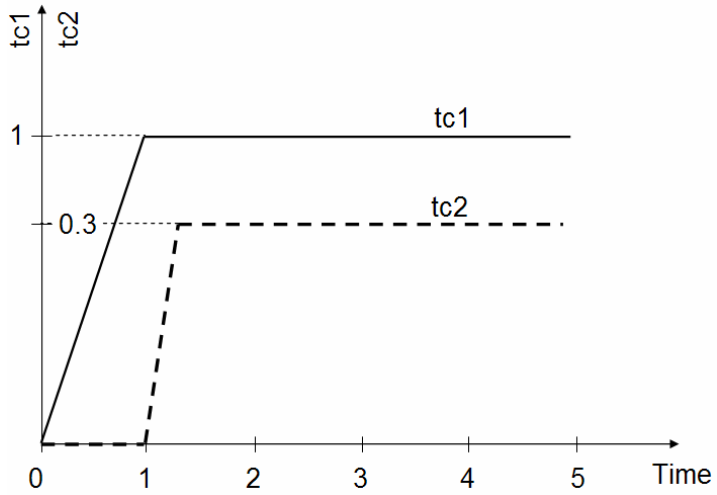

Figure 41: Time curves applied in the FE simulations of the ROP tests

6.8.2 FE Model of the Rolling Friction Tests

The model used in the simulation is shown in Figure 42. The rubber plate was defined as deformable whereas the sphere (ball) as a rigid body.

The dimension for the rubber plate is 37.6 mm x 27.4 mm x 4 mm, divided into 4256 elements (38*28*4). To increase the accuracy of the simulation and to decrease the computing time at the same time, the so called “local adaptivity” of “mesh adaptivity” was turned on, which was applied only to the deep coloured elements in Figure 42. This method increases the number of elements in the chosen region when a given mean strain energy density was reached. Based on trials in our case this value was 1.5 N/mm^2. In that way the mesh will be changed during the simulation. The original and the automatically modified mesh can be seen in Figure 42. The first picture shows the rubber plate and the rigid sphere in its starting position. The second picture (front view) shows the together pushed sphere and rubber plate (the upper sphere mesh represents the original position of the sphere). The third picture shows the position of the sphere at $t=T_p/2$, where the re-meshed part of the rubber plate is also visible.

The model was built up from 8-node solid Hermann type elements. No friction was applied between the rigid sphere and the rubber plate. A rigid flat surface was fixed onto the bottom of the rubber plate. This rigid surface and the bottom of the rubber plate were glued together as in case of the experiments.

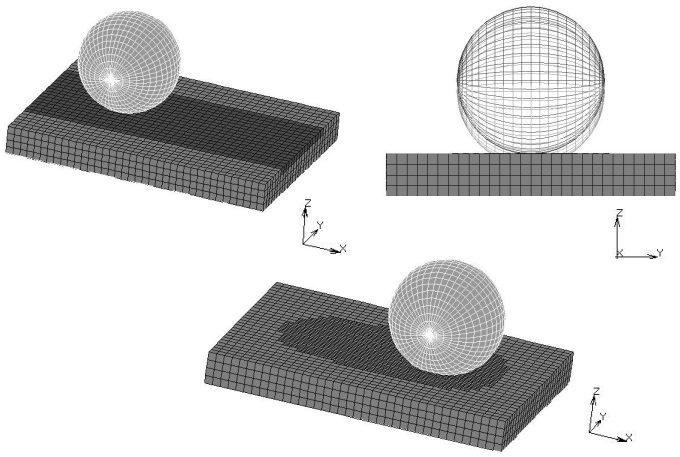

Figure 42: FE model at t=0 and at t=T_p/2 for the Oscillating-RBOP friction simulation

The load was applied by the prescribed displacement of the ball. The ball moved vertically (-z direction, cf. Figure 42) till a fixed position and pressed onto the rubber plate. The horizontal movement (prescribed velocity in direction x, cf. Figure 42) was applied to the rigid surface which was glued to the bottom of the rubber plate. Parallel to this horizontal reciprocating motion, the rigid sphere was driven with an angular velocity. The driving time curves of the prescribed displacements and velocities are summarized in Figure 43. The time curve for the vertical movement of the rigid sphere (tc1) is linear. At t=0 s the value of the tc1 is zero. Subsequently it increases linearly until t=1 s, where it will be 1. Afterwards this value remains constant until the end of the cycle (t=31 s). To ensure a normal force of 140 N, the value of tc1 (1) will be multiplied with a proper displacement value (~1 mm). The movement of the rigid surface at the bottom of the rubber plate and the angular velocity of the sphere can be described by the same time curve (tc2). To prescribe the right velocity and right angular velocity, the values of the sinusoidal time curve will be multiplied by 1.47 mm/s for the horizontal velocity of the rubber plate, and by 0.21 rad/s for the angular velocity of the sphere. The value of the sinusoidal time curve (tc2) is zero from t=0 s to t=1 s. In this way, the velocity of the rubber plate will be:

$$v(t) = 1.47 \sin\left(\frac{\pi}{15}(t-1)\right) \left[\frac{mm}{s}\right], \qquad (5.7.2.1)$$

while the angular velocity of the sphere can be described as

$$\omega(t) = 0.21 \sin\left(\frac{\pi}{15}(t-1)\right) \left[\frac{rad}{s}\right] \quad \text{if } 1s \le t \le 31s. \qquad (5.7.2.2)$$

The results of the FE simulation of the rolling tribotests are discussed in chapter 9.

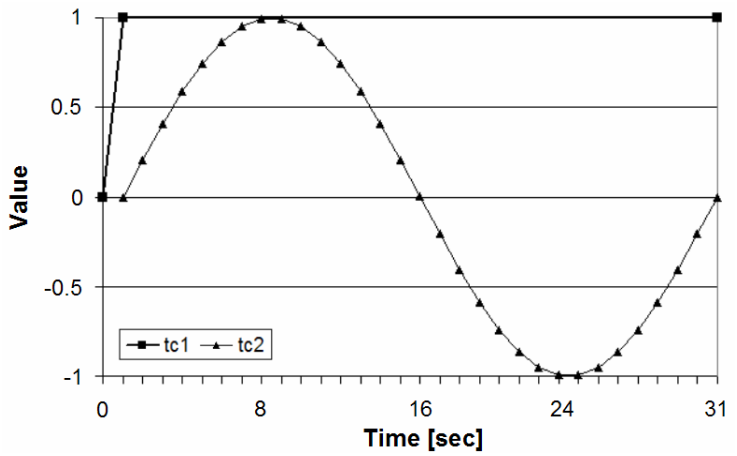

Figure 43: The driving time curves for the vertical displacement of the sphere (tc1), for the horizontal velocity of the rubber plate (tc2) and for the angular velocity of the sphere (tc2)

7 Results and Discussion

7.1 Tension and Compression Tests

The mechanical characterization of the investigated materials is of basic importance. However until now no correlation exists between the mechanical properties of an elastomeric material and its adhesive wear behavior. Nevertheless, the results of the mechanical tests may deliver important material properties which influence the wear mechanisms during dry sliding. The stress-strain curves of the tension and compression tests have another great benefit, namely one can use them to fit a related material model (see chapter 3.2.2). In Figure 44 the results of the compression and tension tests, in form of engineering stress versus strain are depicted. The engineering stress is determined as the quotient of the measured force (F) and the original cross sectional area of the specimen (A_0):

$$\sigma = \frac{F}{A_0}. \qquad (6.1.1)$$

The strain is expressed as it follows:

$$\lambda = 1 + \varepsilon, \qquad (6.1.2)$$

where

$$\varepsilon = \frac{\Delta L}{L_0}. \qquad (6.1.3)$$

In Equation 6.1.3 ΔL is the change of the specimen's length and L_0 is the original length of it. This type of description of the strain results that all of the resulted strains values are positive under both compression and tension. In the case of compression as larger is the compressive strain the closer the value of λ to zero will be. Under tension, the higher is the strain the higher positive number for λ will be noticed. The compression stresses are defined as negative, while the tension ones as positive stresses.

The tendencies for compression (cf. Figure 44 left) and for tension (cf. Figure 44 right) are basically the same. With increasing CB amount higher stresses develop in the EPDM systems. For compression tests one can observe an exception related to the mentioned tendencies; EPDM 0 (without CB) seems to be stiffer for higher compression strain values as EPDM 30. It needs to be noted that during compression tests there was no indication for the failure of the specimens. The tests were stopped

when a critical distance of the compression plates was reached. Further remarks about the failure of the specimens due to compression will be given later.

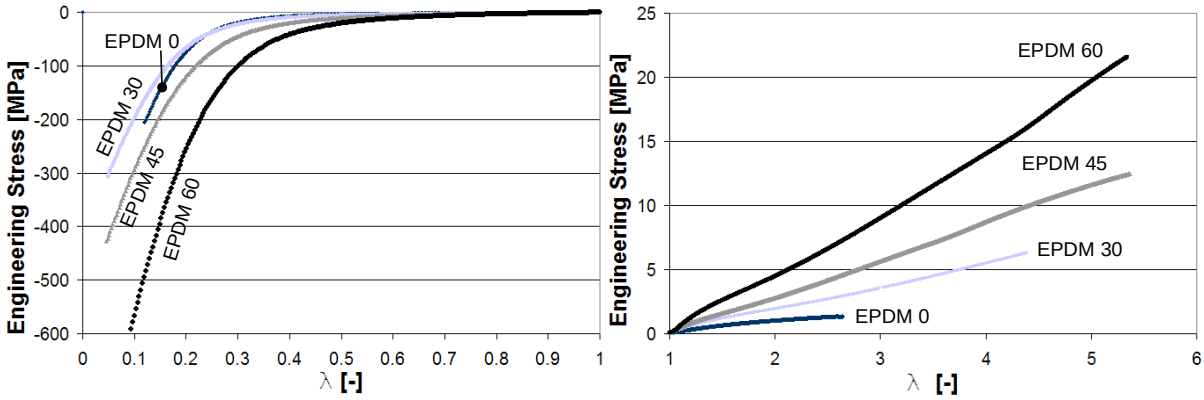

Figure 44: Engineering stress vs. strain for the EPDM rubber series for compression (left) and for tension (right)

In Figure 45 the true stresses are depicted versus the resulted strains. The true stress is determined as follows:

$$\sigma = \frac{F}{A_{def}}, \qquad (6.1.4)$$

where A_{def} - is the actual cross section area of the test specimen. Thus the cross section is steadily changing due to the tension or compression it needs to be expressed as the function of the strain. If we assume that the rubber is incompressible and that the strain is perfectly uniaxial, than it will be a simple geometrical problem (see chapter 3.2.2). For the tension tests in Figure 45 (right) one can see that the true stresses, compared to the engineering stresses (cf. Figure 44 right) are much higher, and the slope of the true stress vs. strain curves is also higher than for engineering stress vs. strain curves. However, the tendency as a function of CB remains the same for both the engineering- and the true stress-strain curves. In the case of compression tests the true stress (cf. Figure 45 left) values are smaller than the engineering compression stress values (cf. Figure 44 left), as the cross section of the specimen is increasing. The true stress vs. strain curves are showing that the CB filled EPDM rubbers undergo a yielding process, i.e. with increasing compression strain the true stress does not increase, but even decreases. This result is very important and unexpected. This yielding process is to observe by extremely high compression strains. For the unfilled EPDM no such yielding was found. After the compression tests all CB filled EPDM specimens showed a plastic deformation without any cracks at their surface. This was not the case for the specimens of unfilled EPDM which were cracked in addition. The most significant yielding was

observed over a strain value of 0.2. Considering the fact, that the unfilled EPDM proved to be stiffer than the EPDM 30 rubber (for compression at high strains), it can be surmised that the yielding process started earlier, at a strain value of ~0.25.

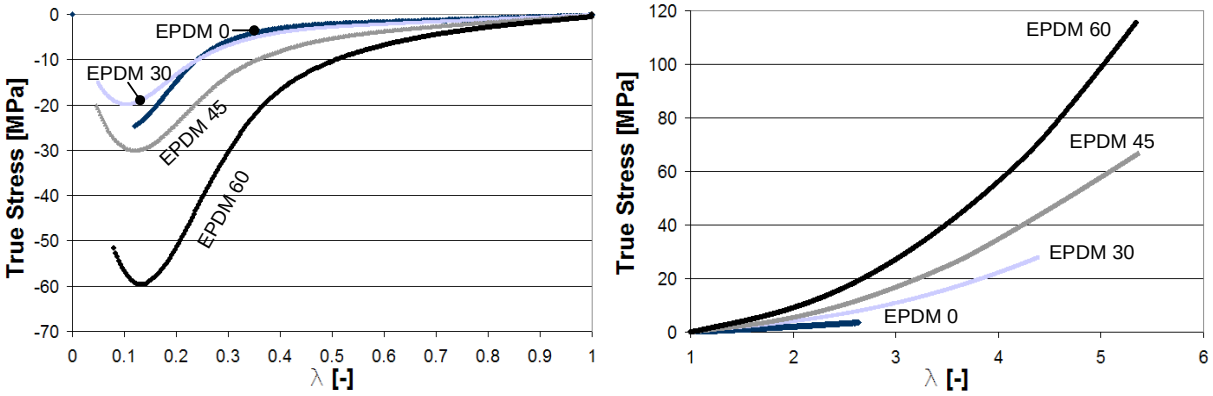

Figure 45: True stress vs. strain for the EPDM rubber series for compression (left) and for tension (right)

The ability of the CB containing EPDMs for yielding is of great importance. Although it is observed at extremely high compression strains we assume, that during dry sliding such conditions are reached. Under action of the asperities of the counter body in the elastomer such compression circumstances may developed which will trigger the yielding of the elastomer. Further on, the above showed mechanical tests were measured at room temperature but it is most likely that at higher temperatures (during the tribotests the temperature increase is significant) smaller strains are needed to reach the yielding process. This phenomenon may have significant influence on the sliding properties, as well as on the wear behavior of the rubber.

7.1.1 Mooney-Rivlin material model

As it was mentioned earlier the compression and tension test results will be used to create a two parameter Mooney-Rivlin material model. This kind of description for the elastomers nonlinear material behavior is detailed in chapter 3.2.2. In Figure 46 one can see the engineering stress results (compression and tension together) versus the strain. It is important to note that the Mooney-Rivlin material model needs to be fitted to the engineering stress versus strain curves not to the true stress - strain curves. In Table 3 the results of the Mooney-Rivlin fit are summarized. These parameters were determined experimentally, inserting proper C_1 and C_2 values into Equation 2.2.2.28.

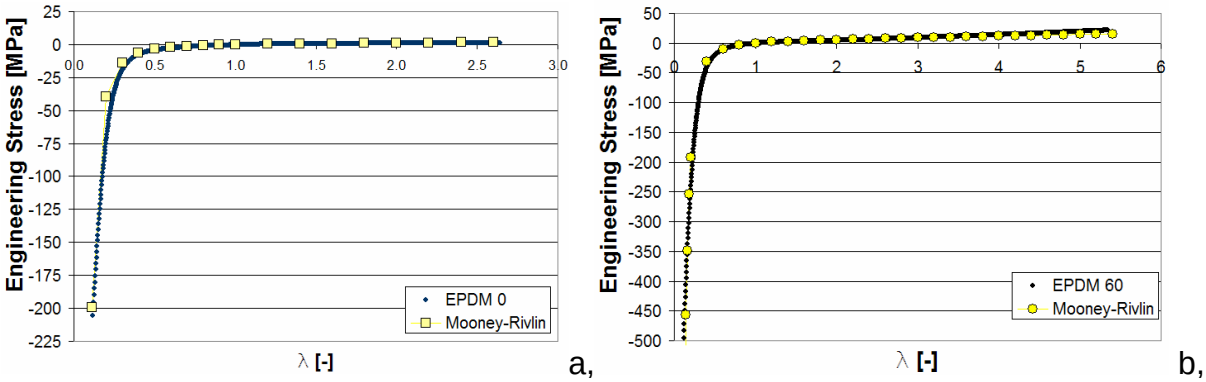

Figure 46: Compression-tension engineering stress vs. strain curves for EPDM 0 and for EPDM 60 and the related Mooney-Rivlin fits

Table 3: The calculated Mooney-Rivlin parameters for the EPDM rubbers studied

Mooney-Rivlin parameters	EPDM 0	EPDM 30	EPDM 45	EPDM 60
C_1	0.30	0.6	0.95	1.36
C_2	0.10	0.15	0.25	0.5

7.2 DMTA test results

7.2.1 Temperature range

In Figure 47 a-c DMTA results of the EPDMs with different CB contents are displayed. Figure 47-a depicts the change of the storage modulus (E´) versus the temperature (note that the scale of the "E´" axis is logarithmic). The effect of the CB content is clear with increasing CB the storage modulus increases as well. The E´ increment is most significant above the T_g in the rubbery plateau. Here the difference covers almost one order of magnitude. The effect of the nano-sized CB particles on the storage modulus is less significant below the T_g where the movement of the polymer chains is frozen in. The spectra in Figure 47-b and Figure 47-c will be discussed together. In Figure 47-b, the change of the loss modulus (E´´) versus the temperature is plotted. The value of E´´ is increasing with the increase of the CB content in the whole temperature range. On the contrary the proportion of the loss and the storage moduli ($\tan\delta$) decreases with increasing CB content, at least in the vicinity of T_g. The largest change in the viscoelastic properties of the CB filled EPDMs is to observe in the vicinity of the T_g. The loss factor peaks at T_g, where the value of E´´ is the highest compared to E´. Here, at T_g, segments of the crosslinked rubber are in motion and their kinetic energy in the neighbourhood can be absorbed. In ideal

case, when the active chain lengths in the rubber were exactly the same, the peak of the tan δ would locate at a given temperature thus the transition between the glassy and rubbery modulus would be very sharp. This is not the case which means that the active chain lengths of the rubber hava a certain distribution. The movement of these different chain lengths will be activated at different temperatures that is why the tan δ peak covers a fairly broad temperature range (-50℃ - 0℃) (cf. Figure 47-c). Because the active chain length basically determines the properties of the rubber the best way to characterize an elastomer is to determine its apparent mean molecular mass between crosslinks (M_c), as it was already mentioned in chapter 3.2.2 (see Equation 2.2.2.2).

A very important result of these DMTA tests is the influence of the temperature on the modulus of the EPDM compositions. This may be implemented into the FE simulation of the sliding friction tests. The heat development during sliding may strongly influence the material properties (the temperature reaches ~75℃) which should be considered by the FE models. However Figure 47 (-a and -b) suggests, that above 20 ℃ the change of the moduli is not significant. Therefore no additional benefit is expected when considering the temperature distribution in the samples by the FE simulation of the dry sliding tribotests.

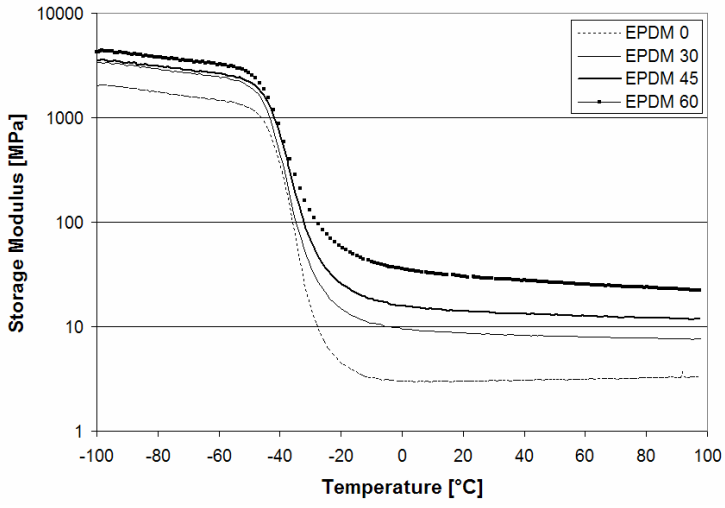

a;

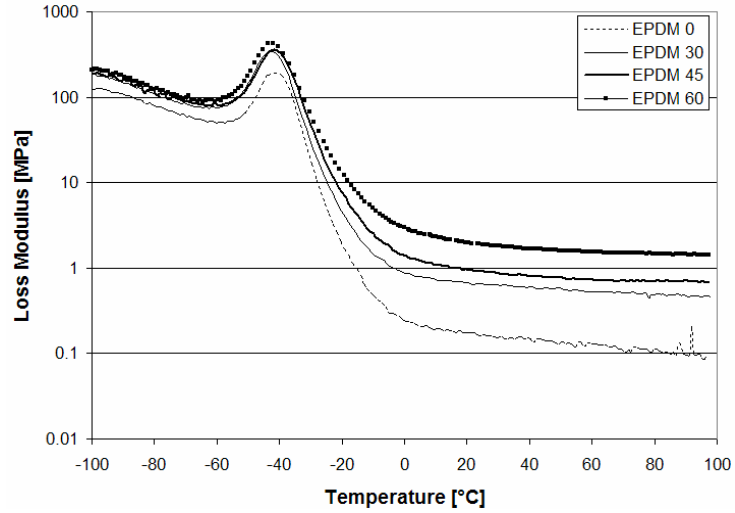

b;

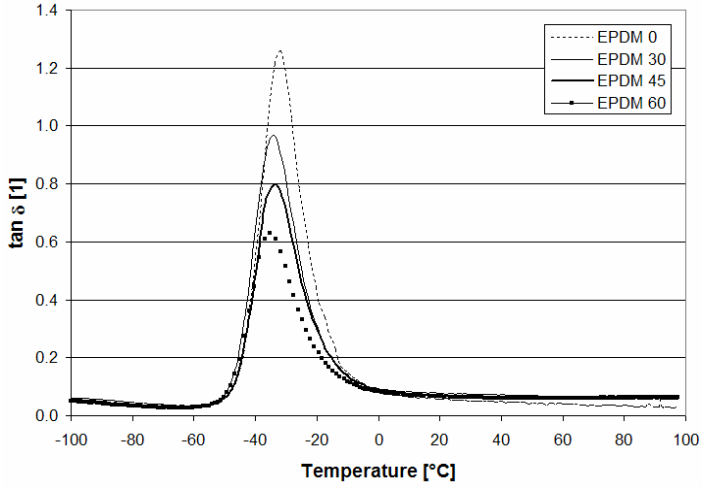

c;

Figure 47 DMTA results a; Storage Modulus (E´) - b; Loss Modulus (E´´) - and c; tan δ vs. the temperature measured at 10 Hz frequency

7.2.2 Frequency Range (EPDM 30)

Other interpretation of the DMTA results is the so called master curve (see chapter 2.3.2). To construct this master curve one needs to use the time-temperature equivalence principle which is usually referred to as Wiliam-Landel-Ferry (WLF) theory. Recall that DMTA measurements were carried out at different frequencies (1, 10, 100 Hz) and temperatures (from -100℃ to +100℃ with a temperature step of 5℃). To create the master curve (moduli or tan δ as a function of frequency) we need as input the E´, E´´ and tan δ vs. frequency curves measured at different temperatures (see Figure 48 an example of E´). In Figure 48 the test results of the EPDM 30 material are depicted where some temperatures are assigned. One can see that the highest storage modulus was measured at the lowest whereas the smallest one at the highest temperature. The largest change in the storage modulus vs. frequency curves occurs in the glass transition temperature (T_g ~ -45℃) range. Using the results depicted in Figure 48 one can create by the described shifting procedure (see chapter 2.3.2) the storage modulus vs. frequency master curve (cf. Figure 50 and Figure 51). The reference temperature was fixed at 20℃. As the shifting procedure of the master curve creation happens manually it has to be checked whether the related shift factors fulfil the requirements of the WLF theory. For this purpose the validity of the WLF-, or the WLF-Arrhenius equations (see Equations 2.3.2.1 -.2.3.2.3) should be checked, whether or not to the experimentally determined and calculated shift factors agree with each other (cf. Figure 49).

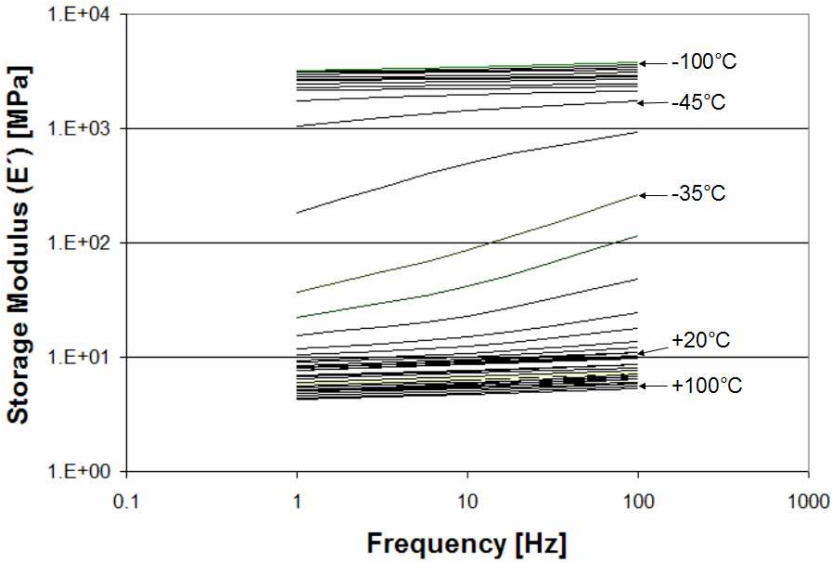

Figure 48: DMTA results at different temperatures in the frequency domain on the example of EPDM 30

During the fitting procedure of the WLF equation to the experimentally determined shift factors it was found, that the WLF function, similar to the theory, describes the curse of the shift factors only in the vicinity of the T_g. Therefore the WLF-Arrhenius equation was also adopted. For the lower and upper limit of the WLF equation (T_C^L and T_C^U, respectively) -45℃ and +35℃ were deduced. All c onstants to describe the shift factor vs. temperature curves are collected in Table 4. This kind of description allows us to transpose the master curve to required reference temperature (between -100℃ and +100℃). By this wa y a time and temperature dependent “material law” can be determined.

Table 4: The WLF and WLF-Arrhenius constants of the master curve for the EPDM rubber with 30 phr CB content. Reference temperature, T_{ref}=20℃. Note: the meaning of the parameters is described in chapter 2.3.2.

	K_1 [-]	K_2 [^oC]	T_C^U [^oC]	T_C^L [^oC]	$A_E^U \left[\frac{J}{kmol}\right]$	$A_E^L \left[\frac{J}{kmol}\right]$
EPDM 30	5.8	105	35	-45	$3.6 \cdot 10^6$	$2.4 \cdot 10^7$

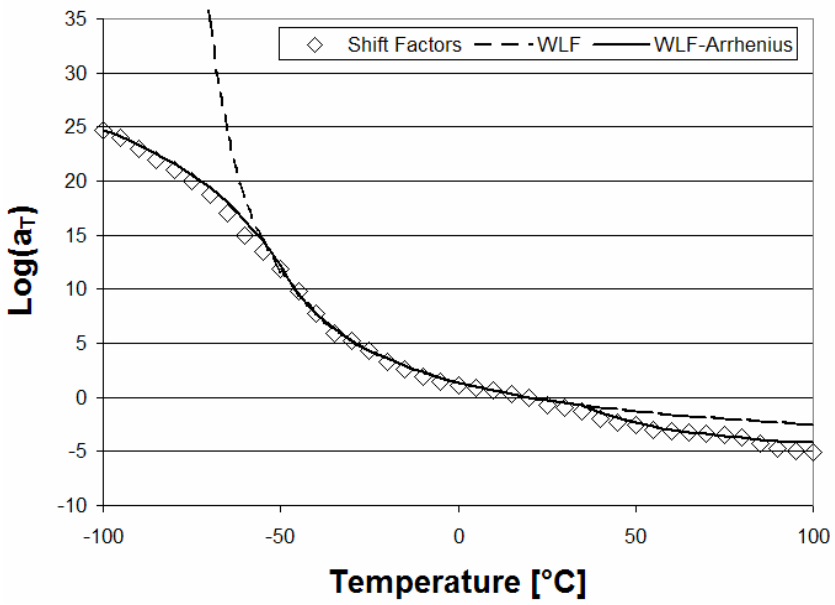

Figure 49 Experimental shift factors after manual shifting and those computed by the WLF and the WLF-Arrhenius equations, respectively for the EPDM 30

Using the already determined and checked shift factors, one has the possibility to create also the E´´ and tan δ master curves. This is shown on the example of the

EPDM 30 material (cf. Figure 50). Comparing these master curves with the initial DMTA curves (where the change of the same properties against the temperature was depicted- cf. Figure 47 a-c), one can notice, that the shape of the curves is similar. Only the tendencies are changed as decreasing temperature corresponds to increasing frequency. It means that for example the E´ values measured at low temperatures correspond to high frequency DMTA results and the E´ values measured at high temperatures correspond to low frequency DMTA results. This depiction of the DMTA results can be very useful for the design of vibration damping elements, of rubbers or for the multi-scaled analysis of sliding. In the latter case where the different scaled roughness peaks of the counter body cause dynamic excitations in the elastomer in a broad frequency range, so that the frequency dependence of the material properties has to be taken into consideration.

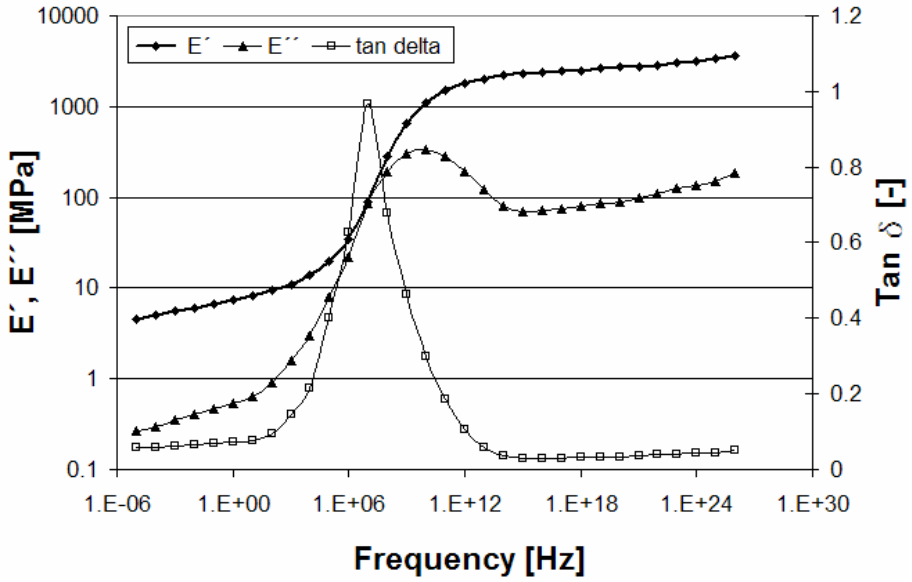

Figure 50 The E´, E´´ and Tan δ master curves of the EPDM 30 material

7.3 Viscoelastic Material Model (EPDM 30)

As it was discussed in chapter 2.3.3 the ViscoData [32] software was used to create the adequate 15-term Maxwell model (cf. Figure 13) for the EPDM 30 material. The results of the fitting procedure are shown in Figure 51. It is clearly to see that the Maxwell-type description of the master curve is fairly good, which will be proved also by the FE simulation results (see chapter 8). The parameters of the created 15-term Maxwell model are collected in Table 5.

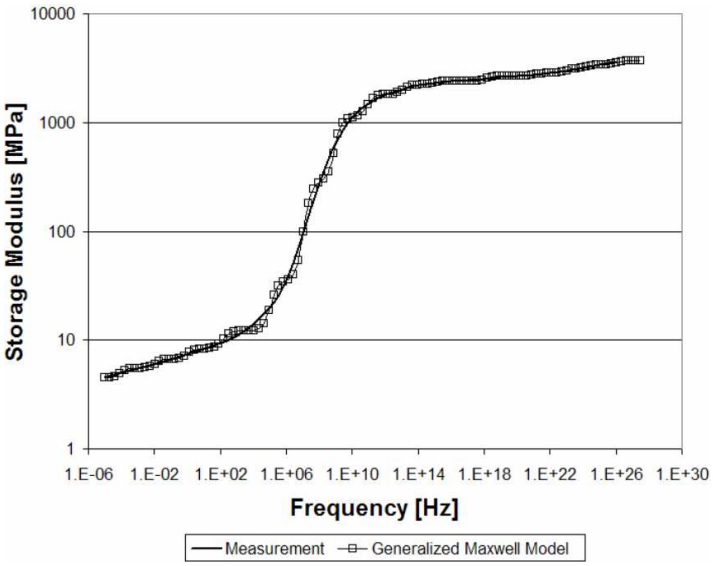

Figure 51: The E´ master curve of the EPDM 30 material and the fitted 15-term Maxwell model

Table 5: Parameters of the fitted 15-term Maxwell model. Note: the meaning of the parameters is detailed in chapter 2.3.3.

$E_{(zero)}$ [MPa]	$3.7 \times 10^{+03}$	$E_{(infinite)}$ [MPa]	$4.5 \times 10^{+00}$
τ_1 [s]	$1.61 \times 10^{+03}$	e_1 [-]	2.83×10^{-04}
τ_2 [s]	$1.29 \times 10^{+01}$	e_2 [-]	3.12×10^{-04}
τ_3 [s]	1.53×10^{-01}	e_3 [-]	4.45×10^{-04}
τ_4 [s]	9.89×10^{-04}	e_4 [-]	1.03×10^{-03}
τ_5 [s]	1.18×10^{-06}	e_5 [-]	6.09×10^{-03}
τ_6 [s]	8.51×10^{-09}	e_6 [-]	6.74×10^{-02}
τ_7 [s]	1.42×10^{-10}	e_7 [-]	2.22×10^{-01}
τ_8 [s]	1.80×10^{-12}	e_8 [-]	1.90×10^{-01}
τ_9 [s]	1.27×10^{-14}	e_9 [-]	1.12×10^{-01}
τ_{10} [s]	2.00×10^{-16}	e_{10} [-]	5.07×10^{-02}
τ_{11} [s]	1.10×10^{-19}	e_{11} [-]	6.91×10^{-02}
τ_{12} [s]	1.38×10^{-22}	e_{12} [-]	4.59×10^{-02}
τ_{13} [s]	1.62×10^{-24}	e_{13} [-]	8.62×10^{-02}
τ_{14} [s]	6.62×10^{-26}	e_{14} [-]	6.76×10^{-02}
τ_{15} [s]	1.82×10^{-27}	e_{15} [-]	7.87×10^{-02}

7.4 Results of the tribotests on EPDM 0

7.4.1 Wear and wear mechanisms

The wear results show that significant wear occurs in the unfilled EPDM rubber specimens during dry sliding (cf. Figure 52). In the tree dimensional contour plot of Figure 52 one can see the loss volume in mm^3 versus the normal load and testing time. At the beginning of the tests the loss volume rapidly increases. In addition, the related increment enhances further with increasing normal loads. The initiation phase ends after 2- 10 minutes. Afterwards, it in the steady state phase, the slope of the loss volume vs. time curves radically decreases. This reflects a slow down in the wear process. The loss volume increases linearly with increasing normal load until 10 N. After it at 12 N normal load the observed wear will be larger during the initiation as well as in the steady state phase. At 12 N normal load the running-in phase is extremely short (2 min) and in the steady state phase only a marginal wear happens. The pretty regular form of the contour plot (i.e. loss volume vs. time and normal load) suggests that during the dry sliding tribotests of the neat EPDM the wear mechanisms do not change.

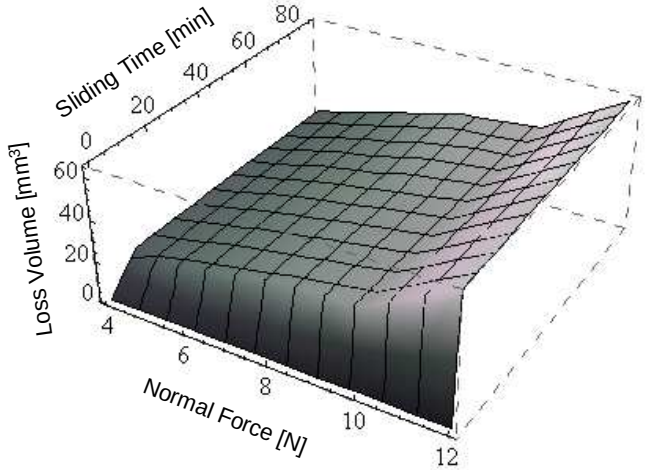

Figure 52: Loss volume results versus the testing time and applied normal force in a three dimensional plot

The width and the depth of the wear tracks were measured after the tests using white light profilometry (see Chapter 5.3.2). It was found, that the shape of the wear track is not a regular elliptic one as expected (cf. Figure 53). With increasing normal load, the cross section of the wear track adopts a pipe-like shape. The cross sections in Figure 53 were drawn based on the average width, depth and Δ measured by profilometry. The value of δ determines the location of the deepest point

relative to the edges of the wear tracks. Note that with increasing normal load the contour of the track deviates more and more from the elliptic one. This can be in linked with the overall deformation of the specimen due to the large friction stresses, as it will be shown later in chapter 6.10.4 in respect to the FE simulation results.

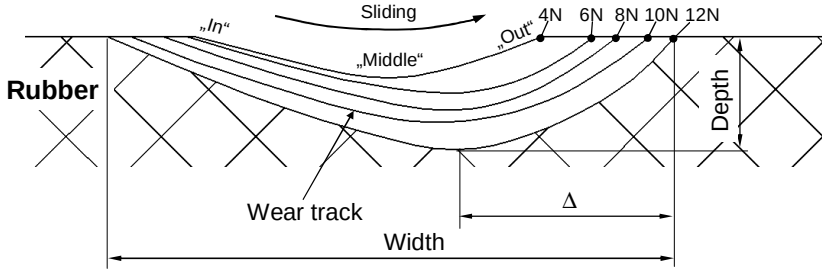

Figure 53: Change of the contour of the wear track as a function of the normal load

For the investigation of the wear mechanism the evaluated wear tracks were divided into three parts based on the actual positions (cf. Figure 53). The “in” section characterizes that part of the wear track where the steel roller enters the contact region. The “middle” part is the deepest region of the wear track and the “out” designated part is the end of the track where the steel rollers surface leaves the contact area. Further on, this designation will be used for all cases.

The SEM pictures in Figure 54 show the typical worn surfaces of the neat EPDM rubber in the mentioned three regions. In Figure 54 a and b the “in” regions of the wear track are shown after 90 min under 4 N normal load (a) as well as after 1 min testing at 12 N normal load (b), respectively. A stair-like structure appears as a result of a permanently surface erosion of the specimens. In deeper regions of the surface a significant amount of abraded wear particles is deposited. This result suggests that the basic wear mechanisms do not change with changing testing parameters. In Figure 54 c and d one can see the “middle” part of the wear tracks after 90 min tests by 4 N and 12 N normal loads, respectively. In these relatively flat regions the surface structure is formed by crack development and growth. The cracks are likely initiated at the surface perpendicular to the sliding direction. After that their direction of growth is more or less parallel to the sliding direction. The crack opening process and the deposition of wear particles into the cracks is well resolved in these figures. In Figure 54 e and f the worn “out” regions are shown after 90 min tests at 4 N and by 8 N normal loads, respectively. In these pictures again the stair-like structure is present, but the deep and high edges of this topography are positioned opposed to those in the “in” section in Figure 54 a and b. In the “out” section again

prominent wear particle deposition is to observe and basically no change in the wear mechanisms can be deduced.

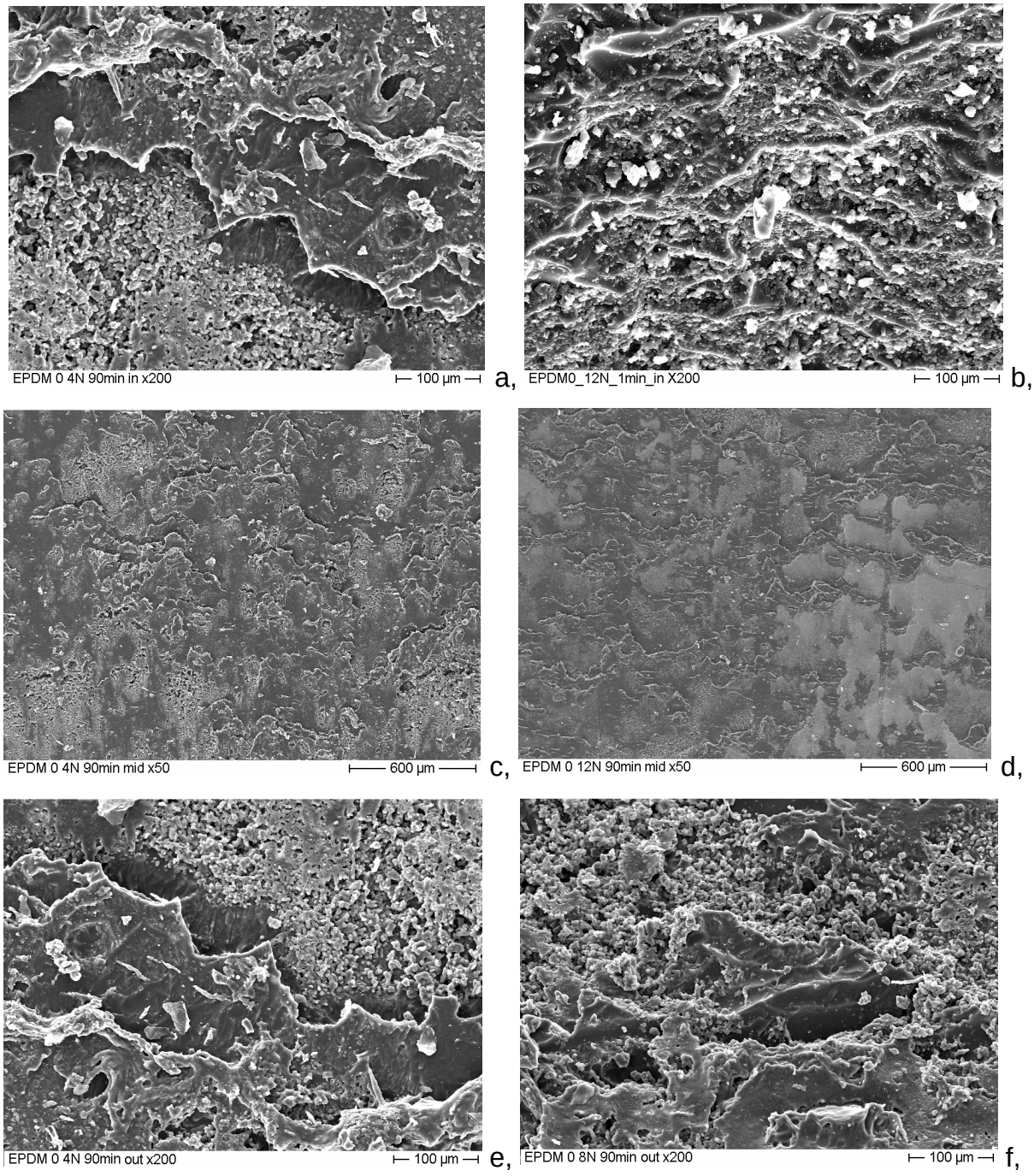

Figure 54: SEM pictures of the wear tracks in different stages of the ROP test on EPDM 0 - a; 4N after 90 min “in” -b; 12N 1min “in” -c; 4N 90 min “middle” -d; 12N 90 min “middle” -e; 4N 90 min “out” -f; 8N 90 min “out”. Note: sliding direction is downward.

A schematic sketch of the estimated wear process, as well as of the groove development is given in Figure 55. Different stages of the wear process are assigned

by numbers. The top picture in Figure 55 shows the schematic test set up with the rotating steel shaft and deformed rubber plate. The first picture shows the estimated position of the first crack on the rubber surface. This initiates the wear process. The growth direction of the first crack is at first downward (i.e. in depth direction), after that the subsurface crack begins to grow in the sliding direction (cf. pictures 1 and 2 in Figure 55). The crack propagation (crack opening) produces a rubber tongue which finally breaks off from the surface and it will be rolled in the sliding direction (cf. pictures 3 and 4 in Figure 55). The edges of this elementary wear track are the ideal initiation places for further cracks (cf picture 5 in Figure 55). The new cracks are also growing, whereby producing a larger wear track and more and more wear debris. Especially large cracks may developed at the right side edge of the wear track, thus the frictional stresses endeavour to open more and more already existing cracks (cf. pictures 6 and 7 in Figure 55). The mechanism of the groove growing is depicted in pictures 8 and 9 in Figure 55. Pictures 10 and 11 show the raw and the “refined” contour of the groove produced. To have a more realistic overview of the wear process we need to refine this crack growth process as it is shown in pictures 12 and 13 in Figure 55. The picture series in Figure 55 summarizes schematically, how the pipe-like wear contour might has been appeared. Furthermore the correctness of this phenomenological sketch will be proved later by FE simulation (cf. chapter 7.4.4).

7.4.2 Coefficient of Friction (COF)

The coefficient of friction results are summarized in a similar contour plot as above for the loss volume in Figure 56. Generally it can be established, that the value of the COF increases with testing time at every load level. A substantial increase of the COF values was observed in the wear initiation phase of the tests. Another important point is that the COF decreases with increasing normal load.

There are basically three effects which dominate the COF. One of them is the temperature: with increasing temperature the mobility of the polymer chains increases and proportional to it their “adhesive properties” are enhanced. This phenomenon may explain the increase of the COF.

The second important influencing factor is the presence of the wear particles. The wear particles are permanently rolled toward the sliding region. Due to the good adhesion they adhere to the steel shaft, so they will be rolled again and again over

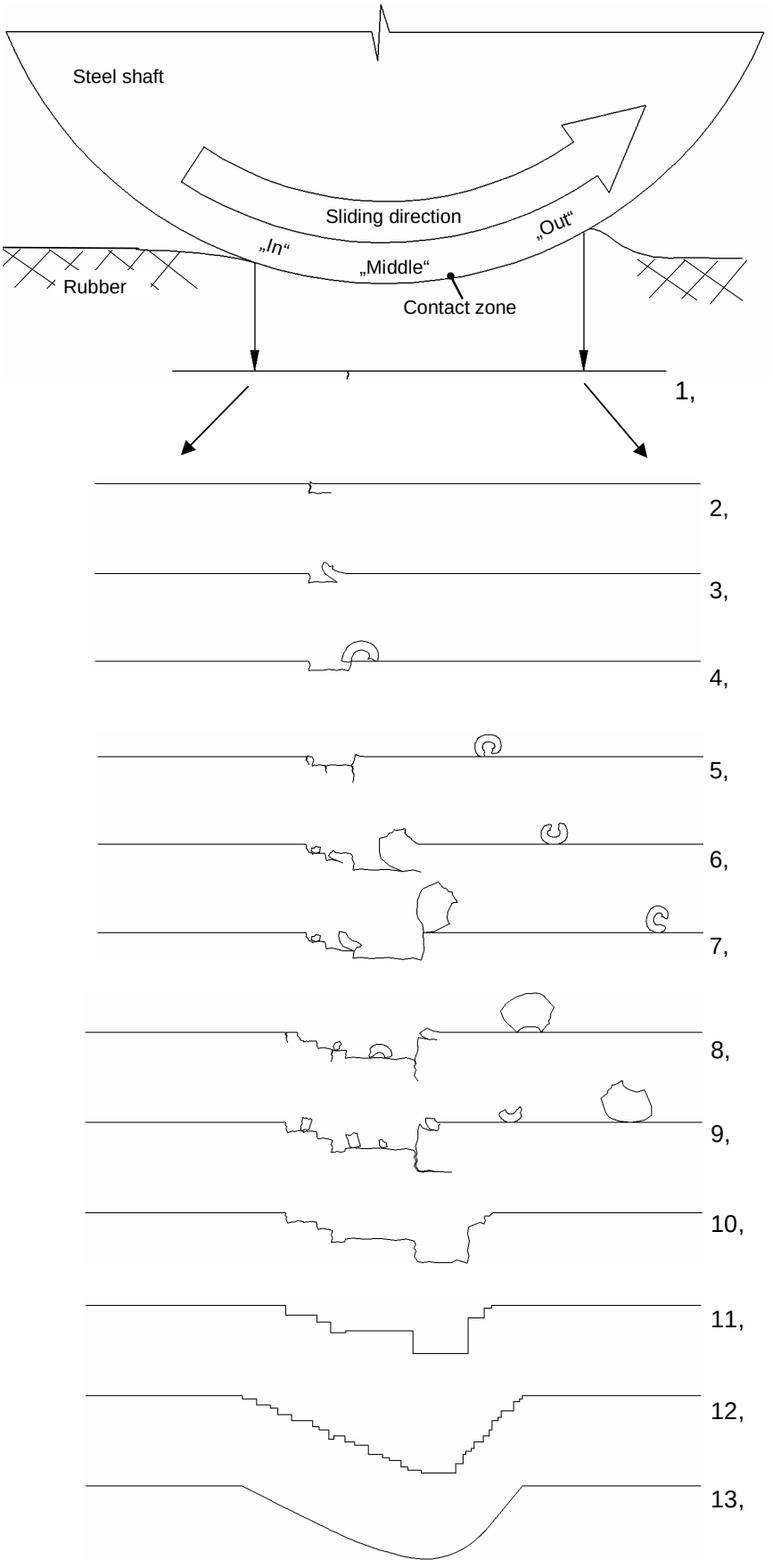

Figure 55: Schematic sketches of the wear processes in different stages of the ROP tribotests

the contact area (cf. Figure 55 -4 -8). Whether they act as a lubricant (film) and thus reducing the COF, or the opposite occurs due to their rolling resistance (hysteresis, microslip, etc…) is not clear at the moment.

The third dominating factor is the geometry of the wear track. The load distribution may be very complicated in the deformed state of the rubber specimen. This may disturb the friction force measurement and even cause undesired vibrations.

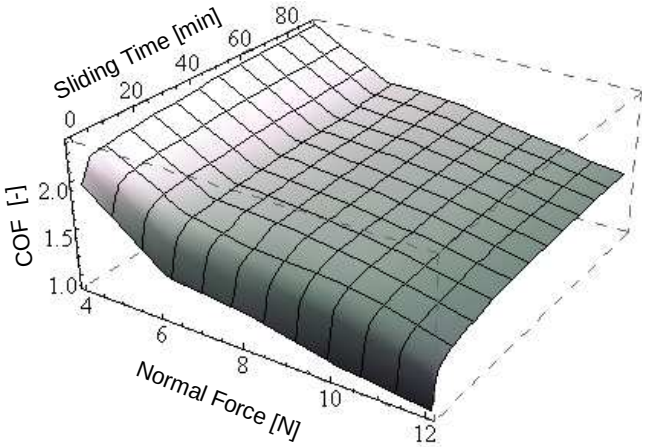

Figure 56: COF change versus the testing time and normal load for the EPDM 0 under ROP

7.4.3 Temperature development

The temperature development measured (cf. Figure 57) corresponds the expectations. With time and with increasing normal load the temperature increases. At constant parameters, just like sliding speed and material pairs in the corresponding test configuration, the temperature rise is controlled only by the normal pressure distribution (cf. Figure 58) and the actual COF (cf. Figure 56). We may assume that the heat development is proportional with the frictional loss power (see Equation 6.4.3.1).

$$P_{loss} \approx F_N \cdot \mu \cdot v \qquad (6.4.3.1)$$

However, the COF decreases with increasing normal load, namely by 4N the maximal COF value is ~2.5, and until by 12N the reduced value of the COF is about ~1.6. But this reduction is not as significant as the increase in the normal load (or normal pressure), thus the product of these terms will also increase.

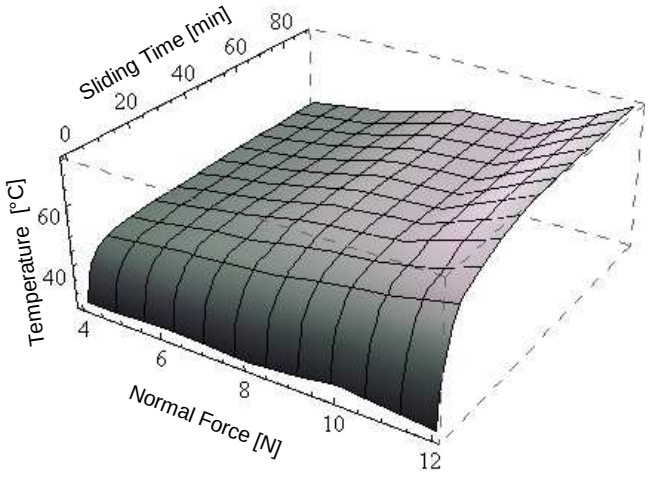

Figure 57: Temperature change versus the testing time and normal load for the EPDM 0 under ROP testing

The value of W_{loss} (frictional loss work) contains the viscoelastic and plastic deformation energy losses which occurred between the surface asperities of the sliding pairs and contains also the crack propagation energy affecting the wear. High temperature peaks are generated due to hysteresis and irreversible deformation at surface positions where large deformations evolve. The related flash temperature peaks are distributed over the whole contact surface (“integrated”) as well as over the upper material layer. This strongly decreases the average temperature which has been measured. The crack propagation is also associated with temperature rise due to the large deformations at the crack tips. It is important to note that the heat development during crack growth influences markedly the crack propagation, as it is shown for example in reference [68]. It means that the wear process can also be influenced by the temperature distributions. Another temperature related property change is connected with the adhesion ability of the rubber material [99, 100, 101]. The consequence of it is that COF increases with increasing temperature. Furthermore, the stiffness of the material is usually also changing with the temperature. But as the DMTA response in Figure 47 shows there is no significant reduction in the E-modulus above room temperature, so this effect is negligible in our case.

The above discussion substantiates that to the changing temperature can strongly influence the wear and sliding properties. That is why we followed also the temperature development during tribological tests.

7.4.4 FE simulation results

Due to the low stiffness of the investigated elastomers, as well as due to their high COF (or friction stresses) the specimens are subjected to large deformation during the tribotests. This geometrical nonlinearity is not easy to handle analytically. A further challenging task is to consider the nonlinear material behavior of the rubber. This makes the analytical study of the stress and strain states during the tribotest very difficult. The complexity of this contact mechanical problem was the driving force to carry out FE investigations. For the EPDM 0 material 9 stages of the tribotests were analyzed. These stages are summarized in Table 6. During modeling the 0 min testing time no wear was assumed. So the contact area from the rubber side was considered as a perfectly flat surface. In the subsequent time stages the wear tracks were modeled as circle shaped cuts in the surface of the specimen with the identical with and depth as measured on the specimens after the tests. The average COF value measured was also considered for every stage. The COF in single simulations was determined as the proportion of the vertical and horizontal reaction forces at the perfectly rigid roller after sliding of the contacting surfaces. However, to make further conclusions on how the contact geometry affects the COF, detailed FE simulations with more accurately applied COF laws (taking into account sliding speed, pressure and temperature) are needed.

The applied simplifications did not influence negatively the goodness of the FE simulations. In Figure 58 a-c one can see the diagrams based on FE calculations. These diagrams show the distribution of the normal pressure in the contact area for different loading situations. Corresponding to the expectations the normal load distribution along the contact lines shows higher values the higher normal load was applied onto the shaft. As it is well discernible, the normal pressure distributions are strongly distorted due to the high friction stresses. The related traces do not follow the regular Hertzian contact stress distribution.

During the simulation the middle of the contact region (0) was first determined as the symmetry line of the model (see Appendix 1 Figure 95). In follow-up steps the middle point of the contact area was determined and it was considered as the actual center of the wear groove for the next simulation step. Due to the large deformations at the end of the first simulation stage, for example at 4 N and 0 min, the middle point of the contact area was moved away from the geometrical symmetry axes. Because of the variable middle point of the contact area, the position of the wear track

changed during simulation as a function of time. The movement of the middle point of the simulated wear track is seen also on the related diagrams, where the 0 point at the “x”-axis means the symmetry axis of the model. The shift in the model parameter with the contact length (especially for the simulation results with 8- and 12 N loads) suggests that a pipe-like wear track contour develops. If one compares the change in the contact region in Figure 58 with those schematically shown results, in Figure 53, fair correlation can be established between the FE simulations and the tribotest results. At 4N normal load the contour of the wear track is symmetrical, but with increasing normal load the pipe-like course of the track will be more and more characteristic (cf. Figure 53). The same process is to observe in Figure 58 a-c, where the middle point of the wear track is shifted more and more in consecutive time stages with increasing normal load.

Table 6: Load cases for FE simulations of the ROP tribotest by EPDM 0

Normal load		**4N**	**8N**	**12N**
Time [min]	Initial phase	0	0	0
	Running-in	10	5	2
	Steady-state	90	90	90

In the picture series Figure 59 a-c one can see the deformed FE mesh in case of 12N normal load for the simulated time stages (e.g. in 0, 2 and in 90 minutes). In Figure 59 a-c it is well resolved that the mean deformations show always in one direction (showing by arrows). Furthermore, in Figure 59 c at the left side of the wear track the two contact bodies separate from one other. This suggests that the wear arises at the opposite side (“out”-region) of the contact area, corresponding to the experimental observations (cf. Figure 53). Further comments and explanations related to the FE simulations (designations and theory) are summarized in Appendix 1 (chapter 11.1).

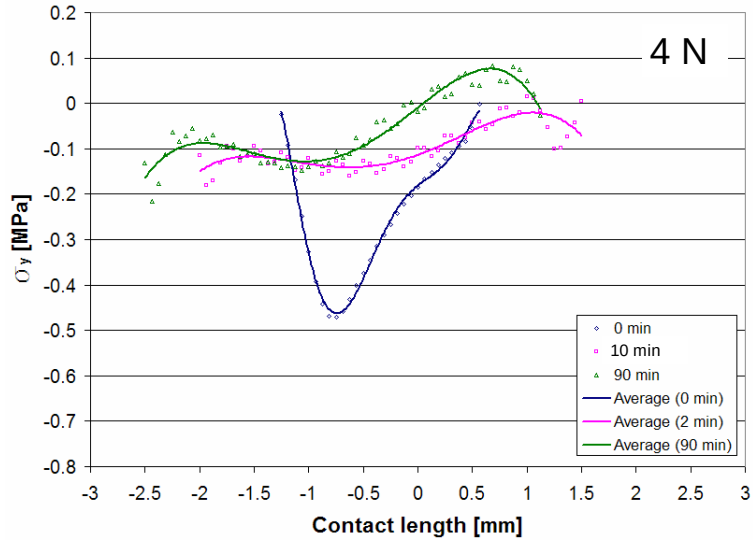

a,

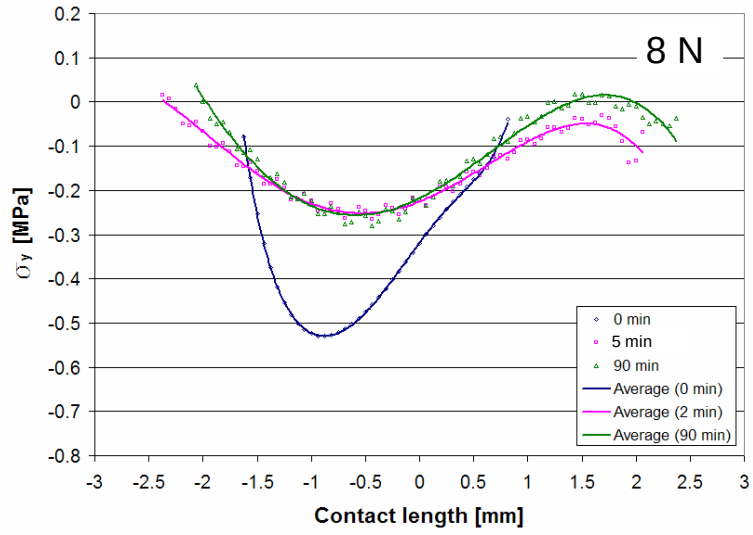

b,

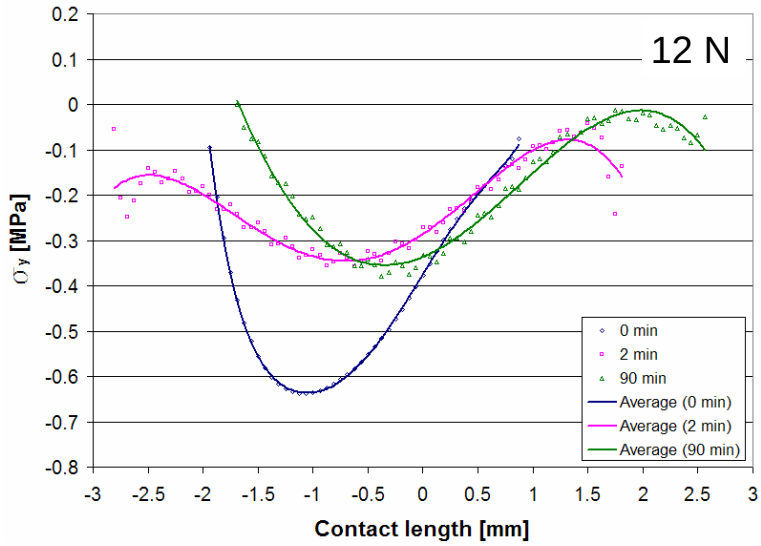

c,

Figure 58: Change of the σ_y –normal pressure distribution with testing time for three different load cases namely –a; 4N –b; 8N –c; 12N. Notes: the entering “In” side of the contact region is represented in the negative range of the contact length, the sliding direction shows right.

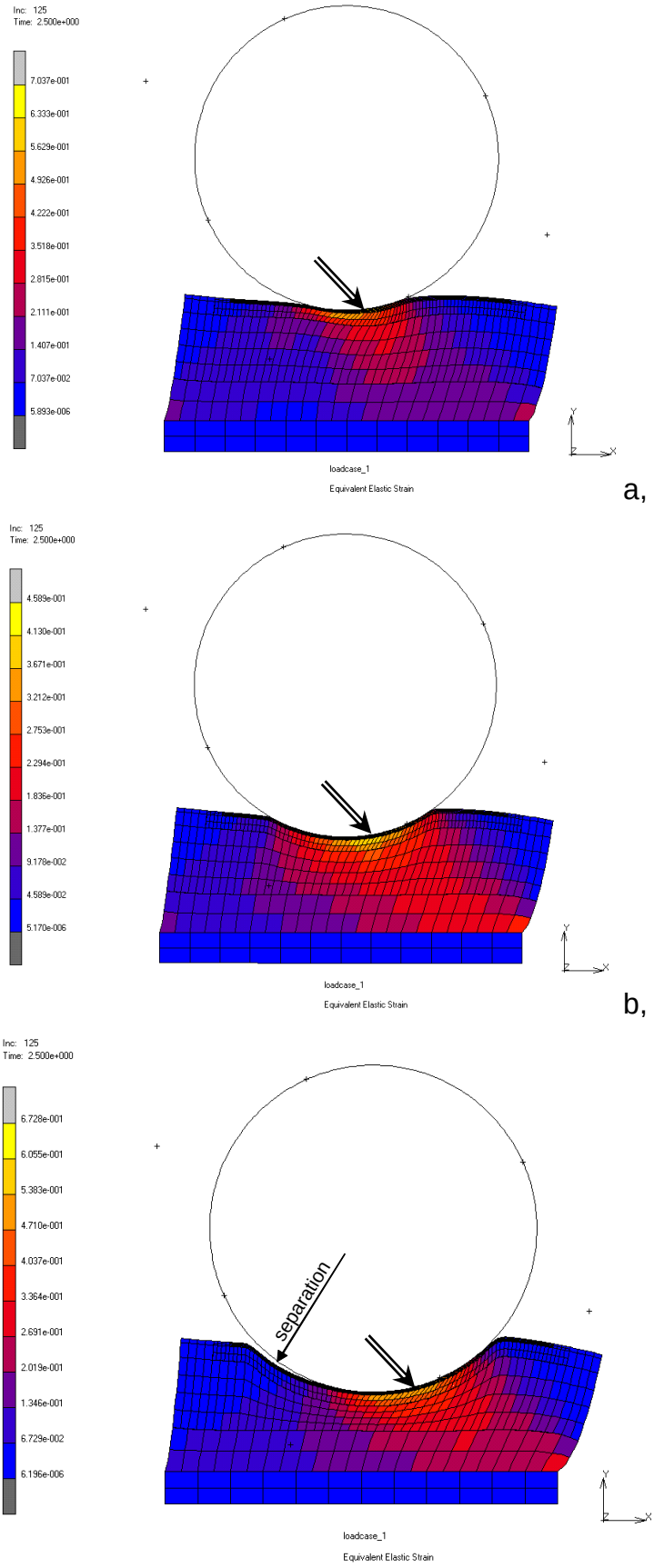

Figure 59: Deformed shape of the FE mesh at 12 N normal load when simulating the effect of testing time. Designations: a; 0min, b; 2min, c; 90min.

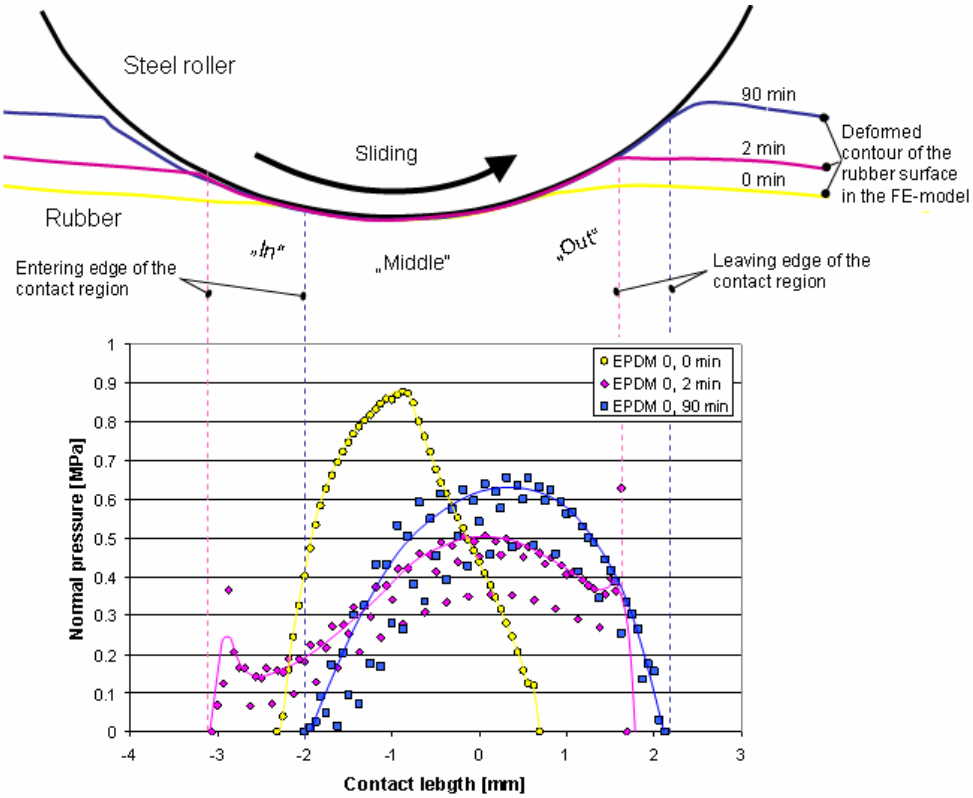

Figure 60: Normal pressure distributions (FE results) for EPDM 0 under 12 N normal load, along the contact length, for three different time stages: initiation (0-min), running-in (2 min), steady-state (90 min)

In Figure 60 the FE simulation results for the EPDM 0 material (schematic sketch of the contact situations in different testing times as well as the normal pressure distribution in the contact region) are illustrated. The dashed lines show the entering “In” and the leaving “Out” edges in the contact region for different testing times. In the diagram the yellow curve represents the normal pressure distribution for the initial phase of the tribotest (0 min). Due to the acting tangential stresses on the surface, distortion of the normal pressure distribution is observed. The course of the normal pressure distribution for the running-in phase of the tribotests (2 min) show deformations due to the appearing wear track on the surface (cf. purple curve in the diagram in Figure 60). Local pressure peaks at the edges of the modelled wear groove (cf. purple curve in Figure 60) can be observed. This is not the case for the steady-state results (90 min), where the contact area is within the modelled wear track (cf. blue curve in Figure 60). The dislocation of the maximum normal stresses on the right side of the diagram (in Figure 60) demonstrates also the formation of the typical pipe-like contour of the wear groove (cf. Figure 53).

7.5 Results of EPDM 30

7.5.1 Wear, Wear mechanism

This is usually expected loss that with increasing normal load, the measured wear or loss volume also increase when the same material combination and test method are applied. Contrary to this expectation, the ROP results are very surprising for the EPDM rubber containing 30 phr CB. Though in general, an extremely large scatter is characteristic for tribological tests, the related test results were reproducible. The 3D contour plot shows the loss volume as a function of normal load and sliding time (cf. Figure 61). In Figure 61 one can see that above a threshold normal load (6 N) the measurable loss volume decreases instead of increasing. Moreover, the larger is the applied normal load (above the threshold 6 N) the smaller the measured loss volume is. Assuming the correctness of the test results, this fact suggests a complicated interaction of the parts within this tribosystem. The results in Figure 61 indicate a characteristic running-in phase at 4 N normal load. This fast-wear running-in period is less remarkable under higher load levels. At 6 N normal load the wear is almost linear with the adopted time. On the other hand the prominent wear decrease by increasing normal load needs to be explained. In addition and a plausible explanation for the maximum loss volume at 6 N normal load at high sliding time should be found.

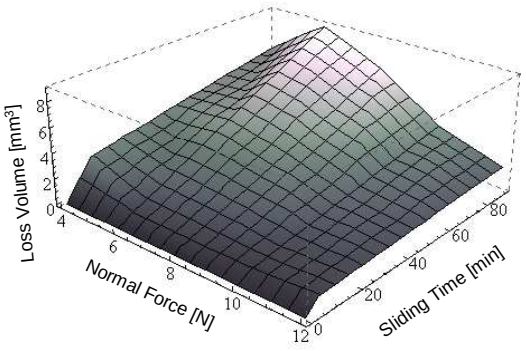

Figure 61: Loss volume versus testing time and versus the normal force for the EPDM 30 under ROP conditions

SEM pictures were taken from the worn surfaces. The SEM pictures from wear tracks in the entering side “in” and “middle” region of the tested specimens are displayed in Figure 62. The “in” and “middle” positions within the contact zone are given in Figure 63. According to our observations the dominant wear process occurs in the “in” and “middle” regions.

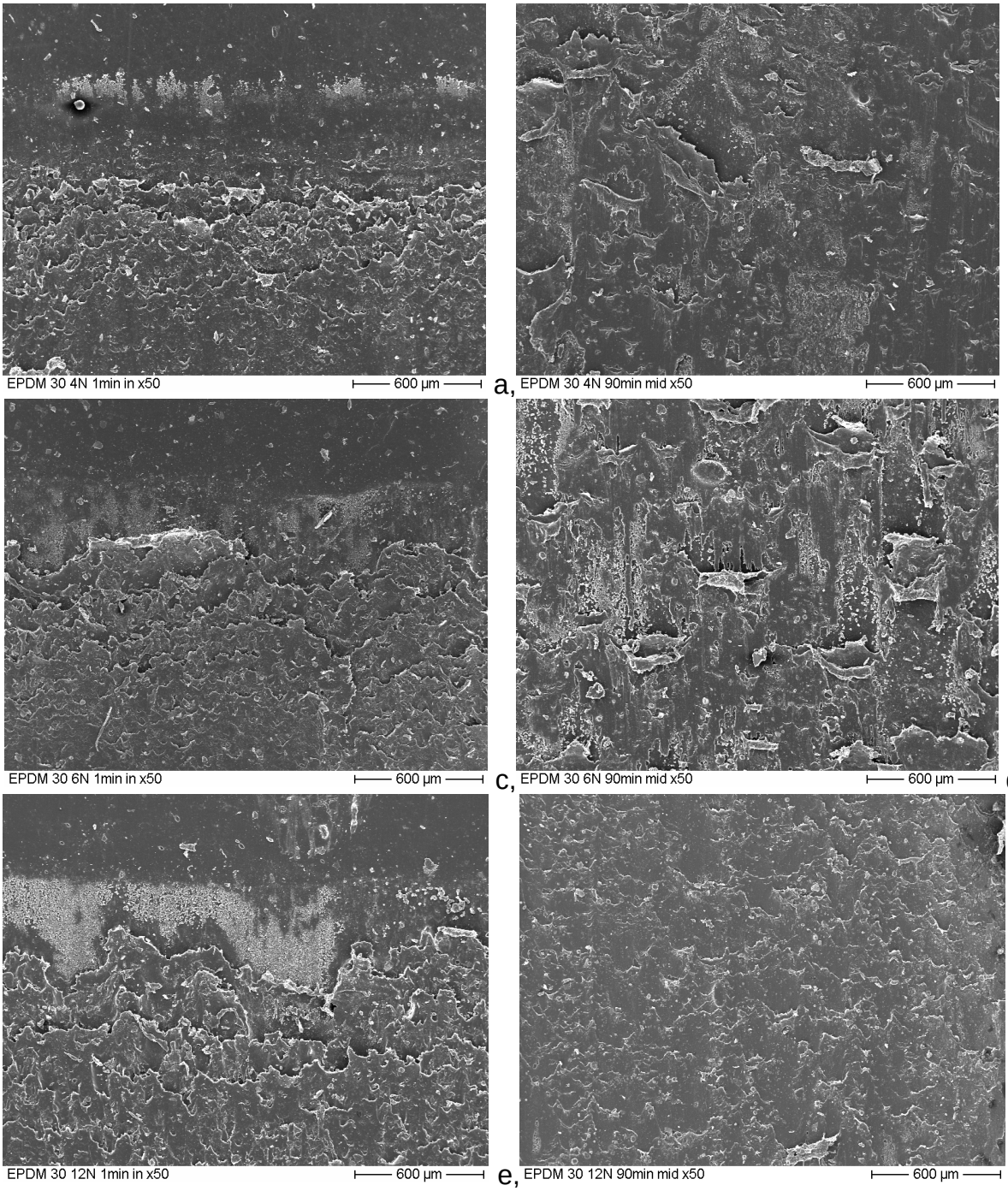

Figure 62: SEM pictures of the wear tracks in different time stages of the ROP tribotests on EPDM 30. Designations: -a; 4N after 1 min “in” -b; 4N 90min “middle” -c; 6N 1 min “in” -d; 6N 90 min “middle” -e; 12N 1 min “in” -f; 12N 90 min “middle”. Note: sliding direction is downward.

In Figure 62-a the worn surface of the EPDM 30 rubber specimen is seen in the “in” region after 1 min testing at 4 N normal load. In this initial stage of wear intensive crack propagation or tearing of the material take place. This scenario changes with the location and testing time (cf. Figure 62-b). Sparsely placed, widely opened cracks are resolved on the surface after 90 min sliding in the middle region. It

is noteworthy that this failure mode becomes characteristic for the overwhelming proportion of the wear track. In accordance with the results in Figure 61, this change in the wear mechanisms suggests reduced wear in the steady-state. In Figure 62-c one can see a wider cracked zone in the “in” region. Probably due to the increased normal load, the cracks penetrate deeper in the elastomer than at lower load. However, with increasing testing time the wear mechanism changes also at 6 N normal load: pronounced wear took place based on the surface appearance in the steady-state stage after 90 min testing (cf. Figure 62-d). Densely placed widely opened cracks are to see on the surface representing significant surface damage. With increasing load (cf. Figure 62-e) the initial surface cracking is further amplified in the “in” region. At 12 N normal load in the steady-state (cf. Figure 62-f), however, moderate surface damage can be resolved in the “middle”-region of the wear track. This suggests a pronounced reduction of the loss volume being in concert with the results showed in Figure 61.

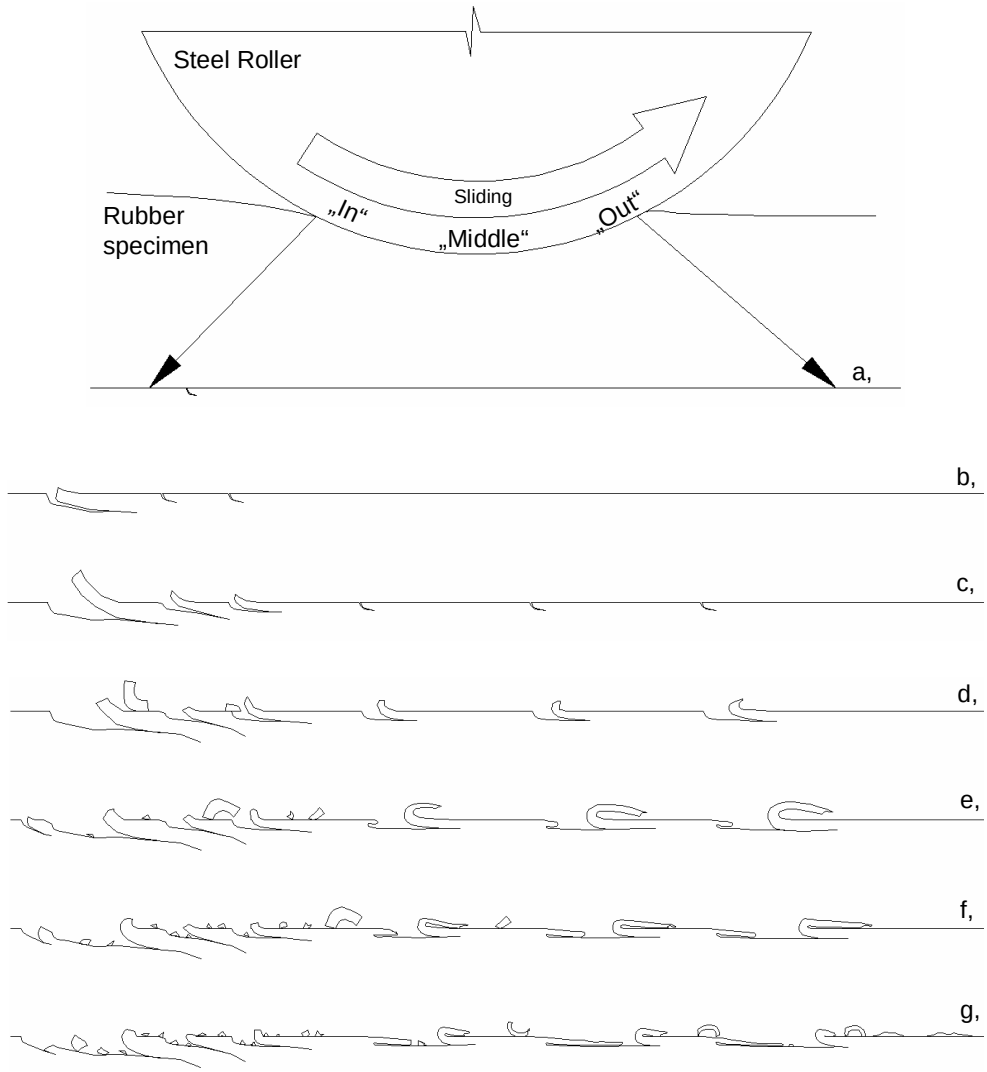

Figure 63: Schematic sketch of the presumed wear mechanism by EPDM 30

As mentioned before, the wear mechanisms differ from one other as a function of the position within the wear track and test duration. The pictures from “a” to “g” in Figure 63 show the wear process during the tribotest. At the beginning, cracks appear in the incoming zone of the contact area (cf. Figure 63 a-b). These cracks penetrate deep into the material, but getting off from the entering side the penetration depth of the cracks decreases. With increasing time rubber tongues form from the cracks and cracking starts in the middle part of the contact area (cf. Figure 63 –c). During the wear process more and more wear particles arise by breaking of the rubber tongues and the cracks in the middle region are growing further (cf. Figure 63 –d). Pictures “e” and “f” in Figure 63 show the appearance of new cracks and the steady “erosion” of the rubber tongues in the entering side, as well as the growth of the cracks in the middle region. In the middle region the direction of the crack growth is parallel to the sliding direction and large plastic deformations develop in both sides of the cracks (left: tension, right: “ironing”). In Figure 63 –g further “eroded” and slowly disappearing rubber tongues are depicted at the entering side and slowly opening cracks in the middle part. At the leaving edge of the contact area a part of the wear particles will be “ironed” onto the surface.

The observed large deformation of the rubber material in the middle zone of the wear track is very important being able to explain the decreasing wear with increasing load. Inspecting the surface of the steel counter-body, a black tribofilm was found on it (see Figure 64 a-d), however only when high normal loads (> 8 N) were applied. Figure 64-a shows a SEM picture of the steel counter surface. At the left side of the picture one can see the neat metal surface (without contact to the elastomer) and at the right side of the picture a rubber “coated” area (having been in the contact with the elastomer). In higher magnifications (Figure 64-b-c) the structure of the rubber “coating” is better resolved. Figure 64-b (magnification x1000) shows a relative thick and coarse rubber layer on the surface which contains rolled wear particles. The higher magnification (x25000) in Figure 64-c shows the base structure of the deposited rubber layer. Here in some places the neat, uncoated metal surface becomes also visible. In Figure 64-d the neat (“uncoated”) metal surface is highlighted by white frames and arrows show the already visible CB particles within the rubber matrix. Figure 64-c demonstrates how smooth the rubber layer is. One may have the impression that the rubber is wetting the metal surface just like a melted polymer. A smooth, continuous rubber surface is to see in Figure 64 c and d.

This phenomenon is extremely unusual considering the fact, that the rubber is fully crosslinked. On the other hand, this explains unequivocally the decrease in the loss volume at higher normal loads. The rubber layer acts, on the one hand, as a lubricant, which decreases the COF (cf. Figure 65). On the other hand, the sliding counter-body surface is no more rigid enough to make serious damages on the surface of the rubber specimen.

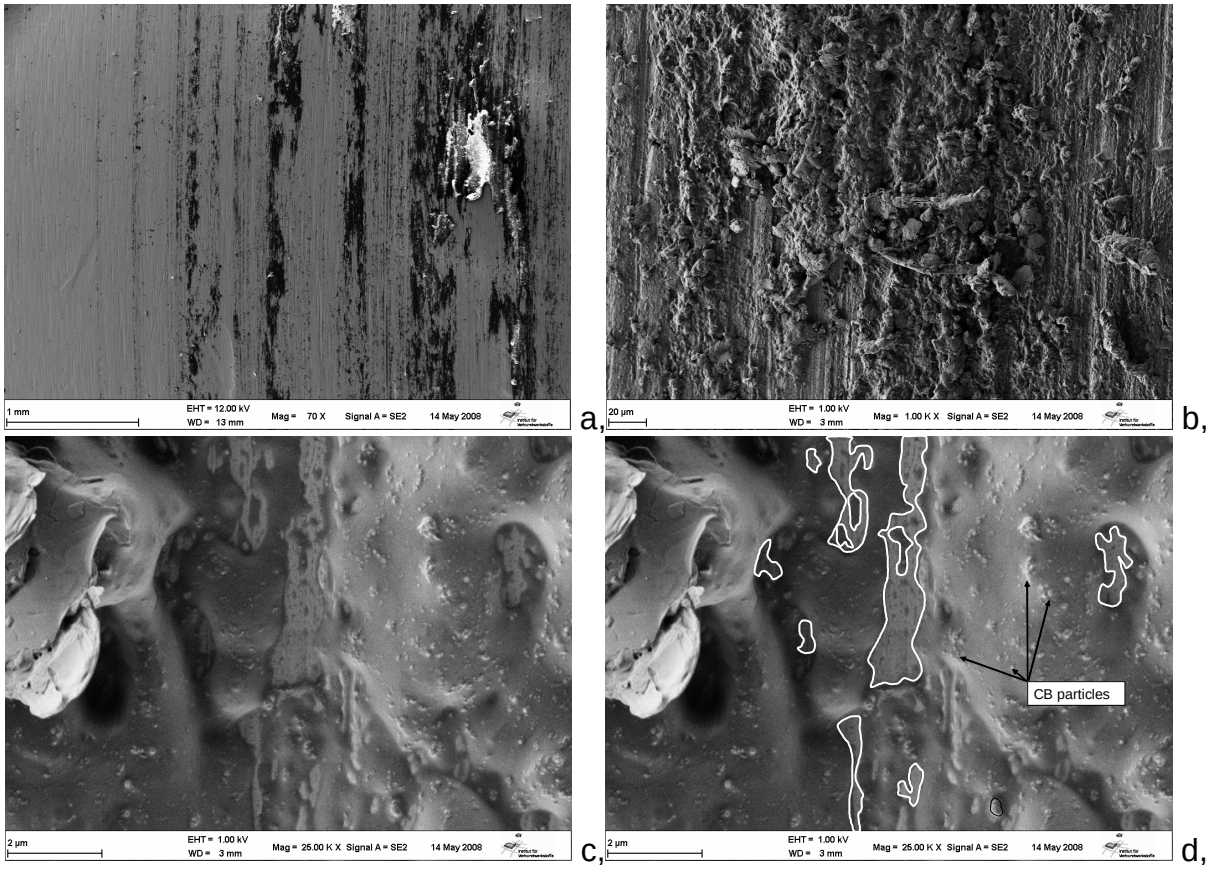

Figure 64: SEM pictures taken from the counter-body surface. a; small magnification of the counter-body surface, b; picture of the deposited rubber layer on the counter body, c; high magnification picture of the deposited rubber layer, d; high magnification picture, highlighting the neat metal surface (framed by white colour) and showing the CB particles (indicated by arrows)

7.5.2 COF

The change of the COF versus testing time and normal load is summarized in Figure 65. Note that extremely high COF values were measured in the running-in phase of the tests. This high initial COF value decreases very fast, probably due to surface damages and due to the larger deformability of the rubber because of the

temperature rise. In the steady-state, the COF increases only slightly in function of the adopted time. With increasing normal load a continuous decrease in the COF occurs in both running-in and steady-state phases. As it was shown before, a relatively thick rubber film formed on the counter-body surface when high normal load (>8 N) is applied. Its effect on the COF is not clear yet. We assume that the permanently deformation of the rubber film increases the friction. The deformations have prominent viscoelastic and plastic proportions, due to the higher pressure and increased temperature (cf. Figure 66), occurring mechanical losses during sliding. On the other hand the rubber film on the counter surface may have a wear protecting effect. This may result fewer cracks in the rubber due to the “softer” counter surface, decreasing that way the COF. The continuously decreasing COF can not account for the shape of the loss volume contour diagram (Figure 61). Recall that the loss volume first increases (until 6 N) and decreases only after further normal load increase above this threshold. This fact underlines the importance of the rubber film formation on the counter surface.

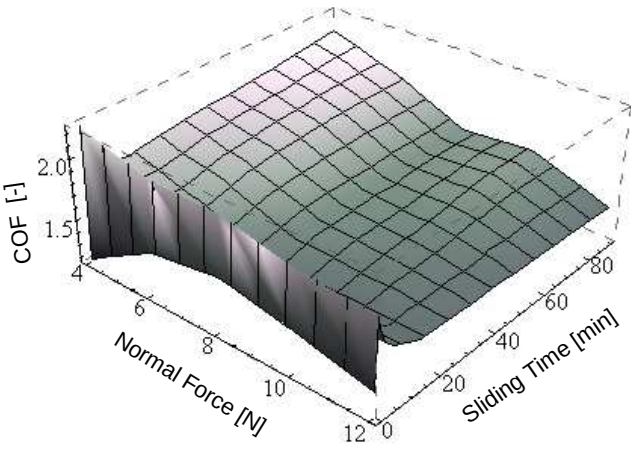

Figure 65: COF change versus the testing time and normal load for the EPDM 30 under ROP testing

7.5.3 Temperature results by EPDM 30

In Figure 66 one can see the measured temperature versus the testing time and applied normal load. A monotonous increase of the temperature can be noticed with increasing normal load. As a function of testing time the temperature first rises very fast in the running-in phase. This warm up process slows down in the steady-state, where an almost constant temperature is reached. Recall that the measured temperature is only the average of the actual flash temperatures in the contact area.

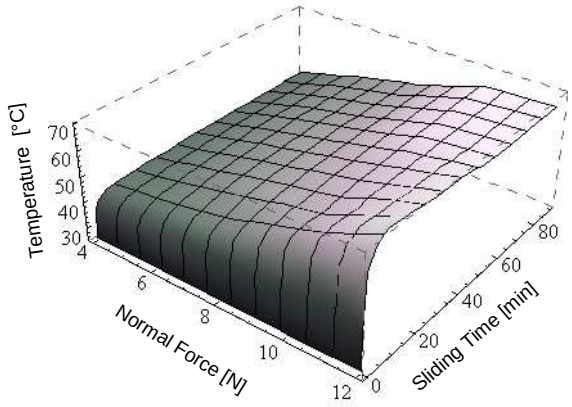

Figure 66: Temperature change versus the testing time and normal load for the EPDM 30 under ROP testing

7.5.4 FE results

The description of the FE models (Chapter 6.8.1) clarifies, that even in this simple tribotest configuration significant simplifications are needed to make reasonable simulations. Unfortunately, in this EPDM 30, a rubber film layer was formed on the counter surface at high load levels (F_N>8N). This fact suggests that the abstraction of the steel roller as a perfectly rigid body, is not fully correct, at least for the simulations considering the highest load level (F_N=12 N). As it was shown before, the rubber film protects the surface of the specimen. It can be assumed that due to these much lower strains and stresses will evolve in the contact area. Considering the presence of the rubber layer on the counter surface at high normal load levels, caution is required with the FE-results in case of 12 N loading (cf. Figure 67-c). The modelled tribotest stages are summarized in Table 7 and the principal stress (σ_1) – contact length results as a function of testing time are depicted in Figure 67-a, -b and –c, respectively.

Table 7: Load cases for FE simulations of the ROP tribotest on EPDM 30

Normal load		**4N**	**6N**	**12N**
Time [min]	Initial phase	0	0	0
	Running-in	10	5	5
	Steady-state	90	90	90

For every load case, the beginning, the running-in phase and the steady-state of the tests were simulated. Comparing the results achieved at three different loads one can see that the highest stresses appear at 12 N normal loading. However, this result

is in contrast with the experimental results, whereby the lowest wear was measured at the highest normal load. The FE results show that with increasing testing time the developed stresses are lower (cf. Figure 67-a and -b). This is in line with the decreasing COFs and with the increasing contact areas due to the increasing wear groove. Only a moderate increase in the largest principal stress values was found between the normal loads at 4 and 6N, respectively. The results at 12 N normal load show far larger stresses in every test stages, but as mentioned before these results are probably false due to the rubber layer on the counter body.

Further comments and explanations related to the FE simulations (designations and theory) are summarized in Appendix 1 (chapter 11.1).

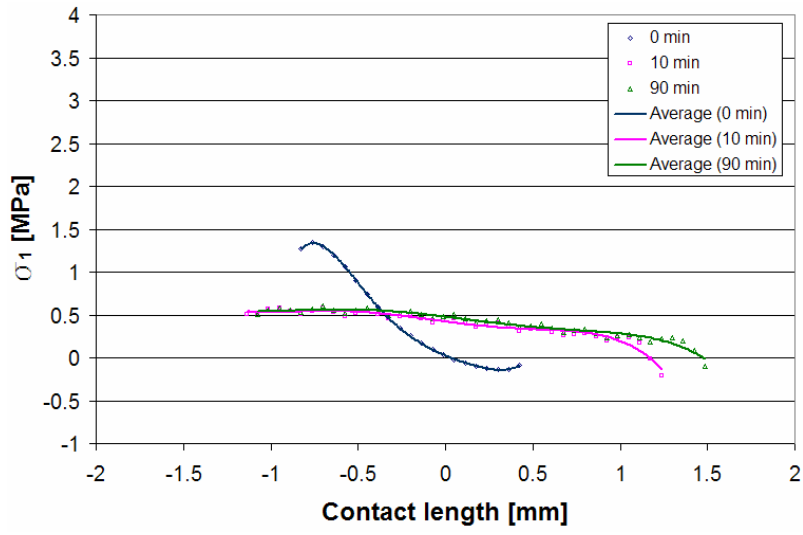

a,

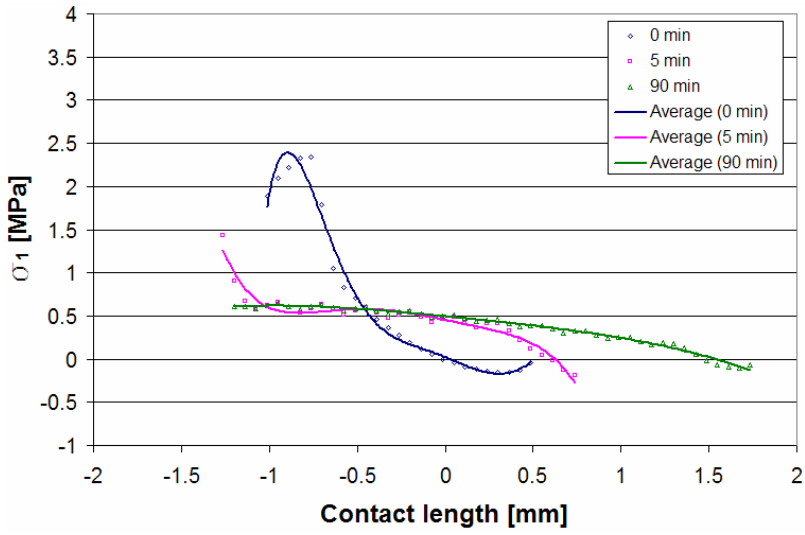

b,

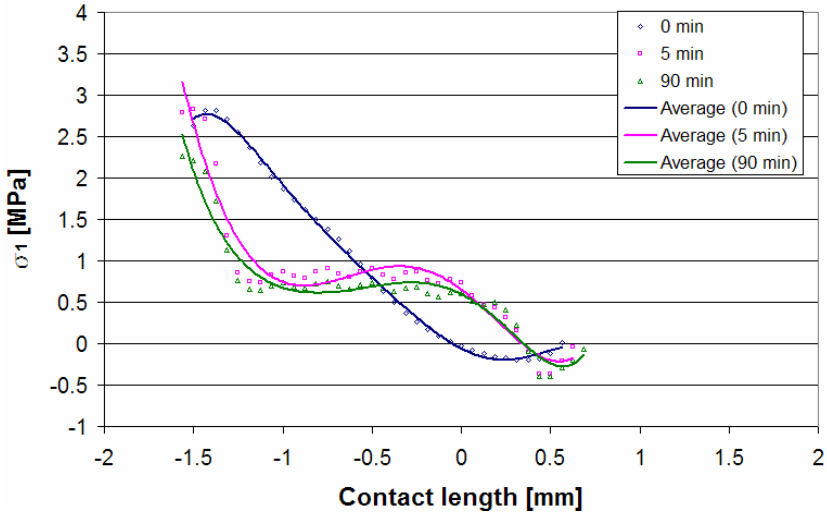

c,

Figure 67: σ_1 – (largest principal stress) distributions along the contact length as a function of testing time, for three different normal loads: –a; 4N –b; 6N –c; 12N. Notes: the entering “In” side of the contact region is represented in the negative range of the contact length, the sliding direction shows right.

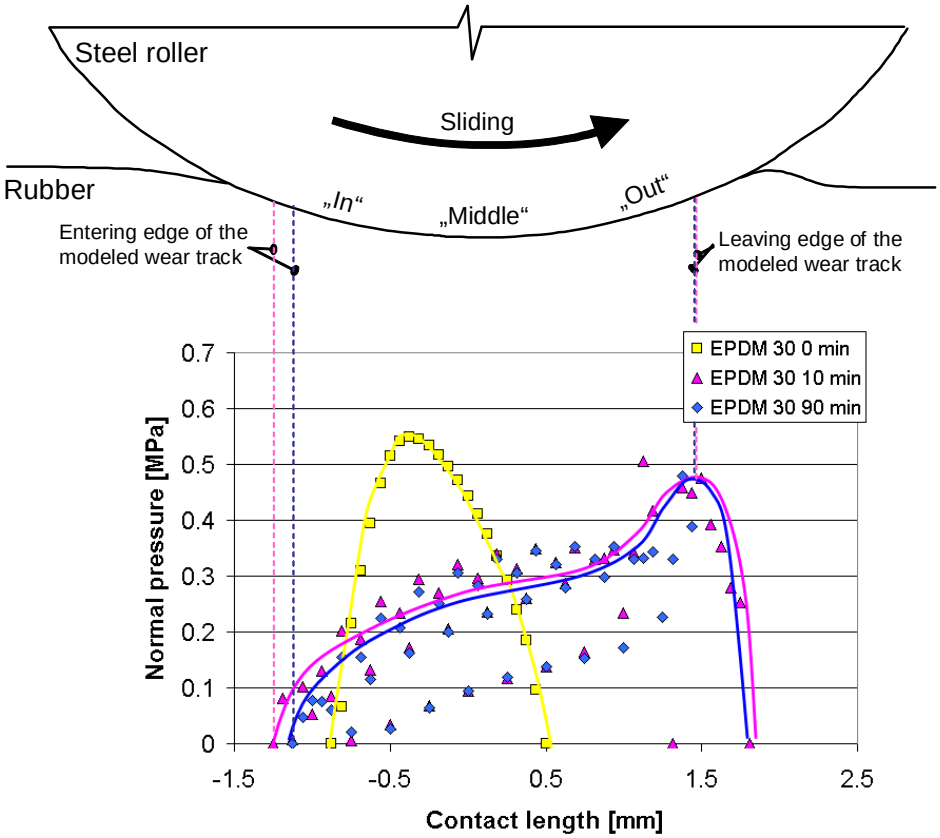

Figure 68: Normal pressure distributions (FE results) for EPDM 30 under 4 N normal load, along the contact length, for three different time stages: initiation (0-min), running-in (10 min), steady-state (90 min)

In Figure 68 the schematic sketch of the contact situation with the “In”, “Middle” and “Out” regions, as well as the normal pressure distributions for different testing times for the EPDM 30 material is illustrated. Dashed lines show the entering and the leaving edges of the contact region. In order to demonstrate the normal pressure distribution in the contact area, the FE results with the lowest applied normal load (4 N) were selected. In the diagram the yellow curve represents the normal pressure distribution at the beginning of the tribotests, without any wear on the surface. Minor distortion can be observed due to the tangential (frictional) stresses. For the running-in phase (10 min) and for the steady-state (90 min), normal stress peaks can be observed at the leaving edge of the wear track. The maximum of the normal stresses is lower for the running-in phase and in the steady-state than for the initiation-phase. Due to the same conditions, (similar coefficient of friction and minor change in the wear track) the courses of the normal stress distributions for the running-in phase and for the steady-state are very similar. Regarding the normal stress peaks at the ”Out” region the leaving edge of the simulated wear tracks is inside the contact area.

7.6 Results on the EPDM 45

7.6.1 Wear and wear mechanism

In Figure 69 the loss volume results versus the normal load and sliding time, achieved on the 45 phr CB containing EPDM rubber, are summarized. The contour surface, in some aspects differs from the previous ones (cf. Figure 52 and Figure 61). The running-in phase of the tests is longer in this case (>10 min) and negligible wear occurs after reaching the steady-state. The loss volume is also much smaller as it was for the EPDM 0 and EPM 30 rubbers. Interesting finding also in this case, that after a threshold load value (> 6N) the wear (loss volume) decreases with increasing normal load. Unlike to EPDM 30, the peculiar feature with EPDM 45 is that both WLP and SEM techniques failed to detect a rubber film on the steel counter body. It should be born in mind that tribotest results are often undergoing a very large scatter because of vibrations during testing. However, the resulting tendencies were justified by parallel tests performed on minimum 5 specimens. The results in Figure 69 show that the maxima of the loss volumes are at about 1-1.5 mm^3.

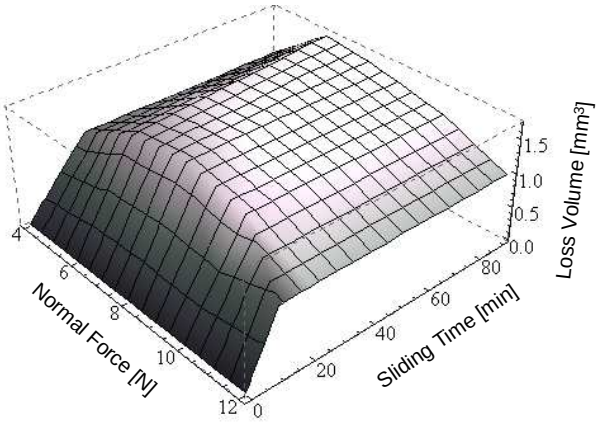

Figure 69: Loss Volume results versus the testing time and normal load for EPDM 45 under ROP conditions

SEM investigation of the worn surfaces yields interesting observations (cf. Figure 70 a-f). The related pictures highlight the large deformability of the CB filled rubber material. Further interesting recognition is the radical change in the wear mechanisms during the ROP tests. In Figure 70-a the surface of the wear track after 1 min testing time at 4 N normal load is shown. Notable material failure is to observe in the middle part of the wear track, where significant crack propagation happens. The wear situation changes radically in the steady-state (cf. Figure 70-b). Instead of the typical “combing”, “wavy” surface structure with retroflected rubber tongues, extremely tensioned rubber segments can be resolved on the surface. A similar

change in the wear mechanisms is to observe at 8 N normal load (cf. Figure 70 c-d). In Figure 70-c after 1 min testing time in the running-in phase significant crack propagation occurs. The change in the worn surface structure becomes obvious when comparing Figure 70-c and –d. The latter is characterized by a smoothed surface with moderately opened cracks. With further increase of the normal load the wear track become heavily cracked (cf. Figure 70-e). However the change of the wear situation between the running-in and steady state stages is also unambiguous. At the highest normal load the surface structure in the steady state seems to be less distorted as it was at lower normal loads (cf. Figure 70-f with Figure 70-b and -d). Albeit the surface is smooth, the “combing wave” structure is recognizable. This wavy structure seems to be stabilized. In the surface no crack opening but highly tensioned rubber segments are seen. Though the surface structure is changing, but only a marginal wear is detectable during the ROP test under steady-state condition.

The characteristic wear mechanisms observed by EPDM 45 are similar to the wear mechanisms shown by EPDM 30 (cf. Figure 63). In this case we can again assume that increasing temperature and increasing normal load (hydrostatic stresses) contribute to an easier deformability of the rubber (see Figure 72). As mentioned before the changing deformability of the rubber may lead to decreasing COF and finally to decreasing loss volume. That way an important correlation between the COF and wear can be established, at least in case of identical materials and test-parameters.

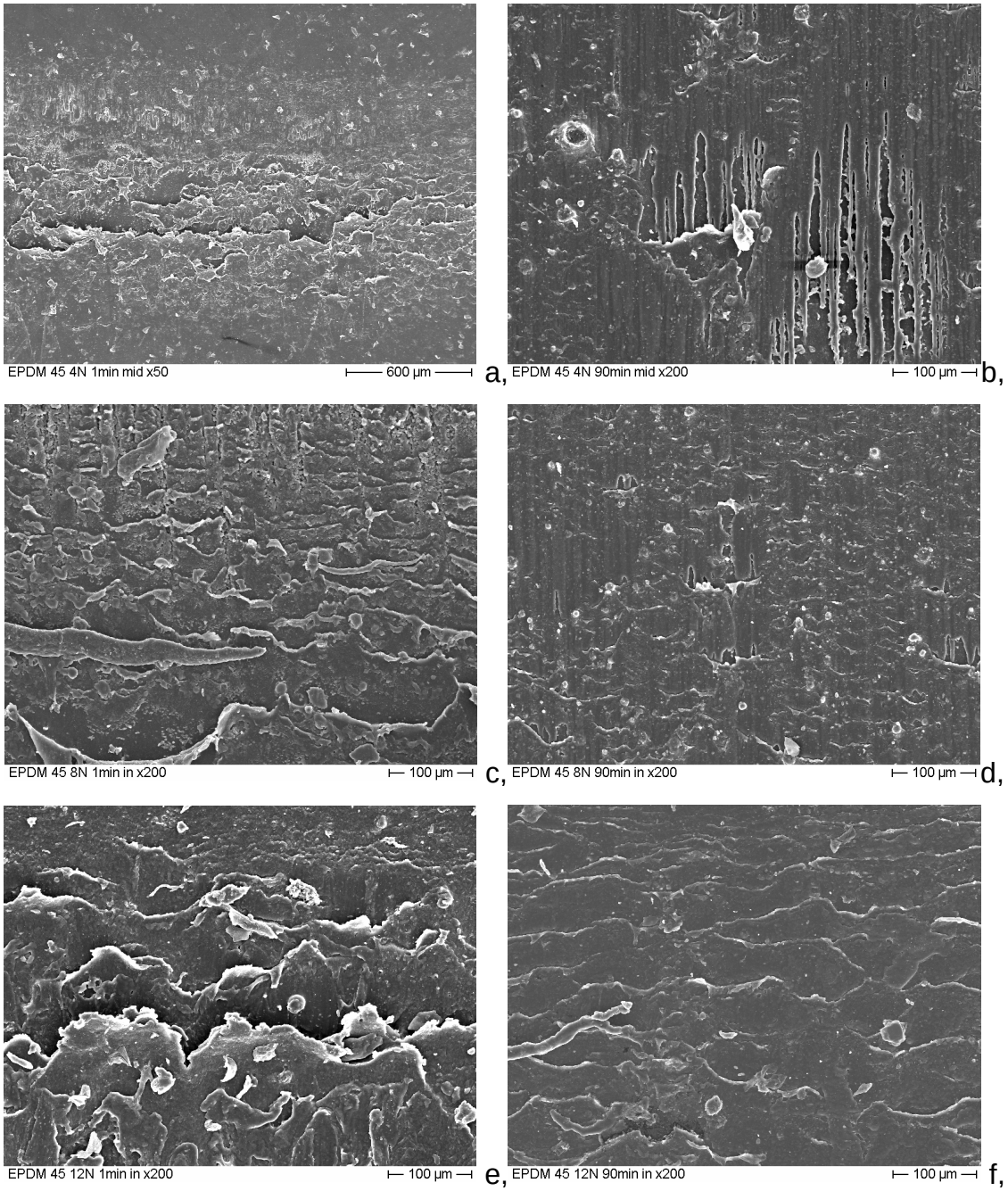

Figure 70: SEM pictures of the wear tracks in different time stages of the ROP tribotests on EPDM 45. Designations: -a; 4N after 1 min “middle” -b; 4N 90min “middle” -c; 8N 1 min “in” -d; 8N 90 min “in” -e; 12N 1 min “in” -f; 12N 90 min “in”. Note: sliding direction is downward.

7.6.2 Coefficient of Friction (COF)

The shape of the COF - normal force – sliding time diagram seems to be similar to that one of the loss volume - normal force – sliding time results (cf. Figure 69). The highest COF was measured of around 6 -8 N normal load. Again extremely high COF values were detected at the beginning of the tests which was followed by a

steep decrease in the COF values even in the running-in phase. The initial COF values are slightly increasing until 8 N normal load, but with further load increase the COF decreases again. After the running-in phase with increasing testing time a slightly increase in the COF can be observed.

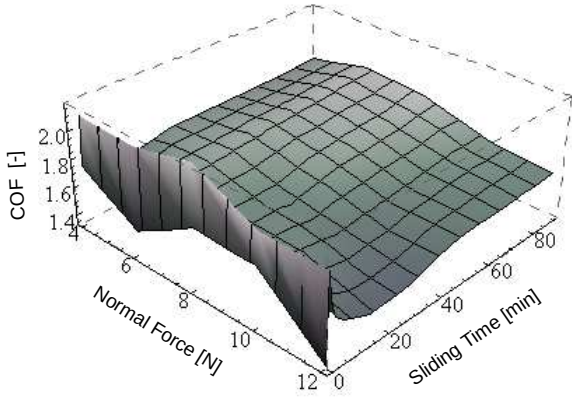

Figure 71: COF change versus the testing time and normal load for the EPDM 45 under ROP testing

7.6.3 Temperature development

Like by EPDM 0 or EPDM 30, the temperature increases with increasing normal load, as well as with increasing testing time, also for the EPDM 45 (cf. Figure 72). The fastest temperature increase is to see at the beginning of the tests. These results match perfectly with the expectation. Nevertheless, one should pay more attention to the energy balance of the tribotest. It is utmost interesting that in the beginning fast wear, high COF and steep temperature increase were found for every investigated material. In depth investigation of the above phenomena may provide an answer for the important question: which is the key factor of the dry sliding process, the COF, the temperature or the wear?

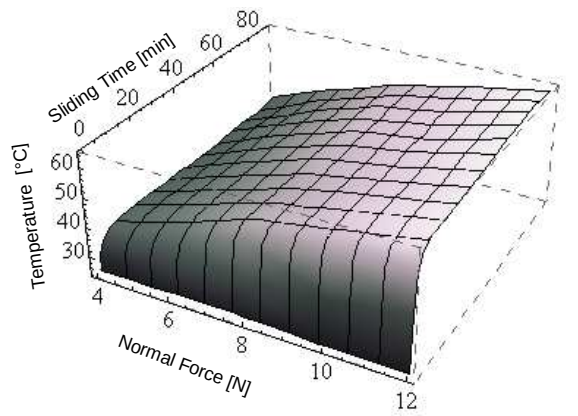

Figure 72: Temperature change versus the testing time and normal load for the EPDM 45 under ROP testing

7.6.4 FE results

In Figure 73 one can see the FE simulation results of the tribotests for the EPDM 45 material. In Figure 73-a the principal stress (σ_1) results are depicted for the beginning of the tests, where the rubber specimens are not yet damaged and very high COF appears (cf. Figure 71). The "x" axis shows the actual positions in the contact region where the zero means the geometrical middle point of the rubber specimen (see Appendix 1 in chapter 11.1). The modelled test stages are summarized in Table 8.

Table 8: Load cases for FE simulations of the ROP tribotest on EPDM 45

Normal load		**4N**	**8N**	**12N**
Time [min]	Initial phase	0	0	0
	Running-in	10	10	10
	Steady-state	90	90	90

Figure 73-a informs us, that the largest principal stress evolves at the highest normal load (12 N) at the entering side of the contact zone. This result is in agreement with SEM observations, convoluting that the initiation of cracks starts also in the entering side of the contact area (cf. Figure 70). Comparing the FE results in the different test stages (cf. Figure 70 a, b and c) one can notice, that the highest stresses are found for the rubber specimens at the beginning of the tests. This is again in line with the test results, namely the fastest wear is observed in the initial phase of the tests, probably caused by the high stresses. The change in the wear mechanisms during the tests time can be also deduced from the FE results. Figure 73-b and –c show that smaller stresses develop due to the enlarged wear track, as well as due to the reduced COF. The larger is the wear track the smaller the stress on the rubber surface is. According to the FE modelling of the tribotest no significant increase in the principal stress happen with increasing normal load. Figure 73-b and –c demonstrate further that the stress distributions over the contact length are slightly different for the 8- and 12 N normal loads, but the stress values are fairly matched with each other. No further increase in the σ_1-stress values was observed when modelling the highest (12 N) normal load. It means that the wear does not increase with increasing load as the COF decreases. The decreasing wear may be the reason of collateral effects, just like the already mentioned material property changes due to increasing hydrostatic stresses and temperatures. Further comments and explanations related

to the FE simulations (designations and theory) are summarized in Appendix 1 (chapter 11.1).

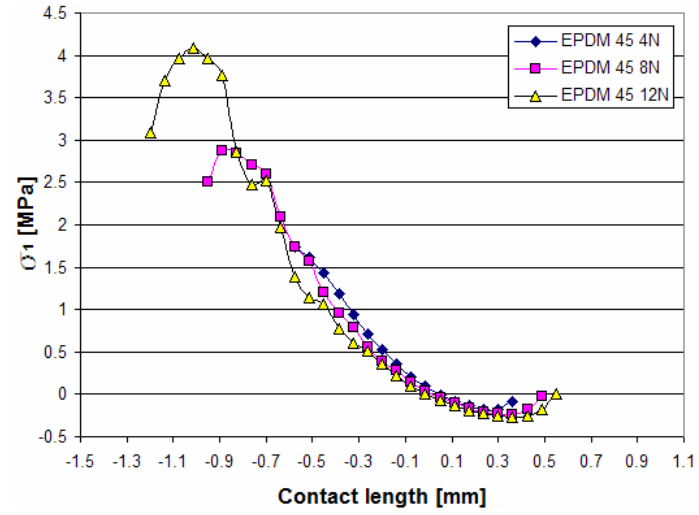

a,

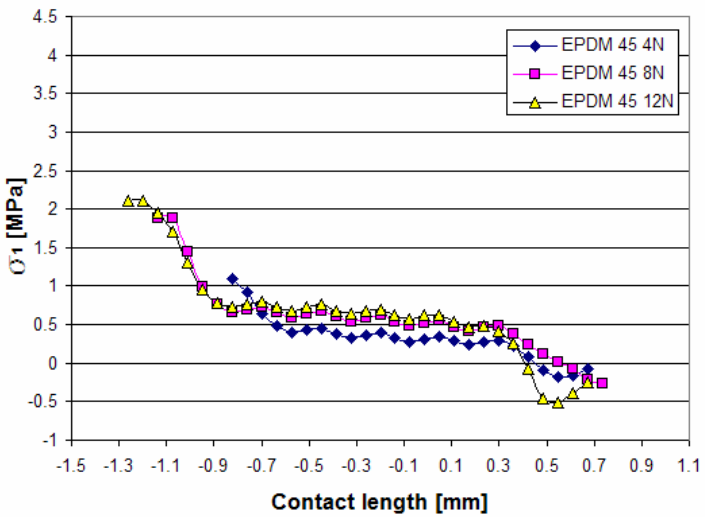

b,

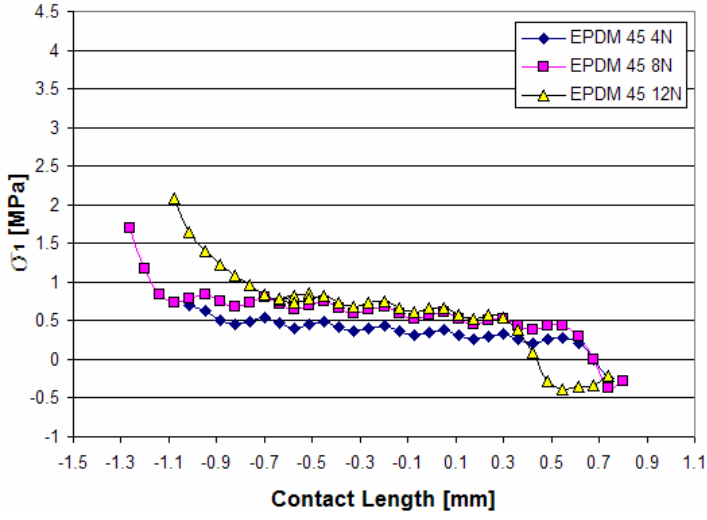

c,

Figure 73: σ_1 – (largest principal stress) distributions along the contact length as a function of normal loads, for three different time stages: a; 0-min, b; running-in, c; steady-state. Notes: the entering “In” side of the contact region is represented in the negative range of the contact length, the sliding direction shows right.

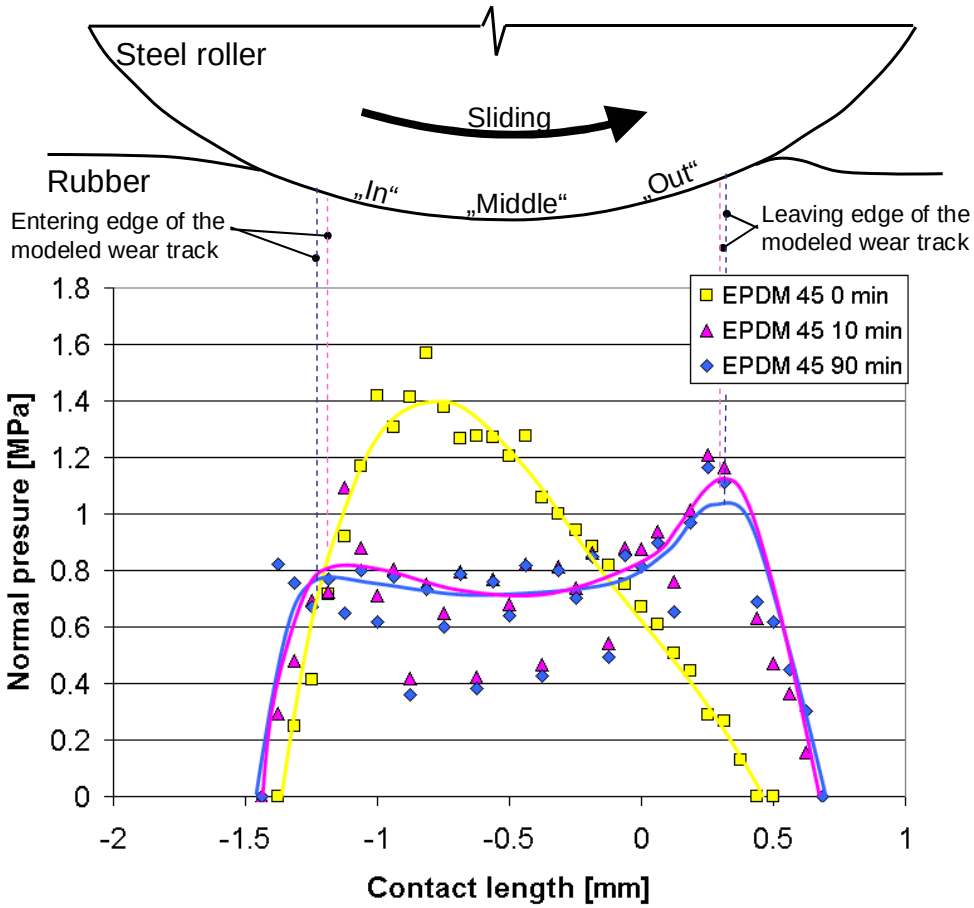

Figure 74: Normal pressure distributions (FE results) for EPDM 45 under 12 N normal load, along the contact length, for three different time stages: initiation (0-min), running-in (10 min), steady-state (90 min)

In Figure 74 the schematic sketch of the contact situation showing the “In”, “Middle” and “Out” contact regions, as well as the normal pressure distributions for the EPDM 45 material is illustrated. The FE results of the highest normal load (12 N) were selected. The yellow curve represents the normal pressure distribution at the beginning of the tribotests (0 min). A determined distortion of the normal pressure distribution can be observed due to the tangential (frictional) stresses. For the running-in phase (10 min) and for the steady-state (90 min), normal stress peaks at the entering “In” and at the leaving “Out” edges of the wear track can be observed. In the FE-calculated normal stress distributions for 10- and 90-min testing times local peaks are formed at the “In” and “Out” regions due to the fact that the modelled wear grooves are shorter than the contact length. The similar coefficient of friction and the minor change in the size of the wear track results in similar normal stress distributions for the running-in phase and for the steady-state.

7.7 Results on the EPDM 60

7.7.1 Wear and wear mechanism

Figure 75 shows the loss volume results for the EPDM 60 material versus the normal load and sliding time. Corresponding to the expectation, a running-in and a steady-state phase of the wear process are to observe at every normal load. The time of the running-in phase was reduced by increasing normal load. This may be traced to increasing stresses in the contact region with increasing normal load.

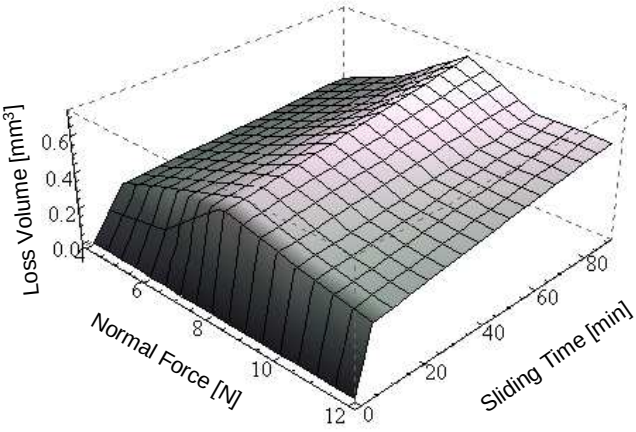

Figure 75: Loss Volume results versus the testing time and normal load for EPDM 60 under ROP conditions

As it was observed for the other CB containing EPDMs, with increasing normal load, above a threshold value, the measurable loss volume decreases. This is also the case here. For the EPDM 60 just for the EPDM 45 no significant rubber deposition could be deduced on the counter body. Recall that this is opposed with the finding with EDPM 30 (cf. Figure 64). In absence of transfer film deposition on the counter surface a complex stress-temperature interaction may be the reason for the loss volume decrease when passing the normal load threshold at 8 N. Though the most likely interplay between stress state and temperature is unknown, the characteristic marks of such an unusual wear mechanism can be found in Figure 76 a-f. In Figure 76 a, c, and e one can see the worn surfaces of rubber specimens in the middle region after 1 min sliding at 4, 8 and 12 N normal loads, respectively. In Figure 76 b, d, and f the worn surfaces after 10 min sliding time are depicted at the same normal loads. The 1 min duration test represents the running-in phase of the tribotest, while the SEM pictures taken after 10 min testing time inform us about the steady state processes during dry sliding. In Figure 76-a the surface structure after 1

min testing at 4 N load is displayed. The surface is smooth and a crack opening process (described in chapter 7.5.1) seems to be dominant. This situation changes with time see Figure 76-b, and a combing wave-like structure appears on the surface. This observation is in accord with the data in Figure 75 at 4 N normal load, where a relatively long running-in phase can be deduced. This explains the slight surface damage after 1 min testing. With increasing normal load the running-in phase of the ROP tribotest becomes shorter and after 1 min testing time the “combing”, “wave”-like structure is already present, cf. Figure 76 c and e. A significant surface damage occurs when 8 N normal load was applied during the tribotest (compare Figure 76 c and e). Moreover, in the steady state of the tribotests after 10 minutes testing a difference between the two load levels (8 and 12 N) is still observable (cf. Figure 76 d and f). One can get the feeling that the characteristic combing waves become more smoothed in the steady state when higher normal load is applied. This is the right place to call the attention for two interesting phenomena. Both of these phenomena are well observable in all of the pictures in Figure 76. The first is a “self-healing” effect of the rubber. At the retroflected side of the combing waves, the rubber material comes in contact with itself (see Figure 77). During dry sliding the surface roughness peaks of the counterpart produce locally large compressions, whereby the actual normal pressure may be considerably higher then the average surface normal stress. This high compression, combined with increased temperature may cause a permanent adhesion of the compressed rubber parts. It is most probable, that the large number of CB particles play a significant role in this process, as they have a respectable surface free energy. Furthermore, molecular diffusion can also occur because these rubber parts are compressed together for long enough. The adhesion between the rubber substrate and the retroflecting tongue can be strong enough to create a permanent upper coating layer in the contact region. This “self-healing” effect is recognizable everywhere where the combing waves or rubber tongues seem to be fixed in their deformed positions. The second unusual phenomenon which was observed also for EPDM 30 and EPDM 45, is that large, irreversible deformation took place on the surface (cf. the pictures in Figure 76 –c and -e). A remarkable irreversible (plastic) deformation is not typical for rubber materials. The orientation plastic deformation agrees with that of the sliding. Without irreversible deformation, after removing the counterpart, the rubber tongues should move back into their original positions more or less. The yielding or flow of the rubber material is possible

as it was shown in chapter 7.1 in respect with the uniaxial compression tests of the EPDM elastomers. Therefore effect of increasing temperature on the deformability of the filled EPDMs should be subjected of studies.

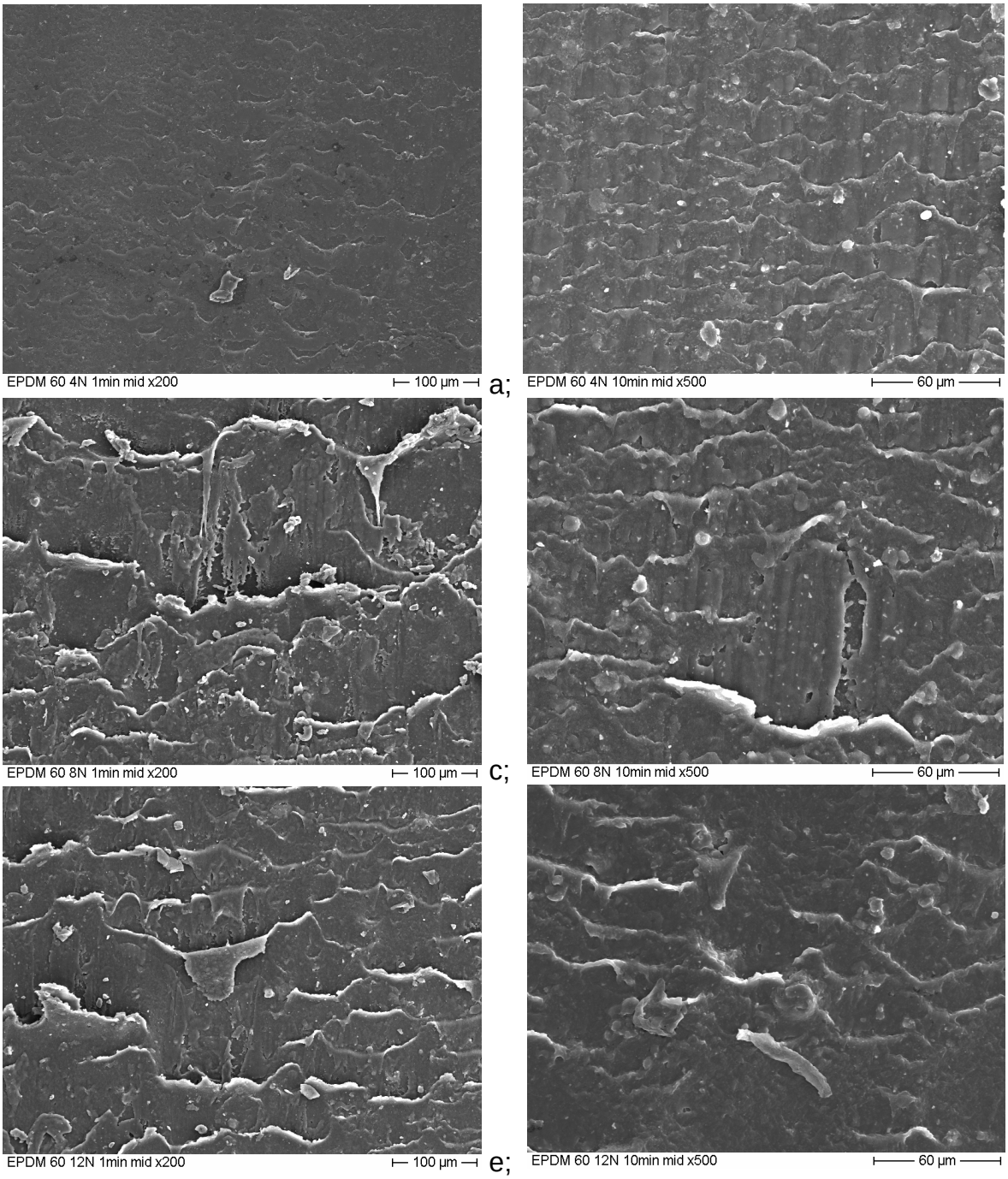

Figure 76: SEM pictures of the wear tracks in different time stages of the ROP tribotests on EPDM 60. Designations: -a; 4N after 1 min “middle” -b; 4N 10min “middle” -c; 8N 1 min “middle” -d; 8N 10 min “middle” -e; 12N 1 min “middle” -f; 12N 10 min “middle”. Note: sliding direction is downward.

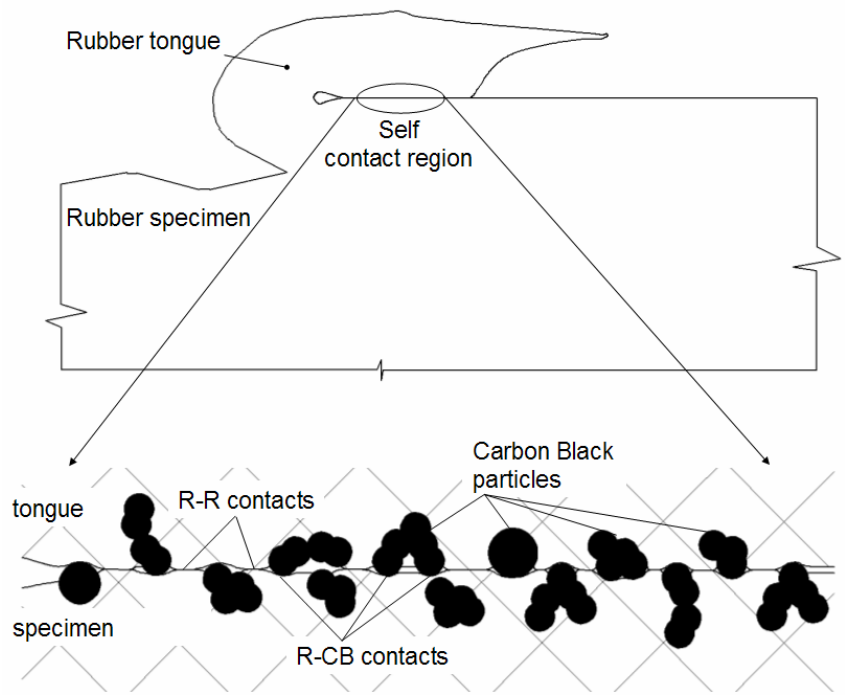

Figure 77: Schematic sketch of the rubber-rubber adhesion process causing “self healing”

The process of the presumed wear mechanisms is depicted schematically in Figure 78. We assume that the first cracks initiate at the middle region of the contact area (cf. Figure 78–a). Later cracks appear also at the entering (“in”) and leaving sides (“out”) of the contact zone (cf. Figure 78–b). These cracks grow first downwards (into the depth), later parallel to the surface in the sliding direction (cf. Figure 78–c). With the parallel extension of the cracks the prerequisites of the combing waviness pattern long with formation of rubber tongues are given (cf. Figure 78–d). These rubber tongues owing to self contact will stick to the worn surface of the rubber it was discussed before (cf. Figure 78–e). Afterwards, limited crack tip opening and wear take place. Due to the increasing temperature and to the constantly acting tangential stresses the stacked rubber tongues become “ironed”. This results in tension-type irreversible deformation (cf. Figure 78-f and -g). In the last picture in Figure 78-h, the shaded part of the rubber tongues means that an upper layer has been formed on the rubber surface. This is adhered to the base material. This partly melted, oriented layer ensures a protecting layer against wear (the wear particles can “glue” again to the surface) in addition this layer acts also as a kind of lubricant film and thus decrease the COF.

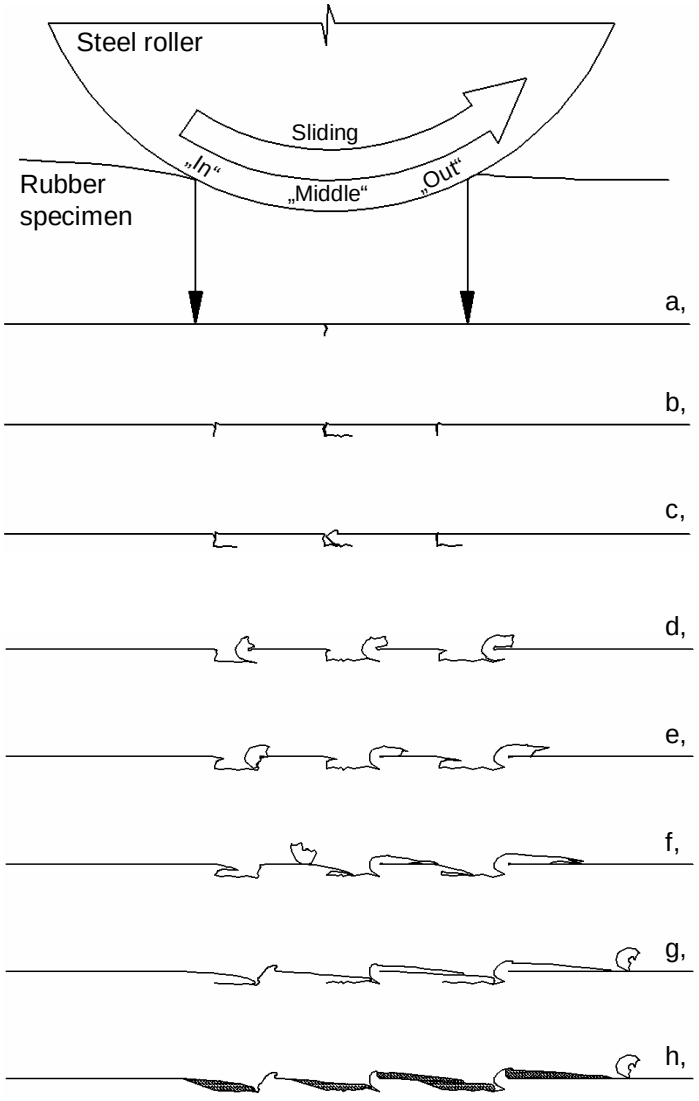

Figure 78: Schematic sketch of the presumed wear mechanisms in EPDM 60

7.7.2 Coefficient of Friction (COF)

The lubrication effect of this easily deformable upper layer is also reflected by COF results (see Figure 79). In Figure 79 one can see, that similar to the loss volume data in Figure 75 the COF plotted against the normal load and testing time reaches a maximum at a threshold normal load range (8 N). The COF values in the running-in phase are extremely high at each normal load selected.

This high value decreases of COF very fast with the testing time. The reason for this reduction may be the temperature increase (cf. Figure 80) and the beginning damage of the original surface. However, the temperature rise enhances the adhesion capability of the rubber chain molecules because their mobility is highly enhanced. The increasing deformability of the rubber with increasing temperature

seems to be the dominant effect. Further on, the damage of the initial surface structure can lead to a decrease of the real contact surface owing to appearing cracks and wear debris. Their effect may balance the enhanced adhesion of the rubber molecules. After the running-in phase no further significant temperature rise can be detected (cf. Figure 80). It suggests that later in the steady-state (with increasing testing time) the change in the COF value is controlled by the change of the contact geometry. As shown in Figure 75 the most severe wear (or largest increase in the contact surface) happens at 8 N normal load. This increase in contact geometry may increase the adhesion component of the friction which finally increases the COF. On the other hand, crack propagation may account for significant energy dissipation.

Observing the COF data from the view point of the normal load, at the beginning the COF increases with increasing normal load. Reaching a threshold normal load value (8 N) the COF does not increase further. After the threshold normal load value the COF tends to decrease. This behavior is due to the interplay of several effects what should be considered. One of them is the increasing contact surface with increasing normal load and with increasing testing time. This enhances the COF and wear until the threshold normal load value because of prominent adhesion effects. On the other hand, with increasing normal load the permanently acting stresses at the rubber surface also increase. This along with the increasing temperature (cf. Figure 80) supports the deformability of the rubber. The easy deformability means some kind of lubrication (reducing the apparent asperity) which reduces both the COF and loss volume.

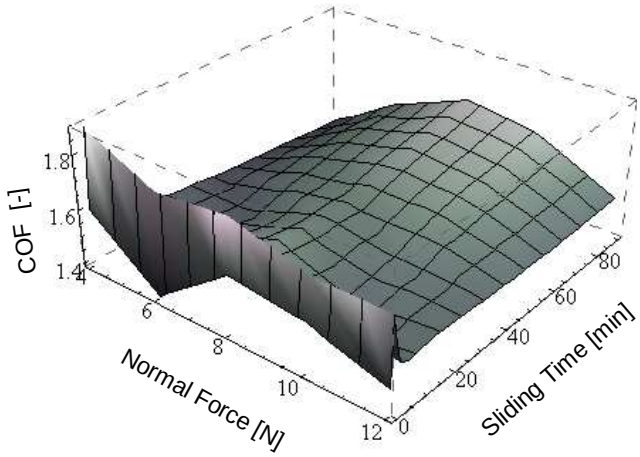

Figure 79: COF change versus the testing time and normal load for the EPDM 60 under ROP testing

7.7.3 Temperature development

As expected the temperature increases with increasing testing time and increasing normal load. The temperature increase is very fast in the running-in phase of the tests and slows down in the steady state phase. The fast warming up seems to be in correlation with the high running-in COF values (cf. Figure 79). In Figure 80 no local temperature maximum can be found measured at 8 N normal load opposed the loss volume and COF values in Figure 75 and Figure 79. The measured maximum temperature (60℃ -63℃) seems to be not extremely high. On the other hand one needs to keep in mind that this temperature is the averaged one and the flash temperatures occurring in micro and nano-levels may be higher.

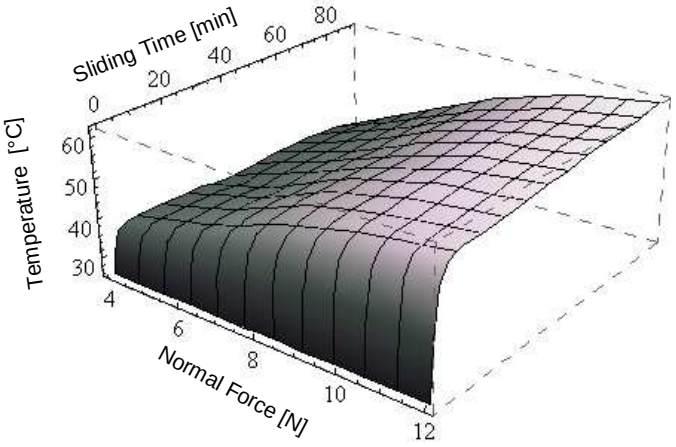

Figure 80: Temperature change versus the testing time and normal load for the EPDM 60 under ROP testing

7.7.4 FE simulation results

For the FE simulation the geometry of the rubber specimens and COF, both changing with progressing wear were taken into consideration. The simulated load situations are summarized in Table 9. Figure 81 shows the normal pressure distribution in the contact zone, in Figure 82 a-c the maximum principal stress (σ_1) results are depicted along the contact region.

Table 9: Load cases for Fe simulations of the tribotest by EPDM 60

Normal load		**4N**	**8N**	**12N**
Time [min]	Initial phase	0	0	0
	Running-in	10	5	5
	Steady-state	90	90	90

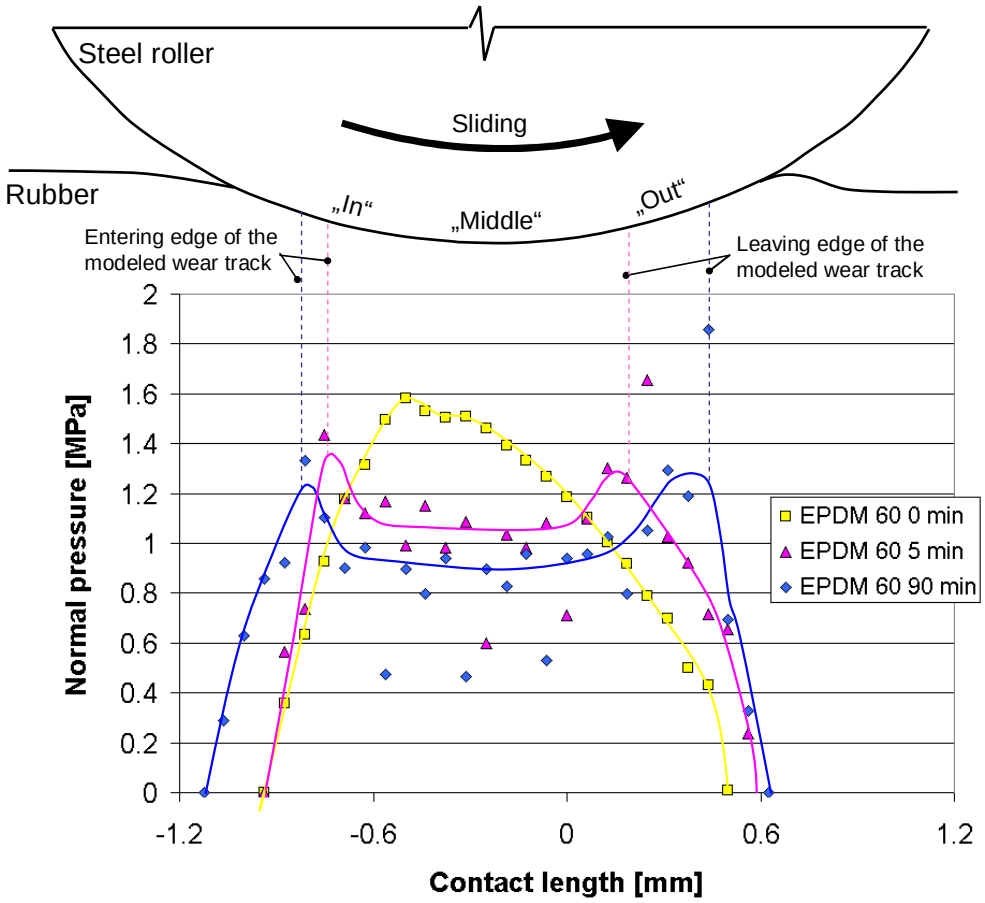

Figure 81: Normal pressure distributions (FE results) for EPDM 60 under 12 N normal load, along the contact length, for three different time stages: initiation (0-min), running-in (5 min), steady-state (90 min)

The schematic sketch in the diagram in Figure 81, shows the positions of the entering- (“In”) and of the leaving-edges (“Out”) in the contact region for the EPDM 60 material. The yellow curve represents the normal pressure distribution at the beginning of the tribotests, without any wear on the surface. The typical symmetric Hertzian type normal pressure distribution is distorted due to the high tangential (frictional) stresses. When the wear groove appears at the surface (running-in and steady-state) the highest normal pressures are observed at both (entering and leaving) edges of the modelled wear tracks (see purple and blue curves in Figure 81). i.e. the FE- calculated contact area is wider than the width of the modelled wear track. At the middle of the contact area the normal pressure is decreased due to the bended contour of the wear groove. Regarding these results it is supposed, that with increasing testing time less wear can be observed on the specimen. The highest wear will occur at the edges of the wear track, i.e. the wear groove will be extended horizontally.

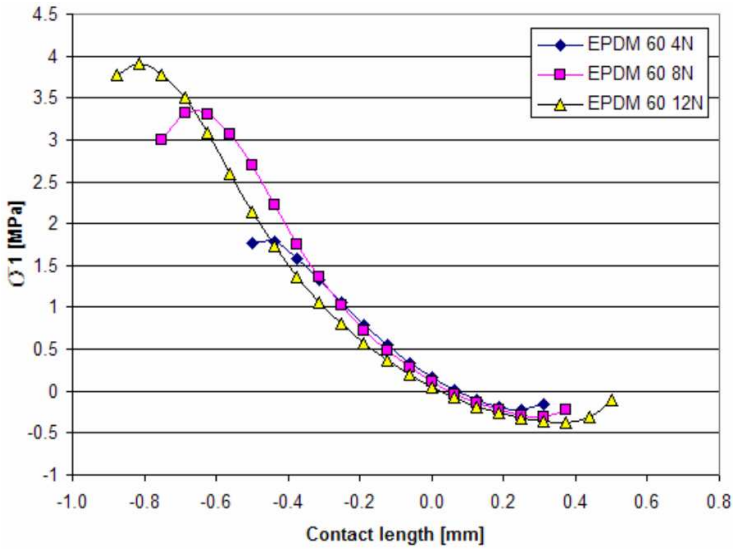

a,

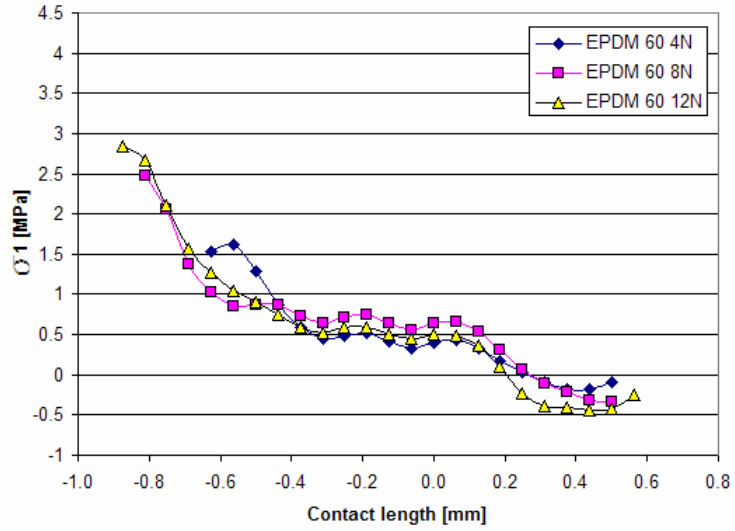

b,

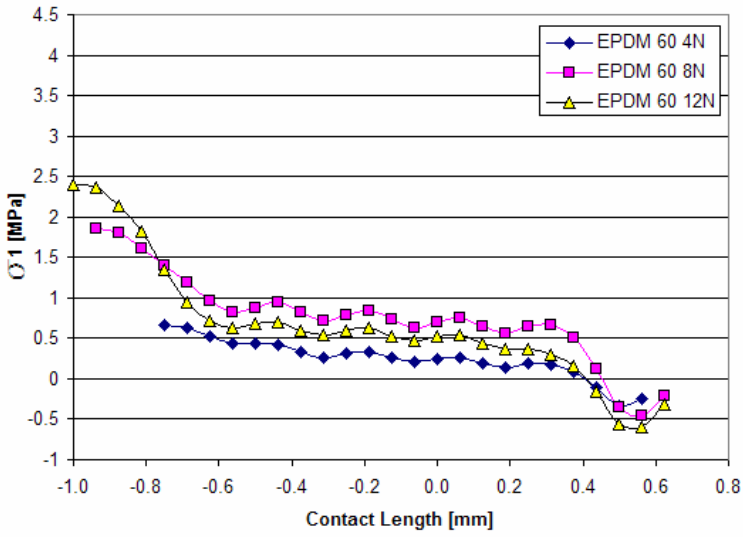

c,

Figure 82: σ_1 – (largest principal stress) distributions along the contact length as a function of normal loads, for three different time stages: a; 0-min, b; running-in, c; steady-state. Notes: the entering “In” side of the contact region is represented in the negative range of the contact length, the sliding direction shows right.

The positive and negative values of the stress results correspond to tension and compression, respectively. To choose the maximum principal stress for failure analysis is usual thus this stress being the largest one stress value occurs the damage of the material. The results in Figure 82-a correspond to the contact of perfectly smooth non worn bodies in the 0-th moment of the tests. Figure 82-b represents the contact situations (in the running-in) after 10, 5 and 5 min testing times by 4, 8 and 12 N normal loads, respectively.

In Figure 82-c the simulation results after 90 min testing are represented. The zero point of the “x” axes means the symmetric middle point of the rubber specimen. The sliding direction is to the right. In Figure 82-a one can see that the maximum σ_1 values emerge generally in the entering region of the contact zone. The largest σ_1 value can be found at 12 N load. Interesting to see, that in the middle region of the contact zone the lowest stress values are to observe at 12 N normal load. After the middle zone there is an inflexion in the σ_1 values and compression occurs (negative stress values). At the leaving edge of the steel roller the largest stress values are noticed again at 12 N normal load. Practically the same situation holds for Figure 82-b and Figure 82-c i.e. for the running-in and steady-state phases. Nevertheless, the most surprising feature is that the stress distribution in the middle region of the contact shows characteristic differences for the different load cases. In Figure 82-c the σ_1 stress distributions are clearly separated. The largest stress values in the middle part of the contact zone are evaluated at 8 N normal load, while the smallest one at 4 N normal load. This finding is in agreement again with the experiments (cf. Figure 75) showing that most severe wear occurs at 8 N normal load.

In Figure 83 a-c one can see the deformed FE mesh and the ε_y (comp 22 of total strain) strain results using a coloured map. The pictures show the simulation test results after 90 min testing at 4, 8 and 12 N normal loads, respectively. These results are in correlation with the normal load distribution results. The same tendency is to observe in this case as given by the data in Figure 82 a-c. On the coloured charts one can see the tension and compression strain results. The largest compressive deformations emerge at 12 N normal load (cf. Figure 83-c), while the largest strains in tension are detectable at 8 N normal load (cf. Figure 83–b). Recall that material failure will occur in tension and not in compression, as disclosed in chapter 7.1. The FE results show that the applied COF values which were deduced from the measurements have a great influence on the σ_1 stress distribution results. On the

other hand, the temperature development and COF changes during the tests suggest that more attention should be paid to the micro and nano-scaled deformations and flash temperatures on the rubber surface, because the deformability of the rubber changes markedly under such extreme situations (flow, network degeneration, etc…). These results are important because it is already obvious what kind of strong correlation exists between the loss volume and COF changes.

Further comments and explanations related to the FE simulations (designations and theory) are summarized in Appendix 1 (chapter 11.1).

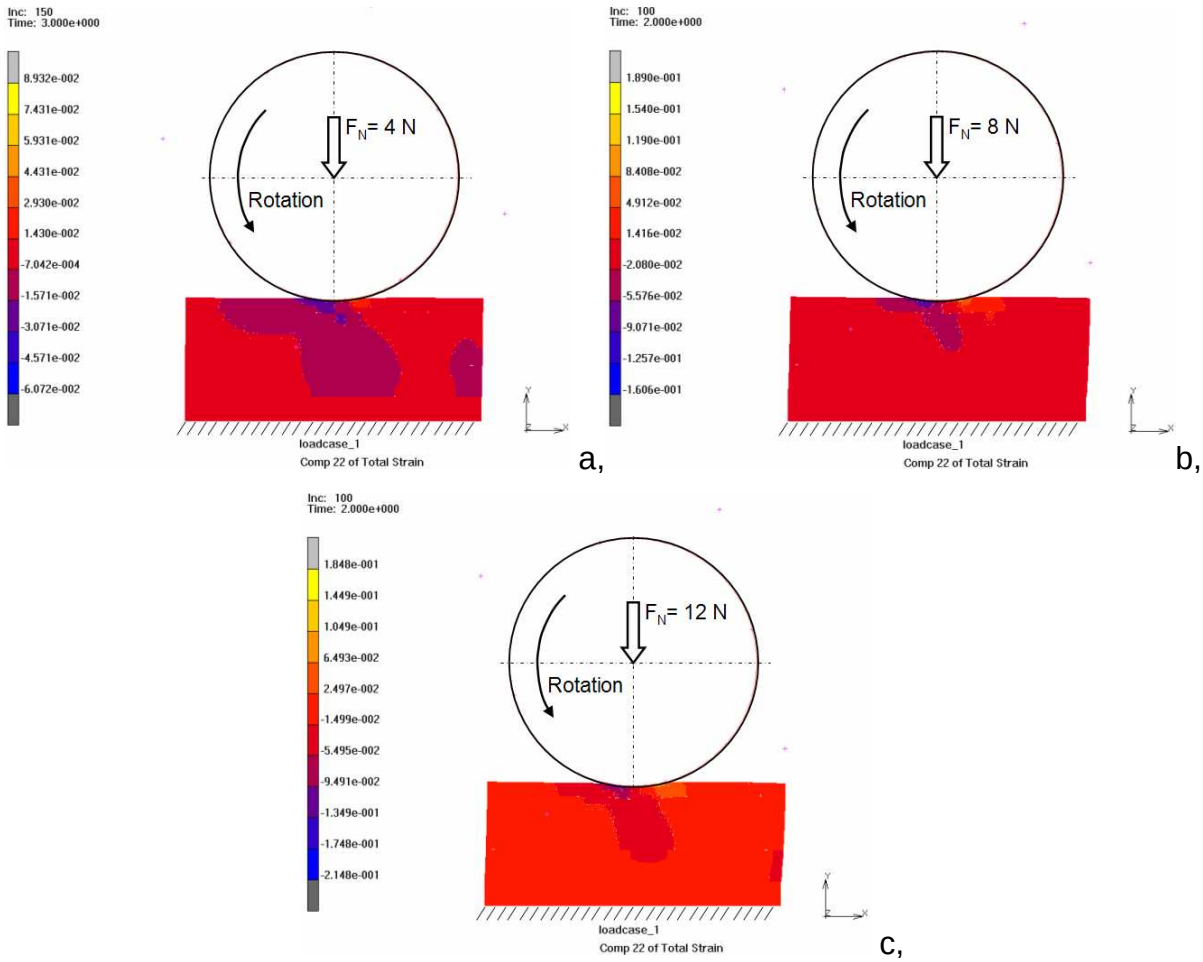

Figure 83: Deformed shape of the FE meshes simulating a testing time of 90 minutes at different normal loads. Designations: -a; 4 N, -b; 8 N and -c; 12 N.

8 Chemical composition analysis of the wear surfaces

The use of new materials with improved properties for tribological applications is of great interest for the modern industry, where the losses due to wear represent a significant economical obstacle. In practice, rubber is normally subjected to various environmental attacks such as thermal aging, radiation exposure, and chemical influence. Deterioration of the material properties of rubber is expected because of changes in molecular structure resulting from these environmental attacks [102]. The study of degradation and stabilization of polymer is an extremely important area from both scientific and industrial points of view, and a better understanding of the degradation mechanism of these materials will help to ensure improved durability to the products. However, not enough attention has been paid to study the durability of polymer nanocomposites [103]. In addition, the knowledge of the surface chemical composition and on its change owing to different applications is crucial for the understanding of the material's behaviour. Several surface modifications have been used for elastomers to modify their surface properties [104,105]. Previous studies [106] pointed out the importance of a good chemical characterisation for understanding and comparing the results obtained. In this chapter, the changes in the chemical composition of the surfaces of different carbon black containing EPDMs are studied before and after wear. An evaluation of the chemical surface modification by means of X-ray photoelectron spectroscopy (XPS) is performed on the EPDM samples. In addition changes in the surface energetic were followed by the sessile drop method on the wear track after tribological tests. Contact angle measurements were performed with water in order to analyse the hydrophobicity of the surface and its change due to tribological tests [107].

8.1 Tribological Tests

For the chemical investigation of the wear tracks those samples were chosen, which were tested under the highest normal load (F_N=12N). The results of the tribological tests are summarised in Figure 84 where the coefficient of friction (COF) and loss volume results are depicted for the different EPDMs. In Figure 84 one can see that the variation is small in the steady-state COF values. They are scattered around the value of 1.5. So the CB content of the EPDM rubber does not affect the

COF. On the other hand, this suggest, that the mean molecular mass between crosslinks is the dominant parameter during dry sliding, as this parameter is probably identical for the EPDMs when disregarding the effects of their CB content. The loss volume values clearly show the reinforcing effect of the CB particles incorporated. The loss volume decreases with increasing CB content. This significant change in the wear is well visible even in logarithmic representation.

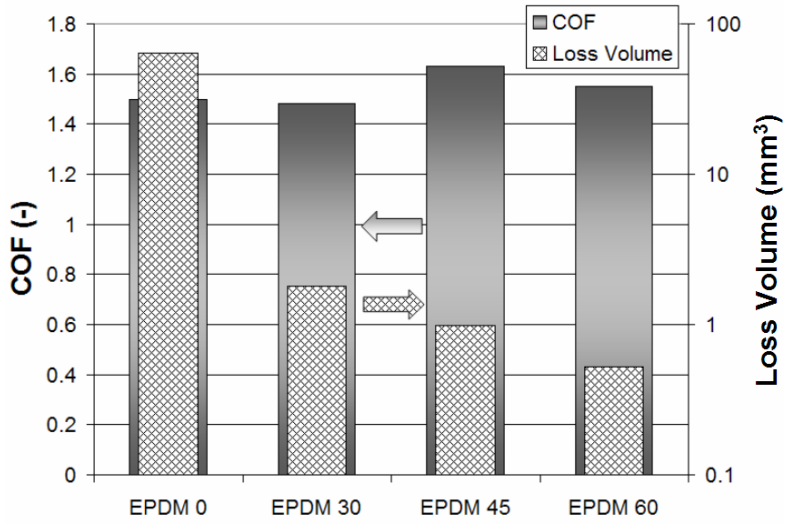

Figure 84: Tribotest results of ROP tests using 12 N normal load

8.2 X-ray photoelectron spectroscopy of the surface

Figure 85-a displays the surface composition of EPDM with different CB contents. The EPDMs mainly presented carbon and oxygen on their surfaces, smaller amounts of other elements, like Si, S or N and traces of Zn. In order to facilitate the analysis of the results, the elements present in small amounts are not displayed in the figures. The comparison between the surface compositions of each EPDM evidenced that CB enhanced the presence of elements different from carbon, especially oxygen. However, there is no clear trend in respect to chemical composition with increasing CB. The composition showing the largest difference from all another's was the EPDM 30.

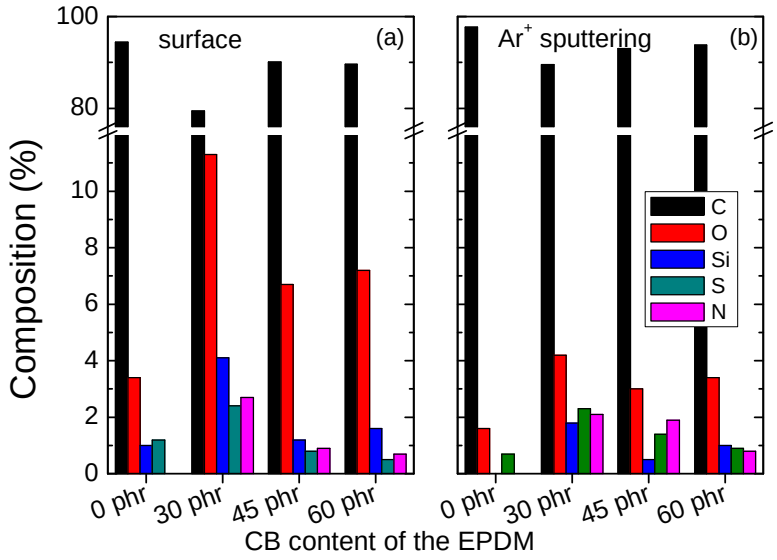

Figure 85: Surface composition of EPDM with different carbon black contents (a) before and (b) after Ar^+ ion sputtering of the surface.

A sputtering process was carried out in order to remove the contamination layer of the surface. Figure 85-b displays the surface composition of the EPDM samples after this process. All the EPDMs presented higher carbon content after sputtering than before. A decrease in the amount of oxygen was observed for all samples (between a 2 and 7 %). The elements present in smaller amounts, showed negligible variations. In the case of EPDM 0 phr CB, Si was completely removed out of the surface. When CB was present in the EPDM, the amount of Si decreased (up to a 2 %) but it was still present in all the samples. Therefore, the results after sputtering evidence a homogeneous composition of the EPDMs independently of their CB contents.

In order to investigate changes in the main bonding of the elastomers, a curve fitting procedure for the C 1s core level peaks was performed. Up to four components were used for the fitting process, taking into account the natural oxidation of the elastomer [108, 109]. The main component corresponded to the C-C/ C-H bond at 285 eV. The rest of the components used for the fitting corresponded to C-O at 286.3 eV, C=O at 288.1 eV and O-C=O at 289.0 eV with a deviation of ±0.1 eV. Table 10 presents the results for the EPDM samples obtained after the fitting process of the C 1s core level peak. The EPDM 0 phr CB showed no oxidised compounds on the surface and all the carbon present in this sample corresponded to the backbone structure of EPDM. This sample contained the highest amount of carbon in the entire range of the EPDMs tested (Figure 85-a). On the contrary, the samples with CB

presented certain contribution of oxidised components on their surface, although the oxygen content was lower than 7 %. After the sputtering of the surface, no oxidised components were found on the C 1s peak of any of the samples tested.

Table 10: Analysis of the C 1s core level peaks for the original surface and inside the wear track of the EPDMs with different carbon black contents.

	COMPONENTS (%)							
	surface				wear track			
	C-C/ C-H	C-O	C=O	O-C=O	C-C/ C-H	C-O	C=O	O-C=O
EPDM 0	100	0	0	0	100	0	0	0
EPDM 30	93	5	1	1	93	5	0	2
EPDM 45	95	2	0	3	96	1	0	3
EPDM 60	95	2	0	3	96	3	0	1

8.3 X-ray photoelectron spectroscopy of the wear track

After the tribological tests, the surface composition of the wear tracks was also analysed. The results are plotted in Figure 86-a. The EPDM 0 sample presented higher oxygen and Si content on the wear track than out of it (Figure 85-a). In contrast, the EPDM samples with CB presented a smaller amount of oxygen on the wear track than the EPDM 0. It was found a progressive decrease in the oxygen content with the increasing CB content and the EPDM 60 sample showed the closest composition to the EPDM without CB. After a sputtering of the surface (Figure 86-b), a decrease in the oxygen content was registered, equivalent to the one observed outside the wear track. Other elements like Si diminished only in the samples containing of CB. As a result changes in the global composition of the wear track are smaller than on the surface.

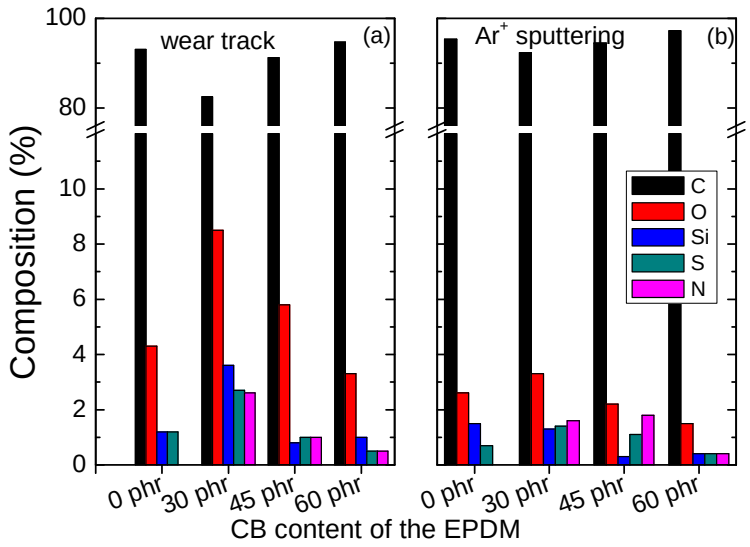

Figure 86: Surface composition of the wear track of EPDM with different carbon black contents (a) before and (b) after the sputtering of the surface.

The analysis of the C 1s core level of the samples inside the wear track (Table 10) evidenced no significant modifications on the carbon bond in comparison to the results obtained out of the wear track. After the sputtering process, the oxidised components of the carbon peak are completely removed in both regions. Therefore, despite the modifications observed in the surface composition of the samples inside and outside the wear track, the structure of the polymer seemed to be unaltered after the tribological tests. However, there is still one question that has to be clarified. The amount of oxygen found on the samples is not proportional to the oxidised components found on the carbon peak. We found that silicon and sulphur are present in oxide form on the sample surface of EPDM 0. This oxide contribution diminished in the wear track and, after the sputtering process, the Si was still in oxide form, while no oxidised sulphur was found. To illustrate this change in the surface composition, Figure 86 shows the alternation in the sulphur peak on the surface of EPDM 0 sample. In the case of EPDM 30 sample, the total sulphur content on the wear track is similar to that one found on the surface, but a smaller proportion of oxidised sulphur is found in the wear track. After Ar+ sputtering, the wear track presented no oxidised sulphur and a lower oxygen and silicon content. This result is in contrast with the findings out of the wear track, where some remaining sulphur was found in its oxide form. Thus, differences found in the oxygen content can be attributed to oxide bonds different from carbon. In the case of EPDM 45 sample, the sulphur present on the surface was not in oxide form and the variation observed in the

oxygen content in the wear track could only be attributed either to the lower silicon content in this region (always in oxide form), or to the oxidised components of the carbon peak. Finally, the EPDM 60 sample presented no sulphur in oxide form, as occurred in the EPDM 45 sample. The analysis of the C 1s core level of this sample evidenced that the regions out of the wear track presented a higher presence of carboxyl groups that implied a higher oxidation state. This may be the cause for the higher presence of oxygen out of the wear track.

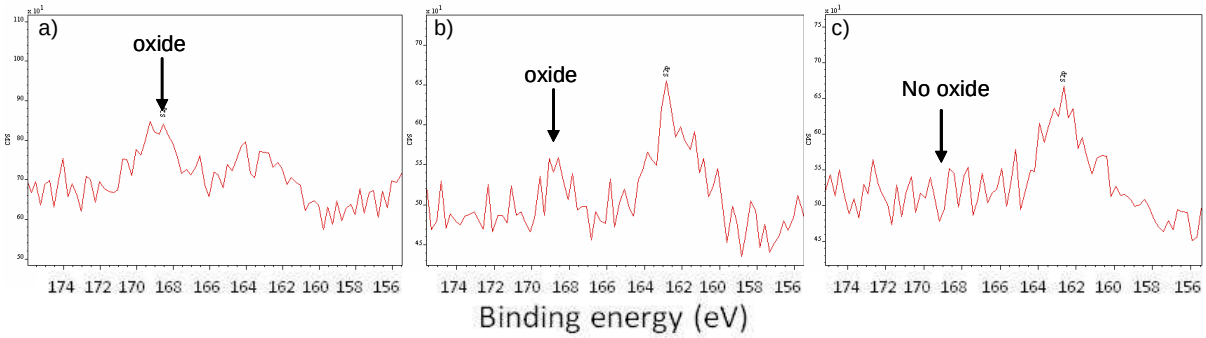

Figure 87: Zoom of the wide energy range scan of EPDM 0 phr CB at the energy of the S 2p peak in (a) the surface, where more than the half of the sulphur is oxidised, (b) the wear track before the sputtering process, where only a small amount of the S is oxidised and (c) the wear track after sputtering of the wear track, where no oxide was detected in the sulphur peak.

8.4 Contact angle measurements

Contact angle (CA) measurements were performed on the EPDM surfaces before and after the tribological tests with water. Figure 88 shows a comparison of water droplets of the same volume inside and outside the wear track. The CA values measured in both regions of each sample are displayed in Figure 89. No significant variations on the hydrophobicity of the samples were observed outside the wear track as a function of the carbon black content. This result seems to be in correlation with the COF results and confirms that the adhesion phenomena may be the dominant during dry sliding not the hysteretic damping effects. The EPDM 0 phr presented a slightly lower CA, but the variation is within the experimental error. There is a tendency in all the samples to increase the CA values inside the wear track, which represented a higher hydrophobicity than the unworn region of each sample. The EPDM 0 phr showed the biggest increase in this value. On the other EPDMs with CB, there is a tendency to observe: CA increases with increasing CB content.

Changes in the hydrophobic properties are highly dependent on the surface chemistry. An outer layer dominated by methyl groups (-CH3) shows hydrophobic properties, while the arrangement of oxygen functional groups (-C-OH, -C=O) at the outer layer induces a better wettability by polar liquids like, water [110]. In our case, the EPDM with 0 phr presented no oxidised components in the analysis of the C 1s core level, which can explain the higher hidrophobicity of this sample. The rest of the EPDM with different CB phr presented small amounts of oxygen functional groups on their surfaces that resulted in lower contact angles than EPDM 0. However, the modifications on the surface composition are not large enough to explain the difference observed neither in this sample, nor in the comparison between outside and inside of the wear track. Thus, the increase in the surface roughness, caused by the tribological test, may play a major role in the alteration of the CA.

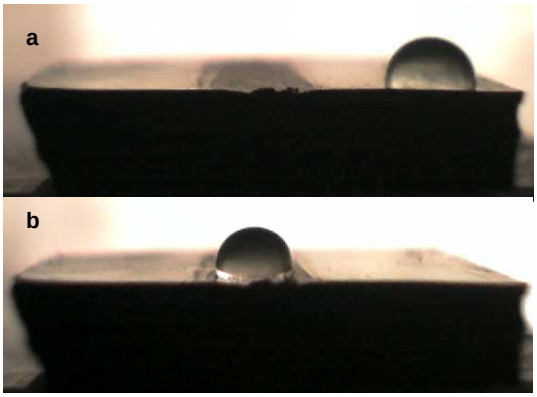

Figure 88: Comparison of 4µl water droplets on the original surface (a) and the wear track (b) of EPDM 60

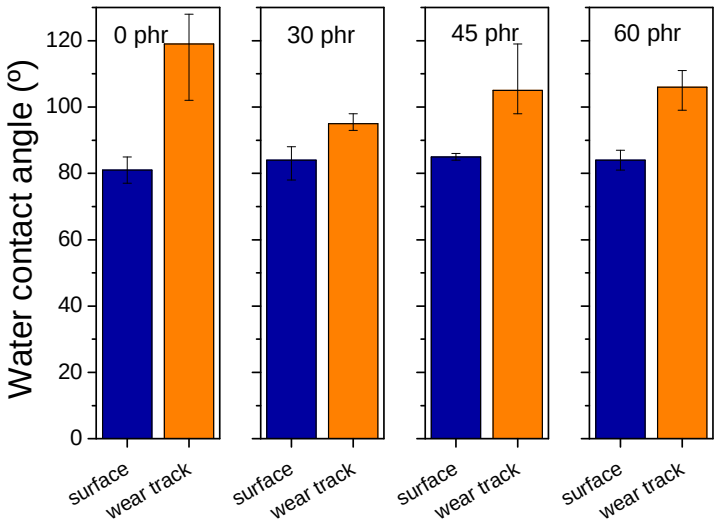

Figure 89: Water contact angle on EPDMs with different carbon black contents in the wear track and outside

8.5 Raman Spectroscopy

Raman spectroscopy was performed on the surface and ob the wear track of EPDM 60 phr CB. The results are plotted in Figure 90. Two scattering peaks can be observed in both regions The peak at around 1603 cm^{-1} is assigned to C=C stretching vibration, and the other one at 1368 cm^{-1} is assigned to C-H symmetric deformation vibration of methyl group [111]. According to Figure 90 the C=C signal of the sample increased due to the sliding wear. The presence of this specie cannot be detected in the XPS measurements, as it is shifted 0.3 eV towards lower binding energies than the C-C bond [112] and thus it cannot be resolved with the equipment used.

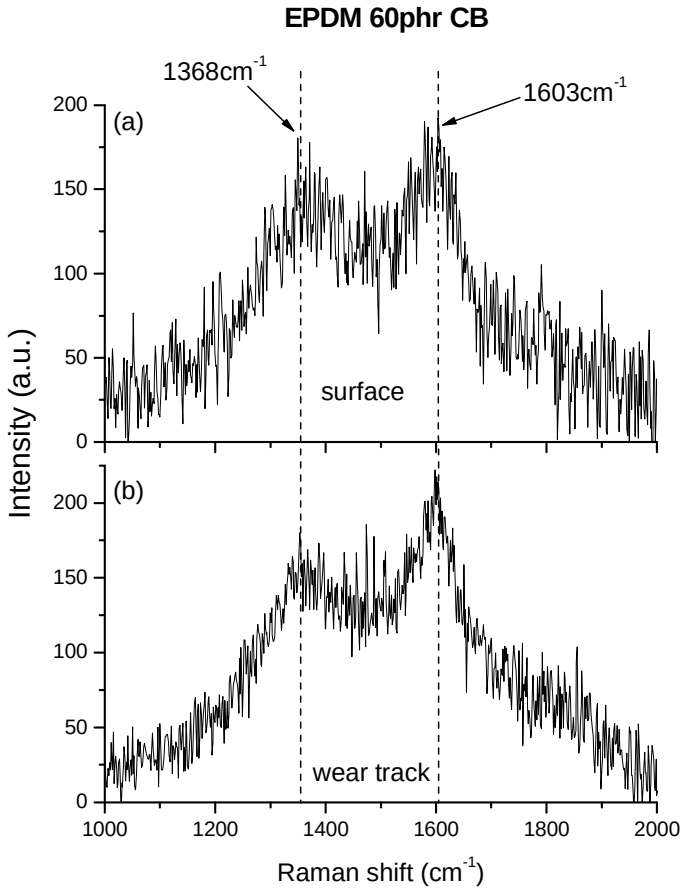

Figure 90: Raman spectra of the surface (a) and wear track (b) of EPDM 60 phr CB

8.6 Conclusions of the chemical investigation

The study within this chapter was a trial to figure out those chemical processes which may occur during dry sliding of steel and EPDM rubber counterparts. By detecting changes in the chemical composition one would be able to deduce molecular mechanisms (chemical processes) during dry sliding. All of the above

results are of fundamental importance to understand the whole wear process, because there are limited further possibilities to investigate the real molecular interactions between sliding pairs. There was no clear influence of the CB percentage on the elemental composition of the surfaces of the EPDMs. The main feature observed is an increase in the oxygen content with increasing CB. A comparison of the surfaces' elemental composition in the wear track and out of it evidenced a smaller amount of oxygen in the wear track of the samples with CB in their composition. The increasing percentage of carbon black reduces the presence of oxygen content in the wear track. In addition, there is a parallel tendency: a smaller contribution of carbon- oxygen containing bonds to the C 1s core level in the wear track of the samples with CB. The contribution of these C-O bond containing components remained always below 8 % according to Table 10. On the contrary, the sample with no CB presented higher oxygen content in the wear track, although it has no oxide contribution in the carbon peak. These facts indicate that the oxidation of the backbone structure of the EPDM is not the only cause for the lower presence of oxygen in the wear track. Other elements present in smaller amounts, like silicon, also presented a tendency to decrease due to wear. This element was always found in oxide form and, therefore, could influence the amount of oxygen in the wear track. In addition, small quantities of sulphur are always present in the samples. Part of this sulphur is in oxide form and the proportion of the related oxide is lower in the wear track than outside of it. For percentages of carbon black higher than 45 phr, sulphur was not found in oxide form neither in the wear track, nor out of it. All these oxides are located in the outer part of the surface, as reflected their significant removal after a slight sputtering process. Therefore, it seems that part of the oxide compounds present on the EPDM surface could be desorbed to the gas phase during friction. Our results suggest that the most important wear mechanism occur in nano- as well as in micro scale and not in the investigated molecular range. It may mean that the wear process is driven by mechanical failures and less by chemical reactions.

9 FE Simulation of Dry Rolling Friction of EPDM 30

Rubbers are utilized widely in the mechanical engineering. Tires, v-belts, belts, rollers are made of rubbers or of rubber-based composite materials. The water-, heat- and chemical-resistances, the excellent and tailorable elastic properties, the high coefficient of friction makes them as first-choice materials for the above applications. However the construction and design of the related rubber parts need profound knowledge on the non-linear and viscoelastic properties of the related rubbers. The internal damping of rubbers can be useful, but the same phenomenon can cause unfavourable energy dissipation during rolling or cyclic fatigue-type loading of rubbery elements.

The exact analytical calculation of the observed strains during mechanical loading of rubbery elements is a great challenge due to the complexity of the viscoelastic material models. Although some simplified analytical methods were developed to evaluate for example the friction resistance or internal heat generation in viscoelastic materials during rolling contact, they failed for more complex stress states or for repeated stresses [52, 54, 57, 58, 59, 62, 63, 113, 114]. On the other hand the finite element (FE) method is able to handle complex viscoelastic material models owing to the permanent advancement of the software and hardware background. This progress makes possible to perform more complex and at the same time, accurate simulations [64,65].

The aim of this study was to investigate the rolling friction whereby a steel ball is rolling on a rubber plate made of EPDM 30 (see chapter 6.5.2).

The linear-viscoelastic properties of the rubber were determined by dynamic mechanical thermal analysis. On the basis of DMTA measurements a master curve was created and a 15-term Maxwell-model was fitted to this master curve (see chapter 3.3 and 7.2). To describe the incompressibility and the non-linear behavior of the rubber, the Mooney-Rivlin material model was used (see chapter 3.2.2 and 7.1.1). The constants of the two term Mooney-Rivlin material law were calculated by simplified equations (8.2.1 and 8.2.2).

For the simulations the FE software MSC.Marc was used. The results of the tests and the FE simulations were compared with each other and discussed.

9.1 Results of the Rolling Friction Test

The rolling friction test is described and discussed in details in chapter 6.5.2. During the measurement the normal and the tangential force were registered (cf. Figure 91). In Figure 91 one can see the change of the normal and tangential forces in one cycle and the calculated coefficient of friction (COF). The COF is calculated as the ratio of the friction force to the normal load (Equation 8.1.1).

$$COF = \frac{F_T}{F_N}, \qquad (9.1.1)$$

where F_T is the tangential force, F_N is the normal force.

The sign of the friction force is changing, due to the changing rolling direction. The normal force is constant; however a small deviation was observed during the cycle. The highest and smallest values of the tangential force are approximately ±4.8 N. Between the direction changes of the rolling ball a plateau can be seen in the tangential force vs. time curve. The COF vs. time curve has also an oscillation, the maximal and minimal value of it are approximately +0.034 as well as -0.034.

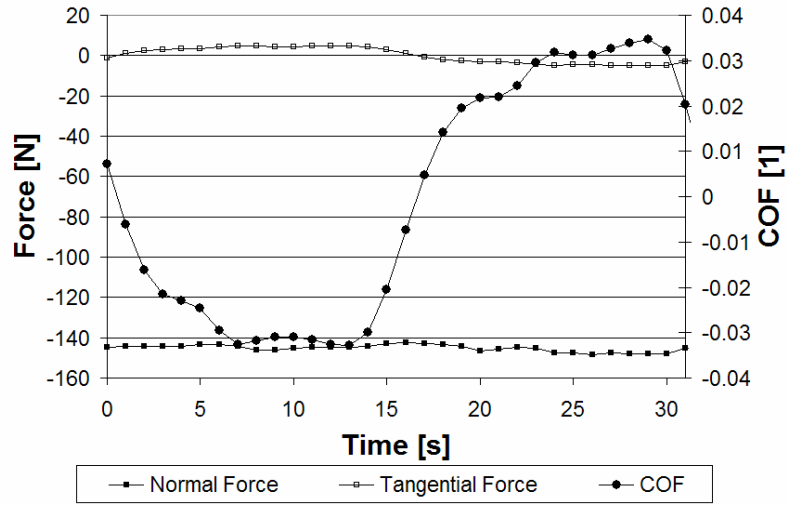

Figure 91: Change of the normal- and tangential forces vs. time in one cycle and change of the calculated COF

9.2 Material Model

The mathematical description of the viscoelastic material behaviour is a complex task. With the help of the ViscoData software [35] we have fitted a 15-term Maxwell-model to the measured storage moduli master curve (see chapter 7.3)

[29,30,33]. The detailed description of the Maxwell-parameter optimization is described in ref. [35]. The parameters of the Maxwell-model are summarized in Table 5. The storage modulus master curve of the DTMA measurements and the fitted master curve of the 15-term Maxwell-model can be seen in Figure 51. The listed Maxwell-parameters in Table 5 (relaxation time (τ) and dimensionless elastic moduli (coefficients) of each Maxwell-element) are formulated specifically for the MSC.Marc FE software.

During the FE-simulation the 15-term Maxwell-model was combined with a two parameter Money-Rivlin material model. According to the MSC.Marc software the constants of the two term Mooney-Rivlin material law were calculated from the Young's modulus of the material measured at -100°C (see E_0 in Table 5) using equations (8.2.1) and (8.2.2) [23,115].

$$E = 6(C_{10} + C_{01}), \qquad (9.2.1)$$

$$4 = \frac{C_{10}}{C_{01}}, \qquad (9.2.2)$$

where,

C_{10} – is the first Mooney-Rivlin parameter,

C_{01} – is the second Mooney-Rivlin parameter,

E – is Young's modulus.

Adjusted to the formulation of the FE software, the Mooney-Rivlin parameters were calculated based on the highest modulus of the EPDM rubber material. Using equations (8.2.1) and (8.2.2), the calculated Mooney-Rivlin constants are the followings:

C_{10} = 123 MPa,

C_{01} = 493 MPa.

9.3 FE simulation results of the rolling friction test

The FE model of these simulations is described and discussed in chapter 6.8.2. Within this chapter the results of this FE model are summarized. Friction force, normal load and the calculated COF from the simulation are shown in Figure 92. The FE-calculated reaction force in vertical (z) direction at the rigid sphere (cf. Figure 42) is defined as the normal force. The friction or tangential force is the reaction force in x-direction (cf. Figure 42) which is calculated at the rigid surface gluing to the rubber

plate. One can see in Figure 92 that the direction of the friction force was reversed when the ball moved back and the COF shows clearly oscillating characteristic. The COF was calculated using Equation (8.1.1).

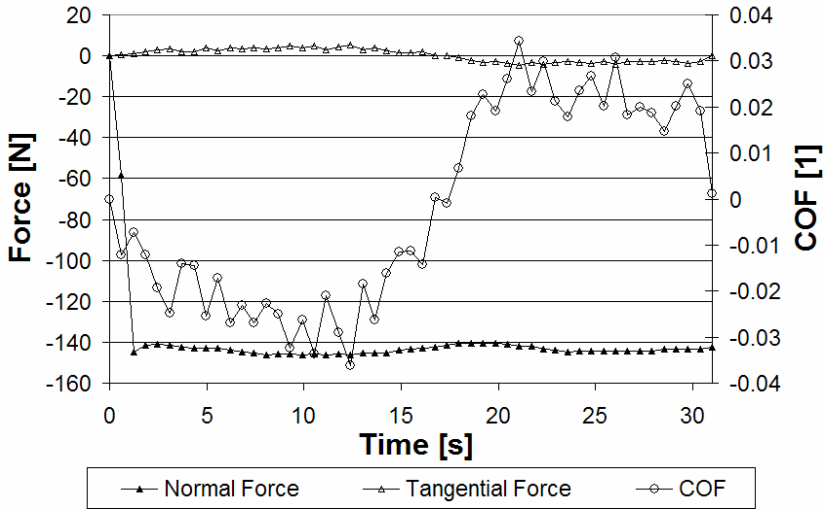

Figure 92: Friction force, normal force and COF calculated by FE simulation

9.4 Comparison of the measured and the FE simulated results

The measured and FE-calculated friction and normal forces are displayed in Figure 93. The curves from the simulation show a fair agreement with the experimental ones. It means that the FE simulation is usable to analyze the rolling process on the rubber plate and get a well quantitative description of the rolling friction.

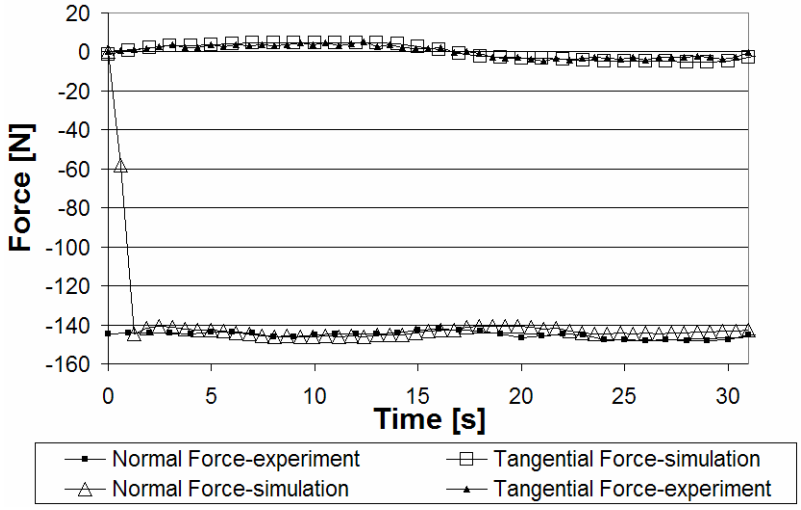

Figure 93: Comparison of friction force and normal loads between experiment and simulation in one cycle

A more slightly comparison is the collation of the measured and FE-simulated COF results (cf. Figure 94). Although the measured and the FE calculated values don't cover each other perfectly, the difference between the results is very small. One explanation may relate to the assumption of pure rolling, because in the contact area the micro-slip phenomenon [116] produces stick-slip around the sticking zone (cf. Appendix 2 in chapter 11.2). On the other hand the oscillations in the COF results can be related to numerical instabilities during the FE calculations.

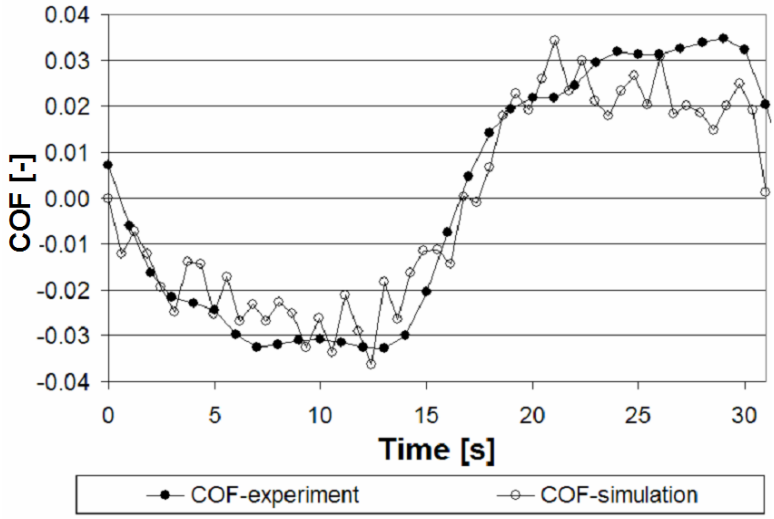

Figure 94: Comparison of COF between experiment and simulation in one cycle

9.5 Conclusions of the Rolling Friction FE Results

This study describes a general method on how to consider the viscoelastic behavior of rubber materials. The description of the viscoelastic material behavior can be realized, for example, with proper number of Maxwell elements, by which the simulation results can well be adjusted to those of the experiments. Increasing number of elements in the FE-model and / or increasing number of steps during the simulation may further improve the accuracy of the calculations. However, both of the listed refinements can lead to a pronounced increase of the CPU time. Based on the results presented in this work the following conclusions can be made:

- The viscoelasticity of the EPDM material was determined by DMTA measurements successfully.
- The fitted 15-term Maxwell-model is able to describe the viscoelastic behavior of the investigated EPDM rubber.
- The FE method used is powerful tool to consider the viscoelastic properties of rubbery materials accordingly and to simulate their process of rolling friction.

10 Summary and Outlook

In this work the tribological properties of EPDM rubbers, with different amount of CB, were analysed under dry sliding and rolling conditions. For a better understanding of the tribological processes the mechanical behaviours of the different EPDMs were investigated applying tension, compression and DMTA tests. In addition, the tribotests were analysed applying FE simulations to highlight the onset of complex stress-strain states during the tribotests.

The tension tests showed that with increasing CB content the stiffness and the strength of the EPDMs increase rapidly until 45 phr CB content. Further incorporation of CB results minor stiffness and strength increase. Prominent increase in the elongation at break was also detectable with increasing CB content.

Increasing CB content enhances the stiffness also in compression. An unexpected phenomenon was observed during the compression tests of the CB containing EPDMs. The real stress-strain curves of the compression tests showed clearly, that the CB filled EPDMs undergo a yielding process when subjected to high compression strains. This finding is considerably surprising knowing that the EPDMs are fully crosslinked. Further on, no visible damage of the CB filled EPDMs was detected after the compression tests. In contrary, no yielding was observed in the unfilled (neat) EPDM, which became heavily damaged after the compression tests.

Based on the engineering stress-strain curves under tension and compression two parameter Mooney-Rivlin material models were created to consider the nonlinear material behaviour of the investigated EPDMs. It was found that the two parameter Mooney-Rivlin model can fairly describe the nonlinearity of the EPDMs in both compressive and tensile loadings.

The viscoelastic behavior of the 30 phr CB containing EPDM (EPDM 30) was determined using DMTA measurements. DMTA tests were realized in tension mode and the complex stiffness and mechanical loss of the EPDMs were determined as a function of temperature and frequency. This type of DMTA test enabled us to create the storage modulus (E´) vs. frequency master curve for the EPDM 30 using the WLF time-temperature equivalence theory.

A 15-term Maxwell model was fitted to the E´ vs. frequency master curve adopting the ViscoData software. It was found that the 15-term Maxwell model

describes adequately the linear viscoelastic behavior of the EPDM rubber in a broad frequency range.

The loss volume results after dry sliding tribotests under ROP conditions showed that the CB content of the EPDM generally influenced the wear behavior of the elastomer. It was found that the loss volume increases with increasing normal load for the unfilled EPDM. On the other hand, when CB is incorporated into the EPDM the wear behaviour changes drastically. It was shown up, that due to the incorporated CB the detectable wear increased as a function of normal load until reaching a threshold value. Above the threshold normal load the loss volume decreased with increasing normal load. The most significant change in the loss volume was detected for the EPDM 30.

The value of the COF changed markedly with increasing normal load and testing time. During the initial phase of the tests a fast increase in the COF was found. After an initial phase of COF increment, the COF was markedly reduced and stabilized for the rest duration of the test for the (neat) EPDM 0. For the EPDMs with CB content the COF increased in the running-in phase steeply. However in steady-state condition the COF decreased with the time before tending to some characteristic value. The COF in the steady-state as a function of the applied normal load decreased consequently with increasing normal load for both EPDM 0 and EPDM 30. For the EPDM 45 and EPDM 60 the steady-state COF reached its maximum at a threshold normal load.

During the ROP tribotests the temperature increased monotonic with both increasing normal load and testing time. In the initial phase of the tests (running-in) a fast temperature rise was always detectable.

SEM inspection of the worn surfaces proved to be helpful to explain some unusual tribotest results. The large wear observed for the EPDM 0 is due to its poor mechanical performance. With increasing normal load and temperature large plastic deformations were detected on the worn surfaces for the CB containing EPDMs. Above the threshold normal loads the increasing plastic deformability of the CB containing EPDMs caused a decrease in both COF and loss volume. Moreover, a rubber tribofilm was generated on the surface of the steel counterpart above a threshold normal load when the EPDM 30 was tested. This rubber tribofilm protects the rubber surface during the tribotest and reduces by this way its wear. Important experimental finding is the “self “healing” effect observed for the EPDM 60 rubber.

This phenomenon was traced to highly filled wear debris, which adhered easily to the previously worn surface building that way a new “protective” surface layer.

The change in the chemical composition of the worn surfaces was analysed using XPS, contact angle measurements and Raman spectroscopy. Though the XPS technique showed differences between the surfaces of the different EPDMs, clear changes in their chemical compositions were not found when collecting the results before and after the wear tests. Based on the contact angle measurements relevant changes occurred in the surface free energies due to the wear tests. On the other hand these changes in the contact angle may just reflect changes in the surface roughness. With help of the Raman spectroscopy no change was found in the chemical composition of the surfaces due to the tribotest.

Adopting of FE simulations the effect of the contact geometry, changing due to the wear, was considered through which correlation was found between the actual COF and wear. The FE simulation of the rolling tribotest reflected very well the experiments. This proved the correctness of the viscoelastic material model and FE approach used.

Based on the above results no correlation was found between the material properties and the tribological performance of the investigated materials. On the other hand, this study has highlighted that the material properties highly depend on the hydrostatic pressure and temperature which have to be investigated in depth to shed light on the “plastic” deformability of the elastomers. Further FE investigations are needed to estimate the micro and nano scaled contact stresses, and to derive reliable flash temperatures.

11 Appendix

11.1 Appendix 1

For the better understanding of the FE results let us consider the sketch of the FE model of the ROP tribotest with an optional mesh in deformed state (cf. Figure 95). In chapters 7.4.4, 7.5.4, 7.6.4 and 7.7.4 different stress distributions are depicted in the contact area. The contact area or the length of the contact area mean that curve section along which the steel roller and the deformed rubber specimen are in touch with each other. This curve section is shown in Figure 95 by a black arrow between the steel roller and the rubber specimen. As it is also to see the symmetry line of the rubber specimen do not coincides with the middle point of the contact area (cf. Figure 95). In the stress distribution diagrams in chapters 7.4.4, 7.5.4, 7.6.4 and 7.7.4, the sliding direction shows always right, corresponding to the test configuration.

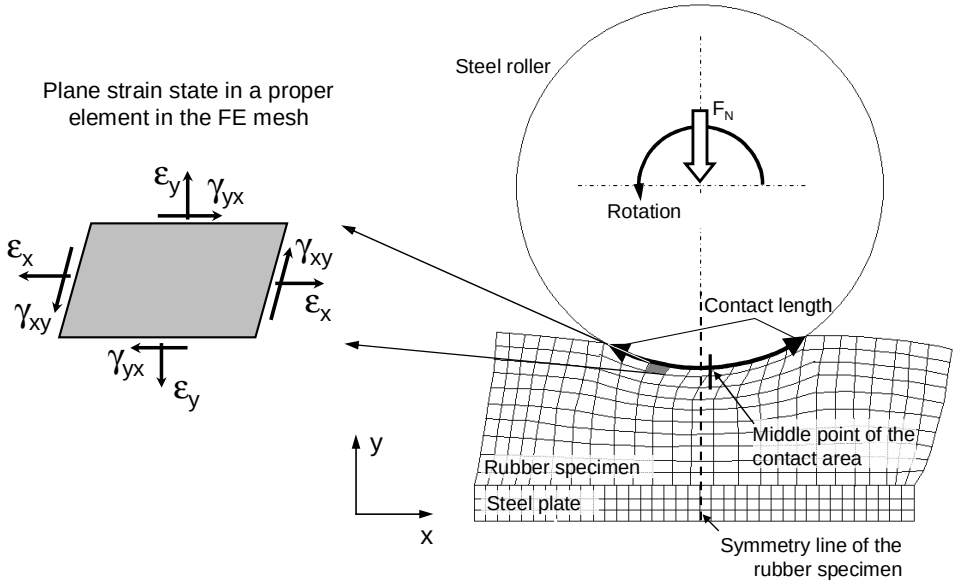

Figure 95: Schematic sketch of the deformed mesh of the ROP tribotest and the plane strain state in a proper element

Plane strain state was assumed for the FE simulation. Figure 95 shows a randomly chosen element of the FE mesh, adjusted to the rubber, in enlarged scale. On this enlarged FE element the different components of the plain strain tensor (ε_x, ε_y, γ_{yx} and γ_{xy} cf. Equation 1) are shown. Note that in plane strain state perpendicular to the assigned x-y plane no strain arises. Accordingly in the plane strain tensor (Equation 1) the value of ε_z is zero. In Equation 1 the values of γ_{yx} and γ_{xy} are equal.

In chapter 7.4.4 the comp. 22 of total strain (based on the designation of the Msc.Marc software pckage) designates ε_y in the strain tensor (Equation 1).

$$\underline{\underline{\varepsilon}} = \begin{bmatrix} \varepsilon_x & \gamma_{yx} & 0 \\ \gamma_{xy} & \varepsilon_y & 0 \\ 0 & 0 & 0 \end{bmatrix} \tag{1}$$

According to Hooke's law, the elements of the strain tensor (ε_x, ε_y, γ_{yx} and γ_{xy}) are accompanied by proper stresses, also in a form of a tensor (cf. Equation 2). Note that in plane strain state the value of σ_z is not zero and similar to the strain tensor (Equation 1) the values of τ_{yx} and τ_{xy} are equal.

$$\underline{\underline{\sigma}} = \begin{bmatrix} \sigma_x & \tau_{yx} & 0 \\ \tau_{xy} & \sigma_y & 0 \\ 0 & 0 & \sigma_z \end{bmatrix} \tag{2}$$

The values of Equation 2 following Hooke's law can be expressed as follows:

$$\sigma_x(x,y) = \frac{E}{1+\nu}\left(\varepsilon_x + \frac{\varepsilon_x + \varepsilon_y}{1-2\nu}\nu\right), \tag{3}$$

$$\sigma_y(x,y) = \frac{E}{1+\nu}\left(\varepsilon_y + \frac{\varepsilon_x + \varepsilon_y}{1-2\nu}\nu\right), \tag{4}$$

$$\tau_{xy}(x,y) = \frac{E}{2(1+\nu)}\gamma_{xy}, \tag{5}$$

$$\sigma_z(x,y) = \nu \cdot (\sigma_x + \sigma_y). \tag{6}$$

In Equations 3 – 6 E - is the Young modulus, while ν - is the Poisson ratio of the related material. According to the assignations of the Cartesian coordinate system in Figure 95 the σ_y characterizes the normal pressure in the contact area. In chapters 7.5.4, 7.6.4 and 7.7.4 the largest principal stress (σ_1) is depicted along the contact length. In the following the determination method of the principal stresses will be detailed. The tensor of the general stress state (Equation 2) can be transposed to a principal stress tensor, which is able to describe the stress state independently from the base coordinate system without shear stresses. For this purpose one need to define the eigenvalues of the stress tensor (Equation 2) as it is shown in Equation 7 in form of a determinant.

$$\begin{vmatrix} (\sigma_x - \sigma_i) & \tau_{yx} & 0 \\ \tau_{yx} & (\sigma_y - \sigma_i) & 0 \\ 0 & 0 & (\sigma_z - \sigma_i) \end{vmatrix} = 0 \tag{7}$$

Equation 7 can be written otherwise as a third power equation (cf. Equation 8).

$$\sigma_i^3 - F_I \cdot \sigma_i^2 - F_{II} \cdot \sigma_i - F_{III} = 0 \quad (8)$$

In Equation 8 F_I, F_{II} and F_{III} are the first, second and third scalar invariants of the stress tensor in plane strain state, respectively. The values of σ_i – (i=1-3) should be determined. The first, second and third scalar invariants of the stress tensor in plane strain state (F_I, F_{II} and F_{III}) are determined according Equations 9, 10 and 11.

$$F_I = \sigma_x + \sigma_y + \sigma_z \quad (9)$$

$$F_{II} = \sigma_x \cdot \sigma_y + \sigma_y \cdot \sigma_z + \sigma_z \cdot \sigma_x - \tau_{xy}^2 \quad (10)$$

$$F_{III} = \sigma_x \cdot \sigma_y \cdot \sigma_z - \sigma_z \cdot \tau_{xy}^2 \quad (11)$$

The solution of Equation 8 delivers three eigenvalues, namely σ_1, σ_2 and σ_3. The following relation was introduced to differentiate the three principal stresses (cf. Equation 12).

$$\sigma_1 > \sigma_2 > \sigma_3 \quad (12)$$

Based on Equations 13, 14 and 15 one has the possibility to calculate the principal strains.

$$\varepsilon_1 = \frac{1}{E}\left[\sigma_1 - \nu(\sigma_2 + \sigma_3)\right] \quad (13)$$

$$\varepsilon_2 = \frac{1}{E}\left[\sigma_2 - \nu(\sigma_3 + \sigma_1)\right] \quad (14)$$

$$\varepsilon_3 = \frac{1}{E}\left[\sigma_3 - \nu(\sigma_2 + \sigma_1)\right] \quad (15)$$

In chapter 7.4.4 the equivalent elastic strain distribution as a result of the FE simulations is depicted. The equivalent elastic strain can be derived similar to the equivalent (or von Mises) stress. The equivalent elastic strain is determined as it is described in Equation 16.

$$\varepsilon_{equiv} = \frac{1}{2}\sqrt{(\varepsilon_1 - \varepsilon_2)^2 + (\varepsilon_2 - \varepsilon_3)^2 + (\varepsilon_1 - \varepsilon_3)^2} \quad (16)$$

The equivalent elastic strain can be expressed also in terms of non-principal strains in general state:

$$\varepsilon_{equiv} = \frac{1}{\sqrt{2}}\left[(\varepsilon_x - \varepsilon_y)^2 + (\varepsilon_y - \varepsilon_z)^2 + (\varepsilon_z - \varepsilon_x)^2 + 6(\tau_{xy}^2 + \tau_{yz}^2 + \tau_{zx}^2)\right]^{\frac{1}{2}} \quad (17)$$

11.2 Appendix 2

The schematic sketch of the rolling process is shown in Figure 96. During forward rolling the ball “sticks” to the surface of the rubber at its pole point “P”. One can define a rotation around the pole point (ω) (cf. Figure 96-a). Because the rubbers are easily deformable and the same time high friction arises between the two counterparts, the pole point “P” will be extended to a “sticking zone” (cf. Figure 96-b). Further on, based on the works of Heathcote [117] we assume that in the contact area a complex sliding zone evolve with relative forward and backward displacements ($V_{slide\text{-}forward}$, $V_{slide\text{-}backward}$) (cf. Figure 96-b).

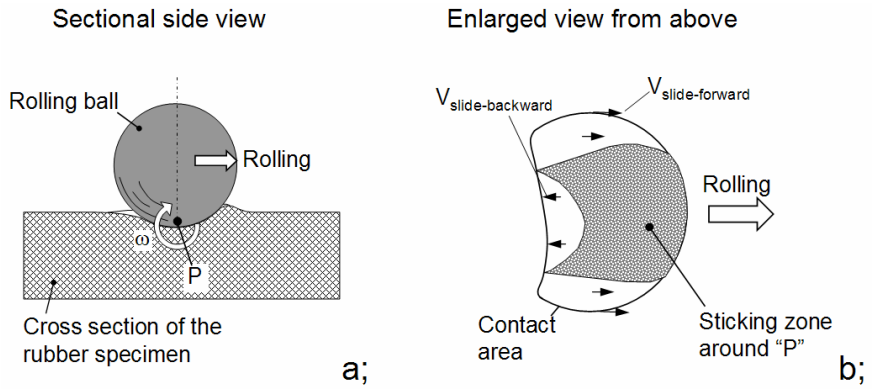

Figure 96: Schematic sketch of the rolling contact for steel ball and elastomeric plane in sectional side view (a;) and enlarged view from above of the contact area (b;)

References

1 Nau, B.S.: The state of the art of rubber-seal technology. Rubber Chemistry and Technology 60 (1987) pp.381-416

2 James, D.I. (Ed.): Abrasion of Rubber. London: Maclaren and Sons 1967

3 Sarkar, A.D.: Friction and Wear. New York: Academic Press 1980

4 Bartenev, G.M., Lavrentev, V.V.: Friction and Wear of Polymers, Elsevier: Amsterdam 1981

5 Gent, A.N., Pulford, C.T.R.: Mechanisms of rubber abrasion, Journal of Applied Polymer Science 28 (1983) pp.943-960

6 Schweitz, J.-Å., Åhman, L..: Mild wear of rubber-based compounds. In 'Friction and Wear of Polymeric Composites' Friedrich, K. (Ed.) Amsterdam: Elsevier 1986, pp. 289-327

7 Zhang, S.-W.: Tribology of Elastomers, Elsevier: Amsterdam 2004

8 Briscoe, B.J., Sinha, S.K.: Tribology of polymeric solids and their composites In. `Wear – Materials, Mechanisms and Practice` Stachowiak, G.W. (Ed.) New York, USA: Wiley 2005 pp.223-267

9 Myshkin, N.K., Petrokovets, M.I., Kovalev, A.V.: Tribology of polymers: adhesion, friction, wear and mass-transfer. Tribology International 38 (2005) pp.910-921

10 Barquins, M.: Adherence, friction and wear of rubber-like materials. Wear 158 (1992) pp.87-117

11 Horváth, L.: A gumiipar története. In ´Gumiipari Kézikönyv I´, Bartha, Z. (Ed.) Budapest, Hungary: TAURUS-OMIKK 1988, pp.19-23

12 http://en.wikipedia.org/wiki/Vulcanization, Accessed on 22.09.2008

13 Naghdi, K.: Rubber as an Engineering Material: Guideline for Users. Munich: Hanser Publishers 1993

14 Soós, I.: Szintetikus kaucsukok. In ´Gumiipari Kézikönyv I´, Bartha, Z. (Ed.) Budapest, Hungary: TAURUS-OMIKK 1988, pp.94-160

15 Donnet, J.-B., Bansal, R.C., Wang, M.-J.: Introduction. In ´Carbon Black Science and Technology´ Donnet, J.B., Bansal, R.C., Wang, M.J. (Eds.) New York, USA: Dekker 1993, pp. xvii

16 Kühner, G., Voll, M.: Manufacture of carbon black. In ´Carbon Black Science and Technology´ Donnet, J.B., Bansal, R.C., Wang, M.J. (Eds.) New York, USA: Dekker 1993, pp. 1-64 (1993)

17 Bansal, R.C., Donnet, J.-B.: Mechanism of carbon black. In ´Carbon Black Science and Technology´ Donnet, J.B., Bansal, R.C., Wang, M.J. (Eds.) New York, USA: Dekker 1993, pp. 67-83 (1993)

18 Hess, W.M., Herd, C.R.: Microstructure, morphology and general physical properties. In ´Carbon Black Science and Technology´ Donnet, J.B., Bansal, R.C., Wang, M.J. (Eds.) New York, USA: Dekker 1993, pp. 139-142

19 Heidenreich, R.D., Hess, W.M., Ban, L.L.: A test object and criteria for high resolution electron microscopy. Journal of Applied Crystallography 1 (1968) pp.1-19

20 Weigert, A.: Rastertunnelspektroskopie an Füllstoffrußen. Dissertation, Universität Regensburg, (2005) pp.3-16

21 Schröder, A.: Charakterisierung verschiedener Russtypen durch systematische statische Gasadsorption. Dissertation, Universität Hannover, (2000) pp.1-16

22 Donnet, J.-B., Custodéro, E.: Carbon black surface studied by scanning tunneling microscopy. In ´Carbon Black Science and Technology´ Donnet, J.B., Bansal, R.C., Wang, M.J. (Eds.) New York, USA: Dekker 1993, pp. 221-225

23 Treloar, L. R. G.: The Physics of Rubber Elasticity, Oxford: Clarendon Press 1975

24 http://www.engin.brown.edu/courses/En222/Notes/Kinematics/Kinematics.htm, Accessed on 22.09.2008

25 http://en.wikipedia.org/wiki/Deformation_gradient, Accessed on 22.09.2008

26 Bodor, G., Vas, L.M.: Polimer Anyagszerkezettan. Budapest: Müegyetem Kiadó 1998, pp.170

27 DMA Online Help for Q Series™ analysers, ©2001-2004 TA Instruments—Waters LLC, http:\\www.tainstruments.com

28 Ferry, J. D.: Viscoelastic Properties of Polymers. New York: John Wiley & Sons 1980, pp.274-287

29 Aklonis, J.J., MacKnight, W.J.: Introduction to Polymer Viscoelasticity. New York: Wiley-Interscience Publication 1983, pp.47-56

30 Ward, I.M.: Mechanical Properties of Solid Polymers. Chichester: John Wiley & Sons 1971, pp.146-164

31 Matsuoka, S.: Relaxation Phenomena in Polymers. Munich: Hanser Publishers 1992, pp. 47-48

32 Herdy, M.: Introductory Theory Manual, ViscoData & ViscoShift. http://www.viscodata.de/Short_Introduction.pdf, Accessed on 22.09.2008

33 Tschoegl, N.W.: The Phenomenological Theory of Linear Viscoelastic Behavior. Berlin: Springer-Verlag 1989, pp.119-121

34 Shaw, M.T., MacKnight, W.J.: Introduction to Polymer Viscoelasticity. New Jersey: John Wiley & Sons 2005, pp.51-65

35 http://www.viscodata.de/ Accessed on 22.09.2008

36 http://en.wikipedia.org/wiki/X-ray_photoelectron_spectroscopy, Accessed on 22.09.2008

37 http://en.wikipedia.org/wiki/Electron_binding_energy, Accessed on 22.09.2008

38 Reimer, L.: Scanning Electron Microscopy. Berlin: Springer-Verlag 1985

39 http://en.wikipedia.org/wiki/Raman_spectroscopy, Accessed on 22.09.2008

40 Koenig, J.L.: Spectroscopy of Polymers. ACS Professional Reference Book. Washington DC: American Chemical Society 1992

41 http://en.wikipedia.org/wiki/Surface_energy#Young.27s_equation, Accessed on 22.09.2008

42 http://en.wikipedia.org/wiki/Contact_angle, Accessed on 22.09.2008

43 Zaghzi, N., Carre, A., Shanahan, M.E.R., Papirer, E., Schultz, J.: A study of spontaneous rubber / metal adhesion. I. The rolling cylinder test. Journal of Polymer Science, Part B Polymer Physics 25 (1987), pp. 2393-2402

44 Chernyak, Y.B., Leonov, A.I.: On the theory of the adhesive friction of elastomers. Wear 108 (1986) pp.105-138

45 Vorvolakos, K., Chaudhury, M.K.: The effects of molecular weight and temperature on the kinetic friction of silicone rubbers. Langmuir 19 (2003) pp.6778-6787

46 Sills, S., Vorvolakos, K., Chaudhury, M.K., Overney, R.M.: Molecular origins of elastomeric friction. In ´Fundamentals of Friction and Wear on the Nanoscale´ Gnecco, E., Meyer, E. (Eds.) Heidelberg: Springer Verlag 2007, pp.659-676

47 Persson, B.N.J.: Qualitative theory of rubber friction and wear. Journal of Chemical Phsics 112 (2000) pp.2021-2029

48 Palasantzas, G.: Influence of self-affine surface roughness on the friction coefficient of rubbers. Journal of Applied Physics 94 (2003) pp.5652-5655

49 Persson, B.N.J., Albohr, O., Tartaglino, U., Volokitin, A.I., Tosatti, E.: On the nature of surface roughness with application to contact mechanics, sealing, rubber friction and adhesion. Journal of Physics Condensed Matter 17 (2005) R1-R62

50 Le Gal, A., Yang, X., Klüppel, M.: Evaluation of sliding friction and contact mechanics of elastomers based on dynamic mechanical analysis. The Journal of Chemical Physics 123 (2005) pp.014704-1 - 014704-11

51 Le Gal, A., Klüppel, M.: Investigation and modelling of adhesion friction on rough surfaces. Kautschug, Gumi, Kunststoffe 59 (2006) pp.308-315

52 Tabor, D.: The mechanism of rolling friction II. The elastic range. Proceedings of the Royal Society of London. Series A, Mathematical and Physical Sciences 229 (1955) pp.198-220

53 Eldredge, K.R., Tabor, D.: The mechanism of rolling friction I. The plastic range. Proceedings of the Royal Society of London. Series A, Mathematical and Physical Sciences 229 (1954) pp.181-198

54 Morland, L.W.: A plane problem of rolling contact in linear viscoelasticity theory. Journal of Applied Mechanics (1962) pp.345-352

55 Pöschel, T., Schwager, T., Brilliantov, N.V.: Rolling friction of a hard cylinder on a viscous plane. The European Physical Journal B 10 (1999) pp.169-174

56 Flom, D.G.: Rolling friction of polymeric materials I. Elastomers. Journal of Applied Physics 31 (1960) pp:306-314

57 May, W.D., Morris, E.L., Atack, D.: Rolling friction of a hard cylinder over a viscoelastic material. Journal of Applied Physics 30 (1959) pp.1713-1724

58 Flom, D.G., Bueche, A.M.: Theory of rolling friction for spheres. Journal of Applied Physics 30 (1959) pp.1725-1730

59 Severin D., Lütkebohle, H.: Rollreibung zylindrischer Laufräder aus Kunststoff. Konstruktion 37 (1985) pp.177-184

60 Heinrich, G.: Zur L. Föppls Theorie der rollenden Reibung. Österreichischer Ing.-Archiv No. 4 (1950)

61 Moore, D.F.: On the decrease in contact area for sphere and cylinders rolling on a viscoelastic plane. Wear 21 (1972) pp.179-194

62 Severin, D., Kühlken, B.: Tragfähigkeit von Kunststoffrädern unter Berücksichtigung der Eigenerwärmung Teil 1. Konstruktion 43 (1991) pp.65-71

63 Severin, D., Kühlken, B.: Tragfähigkeit von Kunststoffrädern unter Berücksichtigung der Eigenerwärmung Teil 2. Konstruktion 43 (1991) pp.153-160

64 Kulkarny, S. M., Rubin, C. A., Hahn, G. T.: Elasto-plastic coupled temperature-displacement finite element analysis of two-dimensional rolling-sliding contact with a translating heat source. Journal of Tribology 113 (1991) pp.93-113

65 Severin, D., Qiao, L.: The Thermomechanical calculation of polymer roller with finite element method. In ´Advances in computational Methods for Simulation´ Topping, B.V.H. (Ed:) Edinburgh: Civil-Comp Press 1996, pp.73-77

66 Bederna, Ch., Engst, W.: Analyse des Eindrück-Rollwiderstandes bei Gurterförderern mit der Methode der Finitien Elementen. Kautschug, Gummi, Kunststoffe 51 (1998) pp.690-699

67 Severin, D., Qiao, L.: The thermomechanical calculation of polymer roller with finite element method. In ´Advances in Computational Methods for Simulation´ Topping, H.V. (Ed.) Edinburgh: Civil-Comp Ltd. 1996, pp.73-77

68 Persson, B.N.J., Albohr, O., Heinrich, G., Ueba, H.: Crack propagation in rubber-like materials. Journal of Physics: Condensed Matter 17 (2005) R-1071-R1141,

69 Zhang, S. W.: Tribology of Elastomers, Amsterdam: Elsevier 2004

70 Scholz, K.G.: Tribologie der Elastomee. Ratingen: Dr Gupte Verlag 2006

71 Czichos, H., Habig, K.-H.: Tribologie Handbuch - Reibung und Verschleiß. Braunschweig: Vieweg 1992

72 Friedrich, K.: Friction and Wear of Polymer Composites. Amsterdam: Elsevier 1986

73 http://www.taberindustries.com/products/abraser/taber_abraser_description.as Accessed at 22.08.2008

74 Gent, A.N., Pulford, C.T.R.: Mechanisms of rubber abrasion. Journal of Applied Polymer Science 28 (1983) pp.943-960

75 Patrikeev, G.A., Antchak, V.K., Levinshtein, M.S., Khrenov, I.F.: A new method and apparatus for studying the abrasion resistance of rubberized fabrics. In ´Abrasion of Rubber´ James, D.I. (Ed.) London: Maclaren and Sons Ltd. 1967, pp.290-293

76 Nah, C., Jo, B.W., Kaang, S.: Cut and chip resistance of NR-BR blend compounds. Journal of Applied Polymer Science 68 (1998) pp.1537-1541

77 Rudakov, A.P., Kuvshinskii, E.V.: Abrasion of rubber by a smooth indentor. In ´Abrasion of Rubber´ James, D.I. (Ed.) London: Maclaren and Sons Ltd. 1967, pp.36-44

78 Browning, R.L., Jiang, H., Sue, H.J.: Scratch behavior of polymeric materials. In ´Tribology of Nanocomposites´ Friedrich, K., Schlarb, A.K. (Eds.) Amsterdam: Elsevier 2008, pp.354- 373

79 Felder, E., Bucaille, J.-L.: Mechanical analysis of the scratching of metals and polymers with conical indenters at moderate and large strains. Tribology International 39 (2006) pp.70-87

80 Nekrasov, S.S., Ofengenden, N.E.: Study of the abrasion resistance of plastics, cast basalt and rubbers in hydraulic mixtures. In ´Abrasion of Rubber´ James, D.I. (Ed.) London: Maclaren and Sons Ltd. 1967, pp.317-321

81 Marei, A.I., Izvozchikov, P.V.: Determination of the wear of rubbers in a stream of abrasive particles. In ´Abrasion of Rubber´ James, D.I. (Ed.) London: Maclaren and Sons Ltd. 1967, pp.274-280

82 Ruckdäschel, H., Sandler, J.K.W., Altstädt, V.: On the friction and wear of carbon nanofiber-reinforced PEEK-based polymer composites, In ´Tribology of

Nanocomposites´ Friedrich, K., Schlarb, A.K. (Eds.) Amsterdam: Elsevier 2008, pp.149-208

83 Jacobs, O., Schädel, B.: Wear Behavior of carbon nanotube-reinforced polyethylene and epoxy composites. , In ´Tribology of Nanocomposites´ Friedrich, K., Schlarb, A.K. (Eds.) Elsevier: Amsterdam 2008, pp.209-244

84 Qianming, G., Dan, L., Zhi, L., Su, Y.X., Ji, L.: Tribology properties of carbon nanotube-reinforced composites. In ´Tribology of Nanocomposites´ Friedrich, K., Schlarb, A.K. (Eds.) Elsevier: Amsterdam 2008, pp.245-267

85 Yang, A.C.-M., Ayala, J.E., Scott, J.C.: Abrasive wear in filled elastomers. Journal of Materials Science 26 (1991) pp.5823-5837

86 Fukahori, Y., Yamazaki, H.: Mechanism of rubber abrasion part 3: how is friction linked to fracture in rubber abrasion? Wear 188 (1995) pp.19-26

87 Atkins, A.G., Liu, J.H.: Toughness and the transition between cutting and rubbing in abrasive contacts. Wear 262 (2007) pp.146-159

88 Kato, K.: Wear and wear maps of coatings. In ´Tribology of Nanocomposites´ Friedrich, K., Schlarb, A.K. (Eds.) Elsevier: Amsterdam 2008, pp.271-282

89 Glaeser, W.A.: Wear debris classification. In ´Modern Tribology Handbook, Volume One´ Bhushan, B. (Ed.) Boca Raton: CRC Press 2001, pp.301-315

90 Schalamach, A.: How does rubber slide? Wear 17 (1971) pp.301-312

91 Reznikovskii, M. M., Brodskii, G.I.: Features of the mechanism of abrasion of highly elastic materials. In ´Abrasion of Rubber´ James, D.I. (Ed.) London: Maclaren and Sons Ltd. 1967, pp.14-22

92 Karger-Kocsis, J., Felhös, D., Thomann, R.: Tribological behavior of a carbon-nanofiber-modified santoprene thermoplastic elastomer under dry sliding and

fretting conditions against steel. Journal of Applied Polymer Science 108 (2008) pp.724–730

93 Felhös, D., Karger-Kocsis, J.: Tribological testing of peroxide-cured EPDM rubbers with different carbon black contents under dry sliding conditions against steel. Tribology International 41 (2008) pp.404-415

94 Felhös, D., Karger-Kocsis, J., Xu, D.: Tribological testing of peroxide cured HNBR with different MWCNT and silica contents under dry sliding and rolling conditions against steel. Journal of Applied Polymer Science 108 (2008) pp. 2840-2851

95 http://en.wikipedia.org/wiki/Zinc_oxide, Accessed at 22.08.2008

96 http://www.chemicalland21.com/fc/RUBBER%20ACCELERATORS.htm RUBBER ACCELERATORS, Accessed at 22.08.2008

97 http://www.chemicalland21.com/arokorhi/specialtychem/perchem/ ZINC%20 DIBENZYLDITHIOCARBAMATE.htm, Accessed at 22.08.2008

98 Navrátil, Z., Bursikova, V., Stahel, P., Sira, M., Zverina, P.: Czechoslovak Journal of Physics, 54 (2004), Suppl. C, C887-C882

99 Bhomwick, A.K., De, P.P., Bhattacharyya, A.K.: Adhesive tack and green strength of EPDM rubber. Polymer Engineering and Science 27 (1987) pp.1195-1202

100 Gent, A.N., Vondracek, P.: Spontaneous adhesion of silicone rubber. Journal of Applied Polymer Science 27 (1982) pp.4357-4364

101 Lee, L.-H.: Adhesion of high polymers. I. Influence of diffusion, absorption, and physical state on polymer adhesion. Journal of Polymer Science 5 (1967) pp.751-760

102 Chou, H.-W., Huang, J.-S., Lin, S.-T.: Effects of thermal aging on fatigue of carbon black–reinforced EPDM rubber. Journal of Applied Polymer Science 103 (2007) pp.1244–1251

103 Lonkar, S.P., Kumar, A.P., Singh, R.P.: Photo-stabilization of EPDM-clay nanocomposites: effect of antioxidant on the preparation and durability. Polym. Adv. Technol. 18 (2007) pp.891–900.

104 Zajickova, L., Bursiková, V., Perina, V., Macková, A., Subedi, D., Janca, J. Smirnov, S.: Plasma modification of polycarbonates. Surface and Coatings Technology 142–144 (2001) pp.449-454

105 Bursiková, V., Navrátil, V., Zajíckova, L., Janca, J.: Temperature dependence of mechanical properties of DLC/Si protective coatings prepared by PECVD. Materials Science and Engineering 324 (2002) pp.251-254

106 Felhös, D., Karger-Kocsis, J.: Tribological testing of peroxide-cured EPDM rubbers with different carbon black contents under dry sliding conditions against steel. Tribology International 41 (2008) pp.404-415.

107 Alisoy, H.Z., Baysar, A., Alisoy, G.T.,: Physicomathematical analysis of surface modification of polymers by glow discharge in SF6+N2 medium. Physica A: Statistical Mechanics and its Applications 351 (2005) pp.347-357

108 Mitra, S.; Ghanbari-Siahkali, A.; Kingshott, P.; Almdal, K.; Rehmeier, H.K., Abildgaard, H.: Chemical degradation of crosslinked ethylene-propylene-diene rubber in an acidic environment. Part I. Effect on accelerated sulphur crosslinks. Polymer Degradation and Stability 91 (2006) pp.69-80.

109 Swaraj, S., Oran, U., Lippitz, A., Friedrich, J.F., Unger, W.E.S.: Surface analysis of plasma-deposited polymer films, 6. Analysis of plasma deposited allyl alcohol films before and after aging in air. Plasma Processes and Polymers 2 (2005) pp.572–580

110 Laoharojanaphand, P., Lin, T.J., Stoffer J.O.: Glow discharge polymerization of reactive functional silanes on poly(methyl methacrylate). Journal of Applied Polymer Science 40 (1990) pp.369-384

111 Zhao, Q., Li, X., Gao, J.: Surface degradation of ethylene–propylene–diene monomer (EPDM) containing 5-ethylidene-2-norbornene (ENB) as diene in artificial weathering environment. Polymer Degradation and Stability 93 (2008) pp.692-699

112 Beamson, G., Briggs, D.: High resolution XPS of organic polymers - the scienta ESCA 300 data base. Chichester: John Wiley & Sons 1992

113 Morland, L.W.: Exact solutions for rolling contact between viscoelastic cylinders. Quarterly Journal of Mechanics and Applied Physics 20 (1966) pp.75-106

114 Knothe, K., Wang G.: Zur Theorie der Rollreibung zylindrischer Kunststoffräder. Konstruktion 41 (1989) pp.193-200

115 MSC.MARC Volume A: Theory of User Information, Version 2001, April

116 Johnson, K.L.: Contact Mechanics. London: Cambridge University Press 1985

117 Halling, J.: In ´Principles of Tribology´ J. Halling (Ed.) London: Macmillan Press 1975, pp.:182-198

List of Publications

1 Karger-Kocsis J., **Felhős, D**.: Friction and sliding wear of “nanomodified” rubbers and their coatings: Some new developments. In ‘Tribology of Polymeric Nanocomposites’ Friedrich K., Schlarb, A.K. (eds.) Amsterdam: Elsevier 2008, pp.304-324

2 Váradi, K., **Felhős, D.**, Friedrich, K., Tsotra, P.: Experimental and FE analysis of the failure behaviour of SIC/epoxy functionally graded rings under compression load. 1st Vienna Int. Conf. Micro- and Nano-Technology, 2005 March 9-11, Vienna, Austria, pp.431-440 ISBN 3-901657-17-17

3 **Felhős, D.**, Váradi, K., Friedrich, K.: FE modeling of a roller with functionally graded material structure. Műanyagipari Szemle 4 (2005) pp.81-89 (in Hungarian)

4 **Felhős, D.**, Váradi, K., Friedrich, K., Tsotra, P.: Microindentation test of graded SiC/EP rings: Experimental results and FE modelling. Journal of Computational and Applied Mechanics 6 (2005) pp.177-188

5 **Felhős, D.**, Váradi, K., Tsotra, P Friedrich, K.: Compression of Homogeneous and Graded SiC/EP Rings Experimental Results and FE Modelling. Journal of Materials Science 41 (2006) pp.3349-3355

6 **Felhős, D.**, Váradi, K., Friedrich, K.: Wear Analysis of Functionally Gradient Composite Materials by FE Modeling of Microhardness Measurements and Wear Tests. In ´Materials Science, Testing and Informatics III, Materials Science Forum´ Gyulai, J., and Szabó, P.J. (eds.) Vol. 537-538 (2006) pp.519

7 Vas. M., Pölöskei K., **Felhös D.,** Deák T., Czigáy T.: Theoretical and experimental study of the effect of fiber heads on the mechanical properties of non-continuous basalt fiber reinforced composites. eXPRESS Polymer Letters 1 (2007) pp.109-121

8 Molnár, P., **Felhős, D.,** Mitschang, P.: Improvement in bonding of functional elements with the fiber reinforced polymer structure by mean of tailoring technology. Journal of Composite Materials 41 (2007) pp.2569-2583

9 Karger-Kocsis, J., **Felhös, D.**, Thomann, R.: Tribological Behavior of a Carbon-Nanofiber-Modified Santoprene Thermoplastic Elastomer Under Dry Sliding and Fretting Conditions Against Steel. Journal of Applied Polymer Science 108 (2008) pp.724–730

10 **Felhös, D.**, Karger-Kocsis, J.: Tribological testing of peroxide-cured EPDM rubbers with different carbon black contents under dry sliding conditions against steel. Tribology International 41 (2008) pp.404-415

11 **Felhös, D.**, Karger-Kocsis, J., Xu, D.: Tribological testing of peroxide cured HNBR with different MWCNT and silica contents under dry sliding and rolling conditions against steel. Journal of Applied Polymer Science 108 (2008) pp.2840**-**2851

12 Karger-Kocsis, J., **Felhös**, **D.**, Xu, D., Schlarb, A.K.: Unlubricated sliding and rolling wear of thermoplastic dynamic vulcanizates (Santoprene®) against steel. Wear 265 (2008) pp.292-300

13 **Felhos**, **D.,** Xu, D., Schlarb, A.K., Varadi, K., Goda, T.: Viscoelastic characterization of an EPDM rubber and finite element simulation of its dry rolling friction. eXPRESS Polymer Letters 2 (2008) pp.157-164

14 Karger-Kocsis, J., **Felhos**, **D.**, Barany, T., Czigany, T.: Hybrids of HNBR and in situ polymerizable cyclic butylene terephthalate (CBT) oligomers: properties and dry sliding behavior. eXPRESS Polymer Letters 2 (2008) pp.520-527

15 **Felhos, D.**, Prehn, R., Varadi, K., Schlarb, A.K.: FE simulation of the indentation deformation of SiC modified vinylester composites in respect to their abrasive wear performance**.** eXPRESS Polymer Letters 2 (2008) pp.705-717

List of Students Support Works

1 Bajo, G.M.: Sliding Wear of Rubbers and its Correlation with Mechanical/Structural Parameters. Diploma Work, Technische Universität Kaiserslautern (2007)

CURRICULUM VITAE

Personal

Family name:	Felhös
First name:	Dávid
Date and place of birth:	31. July 1979; Vásárosnamény
Citizenship:	Hungarian
Correspondence address:	Kriza János út 28, 4803 Vásárosnamény Hungary

Education

1985-1993	Eötvös József Primary School in Vásárosnamény, Hungary
1993-1998	Korányi Frigyes Bilingual High School (German-Hungarian) in Nagykálló, Hungary
1998-1999	Engineer-Physicist Studies in Faculty of Natural Sciences at the Budapest University of Technology and Economics, Hungary
1999-2004	Mechanical Engineering Studies in Machine Design and Polymer Science at the Budapest University of Technology and Economics, Hungary
2004-2006	PhD Studies at the Budapest University of Technology and Economics, Department of Machine and Product Design, Hungary
2006 – Today	PhD research assistant at the Institut für Verbundwerkstoffe GmbH (IVW) at the Technische Universität Kaiserslautern, Germany

Scholarships Erasmus Scholarship at the Institut für Verbundwerkstoffe GmbH (IVW) at the Technische Universität Kaiserslautern, Germany

Languages Hungarian (native language), German, English